

NASA Contractor Report 3887

**Method for the Prediction
of the Installation
Aerodynamics of a Propfan
at Subsonic Speeds**

B. Chandrasekaran

**CONTRACT NAS1-16742
APRIL 1985**

NASA

NASA Contractor Report 3887

**Method for the Prediction
of the Installation
Aerodynamics of a Propfan
at Subsonic Speeds**

B. Chandrasekaran
Vigyan Research Associates, Inc.
Hampton, Virginia

Prepared for
Langley Research Center
under Contract NAS1-16742

NASA

National Aeronautics
and Space Administration

**Scientific and Technical
Information Branch**

1985

1.0 TABLE OF CONTENTS

1.0	TABLE OF CONTENTS	1
2.0	INDEX OF FIGURES	2
3.0	NOMENCLATURE	5
4.0	SUMMARY	8
5.0	INTRODUCTION	9
6.0	OUTLINE OF THE THEORY	12
7.0	DETERMINATION OF THE EFFECT OF THE PROPELLER	13
7.1	<u>Calculation of the Axial Induced Velocity in the Slipstream</u>	16
7.1.1	<u>Vortex Ring Modelling</u>	16
7.1.2	<u>Blade Performance Theory</u>	20
7.2	<u>Calculation of the Swirl Velocity</u>	24
7.3	<u>Treatment of the Pressure Increase in the Slipstream</u>	26
8.0	IMPLEMENTING THE PROPELLER EFFECTS INTO THE PANEL CODE AND THE CALCULATION PROCEDURE	27
9.0	EXPERIMENTAL SETUP	30
10.0	RESULTS AND DISCUSSION	31
10.1	<u>Wing Alone Comparison</u>	31
10.2	<u>Wing/Nacelle Comparisons</u>	33
10.3	<u>Wing/Nacelle/With Powered Propfan</u>	34
10.3.1	<u>Overwing Nacelle</u>	34
10.3.2	<u>Underwing Nacelle</u>	38
11.0	CONCLUSIONS AND RECOMMENDATIONS	39
12.0	REFERENCES	41

2.0 INDEX OF FIGURES

1. Bound and Trailing Vortex System for a Propeller.
2. Wake System for Slipstream Model.
3. Vortex Ring Modelling for the Propeller Wake.
4. Definition of the Parameters Associated with the Vortex Tube Modelling.
5. Velocity Diagram for a Blade Element Showing Induced Velocity Components.
6. Definition of Slipstream Parameters.
7. Axial Induced Velocity Distribution Along the Blade Radius of the Propfan for a High Thrusting Load with $C_T = 0.343$, $M_\infty = 0.5$, $\alpha = 2.990$, $J = 2.367$, $\beta = 52.5$ degrees.
8. Induced Angular Velocity Distribution Along the Blade Radius of the Propfan for a High Thrusting Load with $C_T = 0.343$, $M_\infty = 0.5$, $\alpha = 2.990$, $J = 2.367$, $\beta = 52.5$ degrees.
9. Wing/Nacelle/Propfan Configuration and the Panelling Used.
10. Model Planform.
11. C_p Comparison for the Wing Alone Configuration at $M_\infty = 0.50$, $\alpha = 1.0$ degrees.
12. C_p Comparison for Wing Alone with Strip Boundary Layer Correction at $M_\infty = 0.50$, $\alpha = 1.0$ degree.
13. C_N Comparison for the Wing Alone with Strip Boundary Layer Correction $M_\infty = 0.5$, $\alpha = 1.0$ degree.
14. C_p Comparisons for Wing/Overwing Nacelle with Strip Boundary Layer Correction, $M_\infty = 0.5$, $\alpha = 1.0$ degree.
15. C_N Comparison for the Wing/Overwing Nacelle at $M_\infty = 0.5$, $\alpha = 1.0$ degree.
16. C_p Comparison for the Wing/Underwing Nacelle at $M_\infty = 0.702$, $\alpha = -0.025$ degrees. (Boundary Layer Not Included in Theory.)
17. C_N Comparison for the Wing/Underwing Nacelle at $M_\infty = 0.702$, $\alpha = -0.025$ degrees. (Boundary Layer Not Included in Theory.)

18. C_p Comparison for Wing/Overwing Nacelle/High Power by the Method I, with $C_T = 0.443$, $M_\infty = 0.5$, $\alpha = 1.0$ degree.
19. C_p Comparison for Wing/Overwing Nacelle/High Power by the Method I, $C_T = 0.408$, $M_\infty = 0.5$, $\alpha = 2.992$ degrees.
20. C_p Distribution Comparison for High Thrusting Load with $C_T = 0.443$ by Method II, $M_\infty = 0.5$, $\alpha = 1.0$ degree.
21. C_p Distribution Comparison for High Thrusting Load With $C_T = 0.408$ by Method II, $M_\infty = 0.5$, $\alpha = 2.992$ degrees.
22. C_N Comparison of Method II with Method I for High Thrusting Load with $C_T = 0.443$, $M_\infty = 0.5$, $\alpha = 1.0$ degree.
23. C_N Comparison of Method II with Method I for High Thrusting Load with $C_T = 0.408$, $M_\infty = 0.5$, $\alpha = 2.992$ degrees.
24. C_p Distribution Comparison for a Medium Power Load with $C_T = 0.338$, $M_\infty = 0.5$, $\alpha = 1.0$ degree.
25. C_p Comparison for a Low Power Load with $C_T = 0.137$, $M_\infty = 0.5$, $\alpha = 1.0$ degree.
26. C_N Comparison for a Low Power Load with $C_T = 0.137$, $M_\infty = 0.5$, $\alpha = 1.0$ degree.
27. C_N Comparison for a Medium Power Load with $C_T = 0.338$, $M_\infty = 0.5$, $\alpha = 1.0$ degree.
28. Interference Effect on C_N by the Addition of Overwing Nacelle/Powered Propeller to the Basic Wing Configuration. $M_\infty = 0.5$, $\alpha = 1.0$ degree.
29. C_p Comparison for the Wing/Underwing Nacelle/Powered Propeller with $C_T = 0.466$, $M_\infty = 0.701$, $\alpha = 0.0$ degrees, Method II, Without Boundary Layer.
30. C_p Comparison for the Wing/Underwing Nacelle/Powered Propeller With $C_T = .245$, $M_\infty = 0.700$, $\alpha = 0.0$ degrees, Method II, Without Boundary Layer.
31. C_N Comparison for the Wing/Underwing Nacelle/Powered Propeller With

$C_T = .466$, $M_\infty = 0.701$, $\alpha = 0.0$ degrees, Method II, Without Boundary Layer.

32. C_N Comparison for the Wing/Underwing Nacelle/Powered Propeller With $C_T = 0.245$, $M_\infty = 0.700$, $\alpha = 0.0$ degrees, Method II, Without Boundary Layer.

3.0 NOMENCLATURE

a_0	Two dimensional lift curve slope of the propeller blade section
a	Ratio of the induced velocity to free stream velocity V_I/V_∞
A_0	Area of the propeller
$A_{\text{effective}}$	$1/(1 - R_c^2)$
A_∞	Area of the contracted slipstream at the farwake
A_i	Area of the contracted slipstream at any intermediate point in the slipstream
$b(r)$	Chord of the propeller blade
B	Number of blades
C_T	Thrust coefficient of the propeller = $T/\rho n^2 D^4$
C_T^1	$4/\pi^3 \cdot C_T$
c	Wing chord
c_d	Drag coefficient of the propeller blade section
c_l	Lift coefficient of the propeller blade section
C_N	Normal force coefficient = $\int_0^1 (C_{p_{\text{lower}}} - C_{p_{\text{upper}}}) d(x/c)$
C_p	Pressure coefficient
ds	Elemental length, defined in $\Gamma = \oint_C v \cdot ds$
D	Diameter of the propeller
dC_T/dx	Thrust coefficient gradient
F	Prandtl's tip loss factor defined in equation 14
K_T	Tip loss factor defined in equation 14 and same as F .
L	Lift of the blade section
n	Revolutions/second
\vec{n}	Normal vector
P_2	Static pressure immediately downstream of the propeller

P_o	Static pressure at the farwake of the propeller
Q	Dynamic pressure
$r(z)$	Local slipstream radius at any station z downstream of the propeller
R (or) R_o	Radius of the propeller
R_c	Root cutout expressed as r/R .
R_p	Radial distance of a point inside the slipstream from the propeller axis
T	Thrust of the propeller
V	Velocity used in defining the circulation around a closed path
V_I	Induced velocity at the center of the propeller
V	Freestream velocity
$V(P)$	Increment velocity at a point P , due to the propeller wake
V_T	Tangential velocity of the tip of the propeller blade at $r = R$
$V_{T \text{ slipstream}}$	Tangential velocity at any point in the slipstream of the propeller blade
W_a	Axial component of the induced velocity
W_t	Tangential component of the induced velocity
w	Resultant of the axial and tangential induced velocity shown in figure 5
x	Nondimensional radial station = r/R
x/c	Chordwise location of the pressure tap on the wing section
y/R	Spanwise location on the wing section
z/R	Nondimensional axial distance downstream of the propeller
α	Angle of attack of the propeller and the aircraft
β	Pitch angle of the propeller blade
Δ	Increment

σ_j	Singularities used in the Hess code
Φ	Total velocity potential
ϕ_∞	Freestream potential
ϕ_w	Propeller wake potential
ϕ_B	Disturbance potential due to aircraft body
ϕ_T	Helix angle at the tip of the blade = β_T
ρ	Density of the air
λ	$(V_\infty \cos\alpha + V_I)/V_T$ used in Equation (6)
Γ	Circulation defined by $\oint_C v \cdot ds$
μ	$V_\infty \sin\alpha/V_T$ used in Equation (6)
Γ_{ring}	Circulation strength of the vortex ring
Γ_w	Wake circulation for the calculation of the tangential velocity
ω	Angular velocity

SUBSCRIPTS

n	derivative in the normal direction
α	free stream condition
s	slipstream
prop	at the propeller plane

4.0 SUMMARY

A subsonic-flow panel code has been modified to handle the effects of a propeller wake. The effects of the propeller slipstream are to increase the induced axial velocity, tangential velocity and a total pressure rise in wake of the propeller. Principles based on the blade performance theory, momentum theory, and vortex theory were used to evaluate the slipstream characteristics. The slipstream effects are superimposed into Neumann boundary conditions in the panel code to study the installation aerodynamics of the powered propellers mounted on overwing or underwing nacelle integrated with a supercritical wing. Theoretical calculations are compared to experimental results at Mach numbers 0.5, 0.6 and 0.7, over a wide range of angles of attack. The discrepancies between the theory and the experimental results are analysed. Inclusion of a viscous flow modelling is carried out to enhance the accuracy of the theoretical prediction.

5.0 INTRODUCTION

High speed propellers (propfans) have gained importance in recent years due to their higher fuel efficiency in comparison to high by-pass ratio turbofan engines. Propfans have the potential for reducing the fuel consumption of current transport aircraft by 14 to 30 percent (ref. 1, 2). Recent technology advances have shown that high speed turboprops can have up to 15 percent higher installed propulsive efficiency at Mach 0.8 cruise compared to present day propulsion systems. The propfan concept as advocated by the NASA Lewis Research Center and Hamilton-Standard Company consists of an eight bladed propeller operating with a disc loading of 301 kw/m^2 (37.5 hp/ft.^2) at Mach 0.8 and an altitude of 9.144 km (30,000 ft.). The projected propeller efficiency demonstrated through wind tunnel tests is 80 percent (ref. 2, 3). The interference effects of the propfan slipstream on the aircraft has not been determined to date and determination of these interference effects is a main design consideration for installation aerodynamics. Previous turboprop propulsion system analysis has been limited to aircraft designed without the use of modern supercritical wings or advanced propfan technology.

Even though adding a propfan enhances the fuel savings there are several critical problems to be examined which include: the demonstration of the projected performance, the achievement of acceptable level of internal cabin noise, and the efficient integration of the propeller/nacelle combination with the airframe. Careful consideration of the propfan and nacelle effects on the wing must be taken into account during installation in order to gain the beneficial effects derived from the propfan. To address all these problem areas one needs to understand the

flow behaviour as an initial step. Because model construction is expensive and time consuming, it would be advantageous to have a theoretical prediction scheme that could adequately predict the flow field with reasonable accuracy so that the experimental program could be considerably reduced in cost and time. Integration of the propeller/nacelle combination with the airframe is the key factor in determining the lift and drag characteristics of the wing due to the interference effect of the slipstream on the aerodynamic characteristics of the wing and vice versa.

Efforts should be directed towards minimization of the nacelle installation drag, which requires the elimination of the shocks and/or separated flow in the channels between the nacelle and fuselage. This requires a detailed understanding of the flow field aerodynamic characteristics and a knowledge of the interference effects. The interference effects on the propeller due to the presence of different aircraft components such as wings and bodies are found to affect the blade angle of attack characteristics significantly (ref. 4, 5). The interference effects on the wing and body are due to the slipstream of the propeller and nacelle installation onto the wing which alters the aerodynamic lift and drag distribution considerably (ref. 6, 7). For the interference calculations both these effects should be taken into account, causing considerable difficulty in formulating the problem and also in implementing a solution on present day computers. Due to this restriction, approximations are introduced into the formulation of the theory. One such approximation is considering that the effect of the aircraft components on the propeller blades are small.

The purpose of the present investigation is to develop a method for

predicting the interference effects of the propfan on the wing body aerodynamics that can aid in providing a better understanding of the complex flow phenomena associated with prop/nacelle/wing integrations. A very simple model, on which the geometry could be easily defined, is used to assess the capabilities of the developed theory. Experimental results obtained with this model are presented in reference 8. The configurations selected for this assessment are an overwing-nacelle integrated with an unswept supercritical wing, and an underwing-nacelle integrated with the same unswept supercritical wing.

6.0 OUTLINE OF THE THEORY

The basis of the method presented in this report is a subsonic panel method with modifications for incorporating the propeller-induced-onset effects. The panel method selected is based on reference 9. The treatment of the propeller induced effects is based on the theories outlined in references 10, 11, 12 and 19. The panel method uses a distribution of singularities for solving the potential flow past three dimensional arbitrary bodies and solves the equation

$$\nabla^2 \phi = 0 \quad (1)$$

where ϕ is the total velocity potential. Equation (1) is solved with the tangency boundary condition on the body surface such that the normal velocity is zero. The second boundary condition is such that ϕ must approach the undisturbed freestream potential at an infinite distance from the body surface. The total velocity potential ϕ , is comprised of the free stream potential ϕ_∞ , the propeller-wake potential ϕ_w , and a disturbance potential ϕ_B due to the wing and body. Symbolically

$$\phi = \phi_\infty + \phi_w + \phi_B \quad (2)$$

The flow tangency condition at the body surface requires

$$\partial\phi/\partial n = 0 \quad (3)$$

Applying equation (3) to equation (2), one obtains

$$\phi_n = \phi_{\infty n} + \phi_{wn} + \phi_{Bn} = 0$$

where

$$\phi_{\infty n} = -\vec{n} \cdot \vec{V}_\infty \text{ with } \vec{V}_\infty \text{ being the freestream velocity}$$

and $\phi_{W_n} = -\vec{n} \cdot \vec{V}(P)$ with $\vec{V}(P)$ being the nonuniform onset velocity due to the propeller wake at a point P on the body surface. ϕ_{B_n} is the normal component of the perturbation velocity potential due to the aircraft wing and body. From equation (3),

$$-\phi_{B_n} = -\vec{n} \cdot [\vec{V}_\infty + \vec{V}(P)] \quad (4)$$

Equation (4) is solved by approximating the body surface with discrete quadrilateral panels. Equation (4) is applied at each panel center point on the body surface. The effect of the aircraft body geometry enters in the left hand side of equation (4) while the propeller induced effects are described in the right hand side of equation (4). The doublet and source singularities are distributed on the panel surface and equation (4) can be expressed in matrix equation form as:

$$\sum_{j=1}^N (\vec{n}_i \cdot \vec{V}_{i,j}) \sigma_j = -\vec{n}_i \cdot (\vec{V}_\infty + \vec{V}(P))_i \quad (i = 1, 2, \dots, N) \quad (5)$$

where N is the total number of panels and $\vec{V}_{i,j}$ is a matrix comprised of aerodynamic influence coefficients expressed in terms of the geometry. Equation (5) is solved by standard numerical matrix techniques to obtain the singularity strengths σ_j . Once the singularity strengths are determined, the velocity and the pressure distribution can be obtained (ref. 13).

7.0 DETERMINATION OF THE EFFECT OF THE PROPELLER

There are three distinct effects of the propeller slipstream which are (1) the total pressure change across the slipstream, (2) the increased axial velocity downstream of the propeller due to the thrust force and the

contraction of the slipstream and (3) the swirl and the tangential velocity due to the torque of the propeller.

The thrust exerted by the propeller results in a discontinuous increase in total pressure of the flow as it passes through the disk which is manifest as a continuous increase in the slipstream axial velocity and an abrupt rise in static pressure. Due to the reaction of the torque of the propeller the slipstream will have a rotational motion imparted to it and this increases the kinetic energy of the slipstream.

The increased total pressure in the slipstream alters the pressure distribution on the wing sections, immersed in the slipstream flow, and thus alters the normal load and drag distribution on the wing accordingly.

The increase in the axial velocity increases the slipstream Mach number. The increased velocity over the wing in the slipstream will also cause a higher scrubbing drag due to the greater dynamic pressure in the slipstream. The swirl will act to induce an increase in the leading edge upwash on the upgoing side of the slipstream and a decrease on the other side. These perturbations in the wing leading edge onset flow will produce local loading changes which could aggravate the already existing high suction peaks.

The interaction of the wing with the slipstream could result in overall beneficial effect if the wing can recover some of the swirl energy as a local thrust.

To analyse the slipstream-wing interference problem, one should address all these areas and combine all the areas suitably to come up with a solution. The propeller can be modelled by considering it as an actuator disk, having an infinite number of blades, through which the velocity increase is continuous and the pressure increase is discontinuous

(ref. 14). The treatment of the propeller as an actuator disc model simplifies the complex flow representation a great deal and dates back to the Rankine momentum theory. Momentum theory is strictly a one dimensional theory and the properties are assumed to be constant along a plane downstream of the propeller. The momentum theory provides average information on the flow of a propeller with an infinite number of blades. But in reality, the flow is a rotating one, and the flow properties change from point to point in the slipstream of the propeller. There is no provision built in the momentum theory to accommodate this variation. The momentum theory of propellers provides certain basic information that is suitable in determining the upper limits of performance, the assumptions used in the theory are too gross to be practical for actual propellers with a finite number of blades. With a practical propeller, the axial, radial and tangential velocity losses must be found instead of only the axial loss as is found for the actuator disc considered in the momentum theory. Also, with practical propellers having a finite number of blades the axial velocity is not uniform across the disc, further increasing the losses. For these reasons, a more extensive theory is required to find the induced losses and velocity field of the actual propeller than is possible using the simple momentum theory. One such theory is the blade performance theory (ref. 15) which takes into account the local flow to a great detail. Blade performance theories are based on the aerodynamic characteristics of the local blade sections and also on the resulting velocity vectors on the propeller blade sections (ref. 15). The blade section at each radial distance from the axis of rotation is treated as a two-dimensional airfoil section operating in a fluid whose relative velocity is determined only by the propeller's

rotational speed and its forward motion.

The propeller modelling described in this present work is based on the principles derived from both the momentum theory and the blade performance theory. The axial velocity increase is modelled either by the vortex ring method or by the blade performance theory. Swirl is calculated from the blade performance theory calculations. Pressure increase is obtained by combining the axial velocity increase, and the swirl velocity changes, with the one dimensional momentum theory.

7.1 Calculation of the Axial Induced Velocity in the Slipstream

The present work incorporates two different methods for calculating the axial induced velocity increase in the slipstream by 1) vortex ring modelling and 2) blade performance theory. Both of these methods are described in detail in the following paragraphs.

7.1.1 Vortex Ring Modelling

The propeller wake is modelled by a system of ring vortices. This model is based on the concept of a vortex system representing a finite wing consisting of bound and trailing vortices and expressing the lift in terms of the strength of these vortices. The vortex system for the propeller model used in the present calculation is based on the principle that if one examines a propeller as shown in figure 1, there will be a bound vortex along the blade. At the root the free vortex is carried downwind by the flow through the propeller. The tip vortex is carried off in the same manner. These vortex lines constitute the slipstream of the propeller and the motion of the fluid in the slipstream can be calculated as the induced velocity of this vortex wake. The sense of rotation

of the vortex lines is such that the fluid in the slipstream has an increased axial velocity and a rotational velocity in the same sense as the rotation of the propeller. The rotation of the propeller blades makes the vortex lines lie on a spiral path (see fig. 2(a)). Even this simple spiral is difficult to analyse. So further breakdown of these spiral vortex lines to an axial component and a circumferential component makes the problem much simpler. The axial component is discarded as being of secondary importance (ref. 16). The wake then appears as a skewed stack of vortex rings as shown in figure 2(b). The final step is to assume that the rings are spaced so closely that they are equivalent to a continuous elliptic cylinder of vorticity (fig. 2(c)).

The strength of the vorticity is determined from the knowledge of the operating conditions of the propeller and from the thrust coefficient. The details of the modelling are given below. The induced velocity at the center of the propeller is calculated from the following relations (ref. 17).

$$V_I = 0.5 C_T^1 V_T A_{\text{effective}} / (\mu^2 + \lambda^2)^{1/2} \quad (6)$$

$$C_T^1 = 4/\pi^3 \cdot C_T$$

$$\lambda = (V_\infty \cos\alpha + V_I) / V_T$$

$$\mu = V_\infty \sin\alpha / V_T$$

$$A_{\text{effective}} = 1 / (1 - R_C^2)$$

where V_I is the induced velocity, V_T is the tip velocity of the blade and C_T is the thrust coefficient. Equation (6) is a nonlinear equation. It is solved iteratively with the initial value of V_I being obtained from the following relations

$$V_{I_{\text{initial}}} = 1/2(-V_{\infty} \cos \alpha + \sqrt{(V_{\infty} \cos \alpha)^2 + (2T/\rho A_0)}) \quad (7)$$

where the term $2T/\rho A_0$ is calculated from the given thrust coefficient C_T and from the area of the propeller $A_0 \cdot V_{I_{\text{initial}}}$ is substituted in the definition of λ and equation (6) is iterated until V_I in the left hand side of equation (6) converges. Usually only a few iterations are required for convergence. V_I is the induced velocity at the center of the rotor for the specified thrust conditions. By the method of reference 10, this value of V_I is equated to the vortex ring strength by the following equation

$$V_I = \sum_{j=1}^k \Gamma_{\text{ring}} / 2\pi R_{p,j} (A_j B_j + C_j D_j F_j) \quad (8)$$

where k is the total number of the vortex rings stacked in the vortex wake tube, as shown in figure 3; R_p is the radial distance of point p from the vortex ring axis; Γ_{ring} is the strength of the vortex ring; d_1 and d_2 are the minimum and maximum distances respectively from point p , to the ring as shown in figure 4. The definitions of A , B , C , D , and F are

$$A = k(T) - E(T) \quad (9)$$

where $T = (d_2 - d_1)/(d_2 + d_1)$, $E(T)$ is the complete Elliptic Integral of the second kind, and $K(T)$ is the complete Elliptic Integral of the first kind

$$\begin{aligned} B &= (d_r - 1)/d_1 + (d_r + 1)/d_2 \\ C &= d_1 + d_2 \\ D &= TE(T)/(1 - T^2) \\ F &= 1 - (1 + d_r^2 + d_a^2 - d_1 d_2)/2d_r^2 - ((1 + d_r)d_1^2 - (1 - d_r)d_2^2)/2d_r d_1 d_2 \end{aligned} \quad (10)$$

The definitions for d_a and d_r are given in figure 4.

Equation (8) is first applied at the center of the rotor with the left hand side of the equation being the V_I calculated from equation (6). This fixes the value of the circulation strength of the vortex rings that have been stacked in the wake. The circulation strength obtained from equation (8) is for a propeller with a uniform loading, and no azimuthal variation of the loadings are assumed.

A vortex tube, extending from the $-R$ to $+R$ is taken for calculations. Wake contraction was added by varying the vortex-ring radius according to the continuity equation. The variation of the axial induced velocity with axial distance is given by

$$W_a(Z) = V_I(1 + z/R/ \sqrt{1 + (z/R)^2}) \quad (11)$$

where z is the axial distance downstream of the propeller from the axis of the propeller and R is the radius of the propeller (ref. 18, 19). Since at the center of the rotor, the tangential velocity W_t is zero, the only velocity seen by the propeller is V_I . Having determined W_a from equation (11), the radius r at any z location in the slipstream is determined by satisfying the continuity relations as given by

$$\begin{aligned} \rho \cdot \pi R^2 \cdot (V_\infty \cos\alpha + V_I) &= \rho \cdot \pi r^2(z) \cdot (V_\infty \cos\alpha + W_a(z)) \\ r(z) &= R \cdot \sqrt{(V_\infty \cos\alpha + V_I)/(V_\infty \cos\alpha + W_a(z))} \end{aligned} \quad (12)$$

This fixes the radius of the contracted slipstream. In equation (12) it is assumed that the induced velocity in the rotor plane remains constant along the blade radius and equals to the value obtained at the center of the rotor and it is also assumed that the induced velocity does not vary with the radius. Reference 12 determines the slipstream radius by making

use of semi-empirical relations between the thrust coefficient and the slipstream contraction ratio given for various propellers and rotors (ref. 20). Equation (12) is used to determine the local radius of the slipstream for the present work.

7.1.2 Blade Performance Theory

In equation (8), it is assumed that the axial component of the induced velocity at any blade section is equal to the induced velocity at the center of the rotor calculated from equation (6). It is also assumed that the axial induced velocity does not change with the radius of the propeller and remains constant all along the blade radius. But for practical applications this is not true. So, for the correct determination of the axially induced velocity component in the slipstream, the following analysis described in reference 19 has also been incorporated. The theory incorporates the blade element properties. Figure 5 shows the section of a propeller blade operating in a freestream velocity of V with an angular ω .

The induced angle of attack is given by

$$\begin{aligned}\alpha_i &= 1/2(-x + \sqrt{x^2 + 4y}) \\ x &= \tan\phi + \sigma/(8xF\cos\phi) \\ y &= \sigma a_0(\beta - \phi)/(8xF\cos\phi)\end{aligned}\tag{13}$$

where ϕ , and β are defined in the figure 5. σ is the solidity of the blade given by

$$\sigma = Bb(r)R/\pi R^2 = Bb(r)/\pi R$$

where B is the number of blades, $b(r)$ is the local chord of the blade

section, R being the radius of the propeller and x is the nondimensional radius given by r/R . F is the Prandtl's tip loss factor and it is given by

$$F = (2/\pi)\cos^{-1} \exp[-B(1 - x)/2\sin\phi_T] \quad (14)$$

ϕ_T is the helix angle of the propeller's helical trailing vortex system at the tip and is given by

$$\phi_T = \beta_T$$

w_t is initially approximated by $w_t = V_R\alpha_j\sin(\phi + \alpha_j)$ where V_R is the resultant freestream velocity given by

$$V_R = \sqrt{(V_\infty\cos\alpha)^2 + (\omega r)^2}$$

and α_j is given by equation (13).

Figure 5 shows the induced velocity at the propeller plane in more detail. The resultant velocity w is normal to V_e and is composed of a tangential component, w_t , and an axial component, w_a . From the geometry, w_t and w_a are related by

$$(V_\infty\cos\alpha + w_a)/(\omega r - w_t) = w_t/w_a = \tan(\alpha_j + \phi)$$

This equation can be solved for w_a as a function of w_t .

$$w_a = 1/2[-V_\infty\cos\alpha + \sqrt{(V_\infty\cos\alpha)^2 + 4w_t(\omega r - w_t)}]$$

It is convenient to express all velocities in terms of V_T , where V_T is ωR and the preceding equation becomes

$$w_a/V_T = 1/2[-V_\infty\cos\alpha/V_T + \sqrt{(V_\infty\cos\alpha/V_T)^2 + 4w_t/V_T(x - w_t/V_T)}] \quad (15)$$

Goldstein's vortex theory relates w_t to the bound circulation, Γ , around any blade station given by the relation

$$B\Gamma = 2\pi r \cdot 2w_t F \quad (16)$$

where F is the Prandtl's tip loss factor and is given by equation (14).

From the Kutta-Joukowski theorem

$$L = \rho V_{\infty} \Gamma = 1/2 \rho V_{\infty}^2 b(r) C_{\ell} \quad (17)$$

Thus $\Gamma = 1/2 b(r) C_{\ell} V_{\infty}$

Substituting equation (17) in equation (16), the result can be expressed as

$$\sigma C_{\ell} V_e / V_T = 8xF W_t / V_T \quad (18)$$

C_{ℓ} can be calculated from

$$C_{\ell} = a_0 (\beta - \tan^{-1} (w_t / w_a)) \quad (19)$$

and from figure 5,

$$\frac{V_e}{V_T} = [((V_{\infty} \cos \alpha / V_T) + w_a / V_T)^2 + (x - w_t / V_T)^2]^{1/2} \quad (20)$$

Substituting C_{ℓ} calculated from equation (19) and V_e / V_T from (20), one obtains the value of W_t from equation (18).

Equation (15) to (20) can be solved iteratively for W_t / V_T and w_a / V_T . Once the final values of w_t / V_T and w_a / V_T are obtained, accurate values of C_{ℓ} can be determined from equation (19). The value of C_d at the particular angle $(\beta - \tan^{-1}(w_t / w_a))$ can be obtained from the C_d vs α table for the particular blade section at the given operating conditions. C_{ℓ} and C_d with other quantities are used to evaluate the thrust coefficient gradient along the radius of the propeller and is given by

$$\frac{dC_T}{dx} = (bB\pi^2 x^2 / 8R) \cdot \lambda_T \quad (21)$$

$$\lambda_T = (\cos^2 \alpha_i / \cos^2 \phi) \cdot (C_{\ell} \cos(\phi + \alpha_i) - C_d \sin(\phi + \alpha_i))$$

Equation (15) gives the axial component of the induced velocity in the propeller plane at the desired blade section.

For the axial component of the induced velocity calculated by equation (8) the blade properties were not considered by the vortex ring analysis. The axial component of the induced velocity at the propeller plane calculated from the equation (15) takes into account of the blade sectional aerodynamic properties, and represents the local flow to a greater detail rather than the global nature of the vortex ring analysis. An attempt was made to incorporate equation (15) in the calculation procedure in determining the axially induced velocity in the slipstream. In the slipstream the axial component of the induced velocities are obtained from the knowledge of the axial component of the induced velocity distribution at the propeller plane by making use of the following equation (ref. 19)

$$W_a(z) = W_a(0) \left(1 + (z/R) / \sqrt{1 + (z/R)^2} \right) \quad (22)$$

along a streamline. From the knowledge of the slipstream contraction, the local radius at any station downstream of the propeller is determined by making use of equation (12). From the coordinates of the point in the slipstream at which the induced velocities are to be determined the radius R_p from the propeller axis to the desired point is calculated. The ratio R_p/R_{local} determines the relative position of the point in the slipstream with reference to the propeller axis and R_{local} being the local contracted slipstream radius. This ratio fixes the streamline position relative to the propeller axis on which the point lies in the slipstream. Figure 6 explains this in detail. The location of this streamline on the propeller plane with respect to the propeller axis is given by $R_S = (R_p/R_{local}) \cdot R_0$. From the knowledge of the axial induced velocity distribution at the propeller plane, along the blade radius, the corresponding value for the

axial induced velocity distribution at the radius R_S on the propeller blade plane is calculated using the interpolation routine. Equation (22) is then used to determine the axial component of the induced velocity in the slipstream.

Figure 7 shows the axial component of the induced velocity distribution along the SR2 propfan blade radius calculated by the vortex ring analysis and by blade performance calculations. The vortex ring analysis predicts a constant value for the axially induced velocity component along the blade radius and this is due to the uniform loading, assumed in the formulation of the vortex ring theory. In the same figure, the results of the theory outlined in ref. 21 for propeller performance evaluation is also plotted. Figure 8 shows the calculated induced angular velocity distribution along the blade radius. The calculated values for w_a and w_t distribution using the equations (15) and (18) agree moderately well with the distribution calculated by the method of reference 21. The w_a and w_t calculation include the Prandtl's tip loss factor for simulating the three dimensional flow near the tips of the blades. The thrust coefficient, C_T , calculated by integrating the equation (21) along the blade radius for a high thrusting propeller, is overpredicted by a factor of 10 to 20 percent relative to the experimental C_T obtained by Bartlett (ref. 8). The possible reason for this behaviour is due to the theoretically computed values of C_ℓ and C_d of the blade section, used in the C_T calculation, not exactly matching with the true values of C_ℓ and C_d in the experiments.

7.2 Calculation of the Swirl Velocity

Swirl velocity is the tangential component of the induced velocity

and value of the tangential velocity at the prop plane is given by equation (18). In the slipstream of the propeller it can be shown that the circulation Γ remains constant at any station inside the slipstream (ref. 18). Due to the contraction of the slipstream, the local radius of the slipstream changes. In order to accommodate this slipstream contraction, tangential velocity increases according to the conservation of circulation for that station (ref. 18). The conservation of circulation is given by the following relation:

$$B\Gamma = 2\pi R \cdot 2w_{t_{prop}} \cdot K_{T_{prop}} = 2\pi r(z) \cdot 2w_{t_{slipstream}} \cdot K_{T_{slipstream}} \quad (23)$$

Here $K_{T_{prop}}$ and $K_{T_{slipstream}}$ are the tip loss factors at the prop and in the slipstream. $K_{T_{prop}}$ is given by equation (14). $K_{T_{slipstream}}$ is assumed to be unity. R is the radius of the propeller, $r(z)$ is the local radius of the slipstream given by equation (12) and $w_{t_{prop}}$ is the tangential velocity in the propeller plane calculated from equation (18).

Swirl angle is calculated from the expression, relating w_t , w_a and $V_\infty \cos\alpha$ and is given by

$$\text{swirl} = \tan^{-1}[2w_t / (V_\infty \cos\alpha + w_a)]$$

According to the normality relations for the axial and tangential induced velocity components, in the propeller farwake, the tangential component w_t increases from zero just ahead of the propeller to $2W_t$ just behind the propeller. This is due to the conservation of angular momentum in the wake and due to the slipstream contraction to maintain the axial velocity increase downstream of the propeller.

7.3 Treatment of the Pressure Increase in the Slipstream

From the momentum theory the propeller flow pressure difference between a point just downstream of the propeller and the farwake is given by

$$(P_2 - P_0) / \frac{1}{2} \rho_{\infty} V_{\infty}^2 = 8C_T V_T^2 / \pi^3 V_{\infty}^2 - (a^2 + 2a) \quad (24)$$

where P_2 is the pressure just downstream of the blades, P_0 is the farwake pressure, and a is given by $((V_{\infty} \cos \alpha + V_I) / V_{\infty} - 1)$ where V_I is the induced velocity at the disc and V_{∞} is the freestream velocity. The ratio of the disc area to the farwake area is known from the slipstream contraction. The static pressure increase across the entire wake is given by equation (24). From the knowledge of the area variation from the disc to the wake, the pressure increase at any other location is fixed.

The difference in static pressure at any point i inside the slipstream and freestream is given by

$$\Delta p_{i, \text{static}} / q_{\infty} = (8C_T V_T^2 / \pi^3 V_{\infty}^2 - (a^2 + 2a)) \cdot \left(\frac{A_i / A_0 - A_{\infty} / A_0}{(1 - A_{\infty} / A_0)} \right) \quad (25)$$

where A_0 is the area of the disc, A_{∞} / A_0 is the ratio of the farwake area to the disc area obtained from the momentum theory. The difference in total pressure inside the propeller wake at any point i and freestream is given by

$$\Delta p_{t, i} / q_{\infty} = \Delta p_{i, \text{static}} / q_{\infty} + \Delta q_i / q_{\infty} \quad (26)$$

where $\Delta p_{i, \text{static}}$ is given by (equation (25)). $\Delta q_i / q_{\infty}$ is expressed as $((V_{\infty} + \Delta V_I)^2 / V_{\infty}^2 - 1.0)$ where ΔV_I is the resultant of the axial induced velocity, calculated either from equation (8) or from equation (15), and the tangential swirl velocities, calculated from equation (18).

8.0 IMPLEMENTING THE PROPELLER EFFECTS INTO THE PANEL CODE AND THE CALCULATION PROCEDURE

First, from the propeller operating conditions, the axial induced velocity and the tangential component of the induced velocity along the blade radius are determined. This part of the solution needs the two-dimensional C_l and C_d characteristics of the blade section along the radius of the blade. This is calculated from the MCARF code (ref. 22) for the given Mach number, freestream Reynolds number and for a set of incidence angles. The axial induced velocity and the tangential velocity distribution are obtained by the method of iteration as explained in equation (13) to equation (20). The theoretical thrust coefficient of the propeller, operating at the given conditions, is also determined from equation (21). It is observed from the prediction of the thrust coefficient that the theory over predicts the experimental C_T by a factor of 10 to 20 percent. From the knowledge of the experimental thrust coefficient and the operating conditions of the propeller, the induced velocity at the center of the propeller given by equation (6) is determined. This is based on the one dimensional momentum theory. The axial component of the induced velocity can be calculated either by vortex ring analysis (eq. 8) or by the blade performance theory (eq. 15). The computer code has these two options and either one can be invoked.

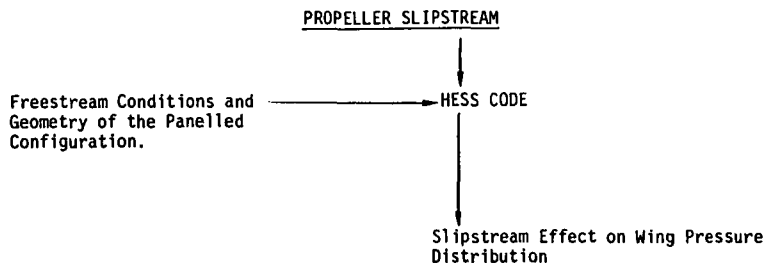
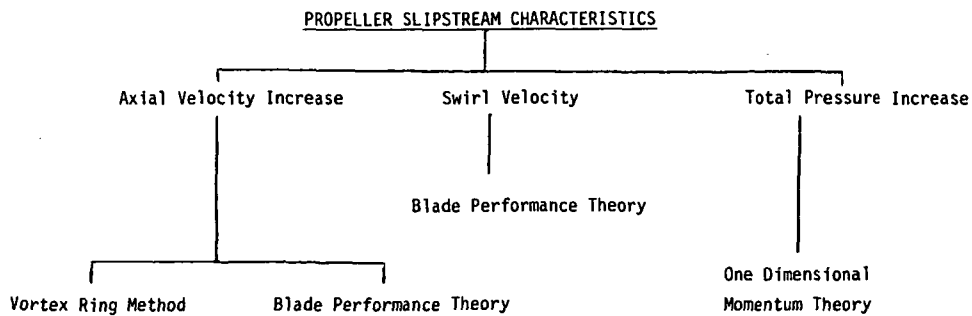
For the vortex ring analysis, the vortex ring strength is determined from the induced velocity at the center of the propeller and from the slipstream contraction ratio. Slipstream contraction ratio is calculated using equation (12). Equation (8) is used in relating the vortex ring strength to the induced velocity distribution at the center of the rotor.

Only uniform loading of the propeller has been assumed. The aircraft body is divided into a number of panels for the Hess code (ref. 23) and these panel points are defined with respect to the propeller coordinate system.

Knowing the vortex ring strength Γ_{ring} from knowledge of the load distribution on the propeller blade, the axial velocities induced at these panel points are determined by repeatedly applying equation (8) and summing these for a definite number of vortex rings. Equation (12), (15) and (22) are used if the axial component of the induced velocity by blade performance theory is required.

From the knowledge of the slipstream contraction and the local radius of the slipstream, a test is done to determine whether a panel point lies inside the slipstream for calculation of the swirl velocity effects. The swirl velocity is determined from the tangential velocity distribution along the blade radius given by equation (18) and from the conservation law of angular momentum. An interpolation routine has been used in determining the swirl velocity at a given panel point, from the tangential velocity distribution on the propeller radius. The induced velocity components are then transformed back to the aircraft coordinate system. These velocity components are the onset velocities at the panel-control points and they enter in the normal boundary condition for the Hess code calculations (ref. 9). The Hess code is run for the normal boundary condition incorporating the calculated propeller onset velocities. The pressure rise calculated from equation (26) is added to the C_p distribution obtained from the Hess code. Effectively the influence of the propeller enters in the form of onset velocity components in the Neumann boundary condition and the pressure rise obtained from the actuator disc theory

enters in the final C_p computation as an added total pressure rise due to the propeller slipstream. Effectively, the whole formulation can be defined in the following flow chart.



Method 1 - Vortex Ring Method for Axial Component of the Induced Velocity, Swirl, Total Pressure Increase.

Method 2 - Blade Performance Theory for Axial Component of the Induced Velocity, Swirl, Total Pressure Increase.

9.0 EXPERIMENTAL SET-UP

The experimental data came from a propfan investigation (ref. 8) conducted in the Langley 16 Foot Transonic Tunnel. The model consisted of an overwing nacelle, or an underwing nacelle integrated into an unswept-untapered supercritical wing mounted on the Langley 16 Foot Transonic Tunnel bifurcated strut support system. Photographs of the models in the tunnel are shown in figure 9. Figure 9a shows the photograph of the overwing nacelle/supercritical wing configuration while figure 9b shows the photograph of the underwing nacelle/supercritical wing configuration. Figure 9c and 9d show the panelled overwing nacelle/supercritical wing and underwing nacelle/supercritical wing configuration required for running the Hess code. The SR-2 propfan, 12.5 inches in diameter, was powered by an airturbine motor (ref. 24). The chord of the wing is one foot in length. Detailed information on the airfoil section is presented in reference 25. The wing had approximately 350 pressure taps to measure static pressures. The chordwise locations of the pressure taps are the same all the way across the wing, while the spanwise locations are symmetric about the centerline of the propfan. Figure 10 shows the spanwise locations of the pressure taps with respect to the propeller axis.

The model was tested from $M_{\infty} = 0.5$ to 0.8 over angles of attack ranging from 0 deg. to 3 deg. The propeller tip speed was varied from 650 to 850 ft/sec at different power loadings (ref. 8). The power loading was varied by changing the geometric pitch of the propeller. Force data were taken on the propeller so that propeller coefficients could be calculated. Model forces were calculated by pressure integration of the wing static pressure taps.

10.0 RESULTS AND DISCUSSION

The current theoretical method has been applied to an overwing nacelle on an unswept supercritical wing configuration using the panelling arrangement shown in figure 9c. Similarly the current theoretical method has also been applied to an underwing nacelle on an unswept supercritical wing configuration using the panelling shown in figure 9d. A 12.5 inch diameter propeller with eight blades is considered for the calculations.

For this investigation the propfan rotation was clockwise as viewed from the rear.

The calculations have been carried for the following cases:

- (1) wing with bifurcated support system
- (2) wing/overwing-nacelle with bifurcated supported system
- (3) wing/overwing-nacelle/propeller at various power levels with bifurcated support system
- (4) wing/underwing-nacelle with bifurcated system
- (5) wing/underwing-nacelle/propeller at various power levels with bifurcated support system.

10.1 Wing Alone Comparisons

Figure 11 shows the C_p comparison of the theory with the experiments for case (1), namely the straight wing with the bifurcated support system. While the predicted upper surface pressure distributions agree well with the experiments, the predicted lower surface pressure distributions do not match well with the experiments. This is due to the boundary layer effects on the supercritical wing, which have not been taken into consideration in

the theoretical calculations. This effect is evident at all the span stations shown in figure 11. From the figure it is evident that the theory and the experiment do not compare very well. This is due to the omission of the treatment of boundary layer in the theory.

To incorporate the boundary layer effect, two different approaches have been sought. The first approach uses a two dimensional strip theory boundary layer correction (ref. 26) while the second approach solves the three dimensional compressible boundary layer equation (ref. 27). In the first approach, there are two options available. One option is to keep the original geometry of the wing section fixed and the boundary layer effects are simulated in the form of onset velocity components (blowing or suction) on the selected control points on the wing section. Then carry out the inviscid analysis for the original wing section as if the wing section is immersed in a nonuniform flow field due to the boundary layer (ref. 28). The second option of the first approach is to calculate the displacement thickness on the wing section, add it to the original geometry of the airfoil, calculate the aerodynamic characteristics for the new geometry, and iterate on the lift coefficient until the convergence criteria is met. The second approach calculates the displacement thickness on the whole wing by solving the three dimensional boundary layer equations and everytime the original wing geometry is updated with the new wing geometry by adding the displacement thickness and iterating for the value of C_N till the convergent limit is obtained (ref. 27).

Figure 12 shows the pressure comparison between the strip theory boundary layer model with the experiments. The inclusion of the viscous modelling improves the accuracy of the C_p computation. From figure 12, it

is evident that the inclusion of the viscous effects is felt to a greater extent in the lower surface C_p distribution than in the upper surface.

The plots of normal force coefficient in this report have the upwash side on the left and the down wash side on the right with the nacelle centerline in the center of the plot at span station 0.0. The plots are presented so that the span values are negative on the upwash side and positive on the downwash side. Refer to figure 10.

Figure 13 shows the C_N comparison for the inviscid and viscous calculation for the straight supercritical wing alone configuration at 0.5 Mach number and angle of attack, $\alpha = 1.0$ deg. (ref. 28). It took six iterations to model the viscous effects with the transpiration boundary condition on the original wing section by the strip theory method. Actually most of the viscous effects has been modelled in the first two iteration. The other four iterations stabilizes the C_N convergence criteria. It is also of interest to note that there is not much of a difference between the 5th and 6th iteration values. Comparison of predictions using the three dimensional boundary layer model with the experiments showed slightly better agreement than the comparisons of the strip theory boundary layer modeling. However, the improved agreement does not warrant the extra computational effort required. Therefore the strip theory model is used in the present prediction method.

10.2 Wing/Nacelle Comparisons

Over Wing/Nacelle - Figure 14 shows the C_p comparisons of the theory with the experiments for case (2), namely the straight wing with overwing nacelle mounted on it. From the theoretical calculations, it is apparent

that the addition of the nacelle does not change the flow pattern very much at the span stations 1, 2, 3, 9, 10 and 11. The only significant changes to be seen are at the span stations 4, 5, 7 and 8. Figure 15 shows the C_N comparison of the theory with the experiments.

Under Wing/Nacelle - Figure 16 shows the C_p comparisons for the case (4) namely, the wing with the underwing nacelle while figure 17 shows the C_N comparisons for the same case. This computation does not include the boundary layer modelling, since at these high Mach numbers considerable difficulty was experienced in running either the three dimensional boundary layer code or the strip theory boundary layer code. From comparisons it is evident the theoretical prediction compares reasonably well with the experiments. Addition of the nacelle increases the C_N value at span station 4, 5, 7, 8 and increases the negative pressure peaks encountered on the upper surface of the wing at these span stations.

10.3 Wing/Nacelle/With Powered Propfan

10.3.1 Over Wing/Nacelle - Figure 18 shows the C_p comparison of the theory with the experiment for a high power loading of $C_T = 0.443$, calculated by the Method I (refer to the flow chart on page 29). In the calculations, the axial component of the induced velocity is calculated by the vortex ring analysis described in equation (1) thru (8). Figure 19 shows the C_p comparison for a high power loading of $C_T = 0.408$ calculated by the Method I. The comparisons are moderate. Figure 20 shows the C_p comparisons calculated by the Method II for the high thrust case with $C_T = 0.443$. Figure 21 shows the C_p comparison for a high thrust case with $C_T = 0.408$ calculated by Method II. In figure 22, C_N calculated by Method I and

Method II for $C_T = 0.443$ is shown. The Method II compares well with the experiments. Figure 23 shows the C_N given by the Method I and by the Method II for a high power loading with $C_T = 0.408$. From figure 23, it is inferred that the C_N value calculated by the Method II agree better with the experiments than the Method I. So, in all the calculations to follow, the Method II will be used for the slipstream/wing interaction.

Figure 24 shows the C_p comparison of the Method II with the experimental results for the medium power loading with $C_T = 0.338$. At span station 4 it is observed that there is a slight difference between the calculated and the measured pressure peak. The theory did predict the high pressure peak shown by the experimental results. The theory does seem to predict the correct propeller effects responsible for the pressure peak at these span stations. On the lower surface of the wing the boundary layer effects are significant. For span station 7 in the medium powered case, the agreement between theory and experiment on the lower surface is good and on the upper surface the agreement is fair. The theoretical calculations tend to show the correct pressure peaks on the lower surface. Span station 8 also shows similar trends. The theoretically calculated local angle of attack based on swirl does produce the higher negative pressure peaks in the upwash side of the wing.

Figure 25 shows the pressure comparison of the Method II with the experimental results for the low power loading with $C_T = 0.137$. The theory shows an increase in the angle of attack of span stations 3, 4, and 5 evidenced from the pressure distribution due to upwash created by the swirl. The theoretical results agree reasonably well with the experimental results at these span stations.

From the C_p distribution for the high power loadings, it can be seen that at span station 4 the theory predicts a higher pressure peak than indicated by the experiment. While the theory predicts a gradual increase in pressure peak for span station 3, 4 and 5, the experimental pressure peak was the largest at span station 4. A similar trend was found for the medium power loading, while for the low power loading the experimental pressure peaks increase gradually from span station 3. It is evident from the experimental results that the swirl component at span station 5 is less than the swirl at span station 4. But this trend is not present in the theoretical calculation. This is probably due to the theoretical prediction scheme not matching exactly the natural loading of the prop and the fact that the interference effect of the wing/nacelle on the propeller wake has not been included in the calculation. Similarly for span station 7 and 8, the theoretical calculations agree moderately well with the experiments. It is evident from the experiments that the pressure peak on the lower surface of the wing section at span station 8 is greater than at the span station 7 and the theory did not predict this effect. The comparisons at these span stations are moderate.

The greatest difference between C_p values of the wing alone and propeller-on occurred at the wing leading edge. On the upwash side there was a negative shift in C_p on the upper surface with a positive shift in C_p on the lower surface. On the downwash side the reverse was true with a positive shift in C_p on the upper surface and a negative shift in C_p on the lower surface. Again this was caused by the swirl in the propeller slipstream changing the wing local angle of attack. From the pressure coefficient comparisons it is inferred that the theory predicts the

pressure distribution with a reasonable accuracy except at low powers. At low power levels, the theory over predicts by a factor 50-60%.

Figure 26 and 27 compares the theoretical and experimental values of C_N for the wing/overwing nacelle with the low and medium power setting respectively. Similar comparison for the high power loading of the propeller are shown on figures 22 and 23. The C_N comparisons for the high power loading and for the medium power loading are reasonable while the C_N comparisons are poor for the low power loading. Figure 28 shows the ΔC_N comparisons (the difference in the C_N with respect to the wing alone C_N) of the theory to experiments. This effectively compares the interference effects caused by adding the overwing nacelle and the powered propeller to the basic wing configuration. From figure 28, it is evident that the addition of an overwing-nacelle increases the C_N at most of the span stations. Generally there was an increase in wing lift on the upwash side and a decrease in wing lift on the downwash side caused by the propeller slipstream swirl changing the local wing angle of attack. The dynamic pressure (q) was increased by the propeller which caused a lift increment across the complete span of the wing. Because the dynamic pressure and swirl effect were additive on the upwash side, the increment in lift was greater on the upwash side than the decrement in lift on the downwash side resulting in a overall increased lift coefficient due to the propeller slipstream.

As the power of the propeller increases, the theory predicts an increase in C_N at span stations 1, 2, 3, 4 and 5 and a decrease in C_N at span stations 7, 8, 9, 10 and 11. The upwash effect of the propeller is not greatly pronounced at span station 1. This is evident from the small

variation in C_N with the increase in power. At span stations 9, 10 and 11, the theory predicts only a small change in C_N as the power of the propeller increases. As the power increases the theory predicts an increase in the effective angle of attack associated with a higher swirl at span stations 2, 3, 4 and 5. At span stations 7, 8 and 9, the theory predicts a decrease in the effective angle of attack. This trend is found in the experiments as well as in the theory. For the powered propeller the rotational energy in the slipstream is high and this energy alters the lift and drag characteristics of the wing in the slipstream by increasing the suction peaks on upper surface of the outboard side as evidenced by the C_p distribution for the span station 3, 4 and 5 and reducing the negative pressure peaks on the upper surface at the inboard span stations 7, 8, 9 and this eventually decreases the values of the C_N .

10.3.2 Underwing-Nacelle - Figure 29 and 30 shows the C_p comparisons for the case (5), namely the wing/underwing nacelle/powered propeller. The computations for this case does not include the strip boundary layer modelling due to the difficulties encountered in the boundary layer calculations at high subsonic free Mach numbers of about 0.7. In spite of the inviscid modelling, the C_p comparisons shown in figure 29 and in 30 are quite good. It is interesting to note from figure 29 that the experimental pressure distribution indicate a shock at the leading edge portions of the wing sections, located in the upwash side of the propeller at span stations 3 and 4 and similar shock effect is found on the lower surface of the wing section, situated in the downwash side especially at span stations 7 and 8. Other than this effect, the pressure distribution very much look similar to the overwing nacelle case. Figure 31 and 32

shows the C_N comparisons for the underwing nacelle/powered propeller and the comparisons are moderately good and the effect of the slipstream on the wing normal force coefficient is similar to the effect found with the overwing nacelle/powered propeller cases.

11.0 CONCLUSIONS AND RECOMMENDATIONS

Even though the theoretical approach described above treats the propeller wing interaction problem in an approximate manner, the results of the calculations are very encouraging. The theoretical results agree with the wind tunnel results as evidenced from the C_p and C_N comparisons for all the power levels except at the lower power level. For low power, there appears to be some discrepancy between the predicted and the experimental value of C_p and C_N and this is due to the swirl predicted by the theory. It appears from the calculations, that the theory over predicts the swirl effect at the lower power levels. It is also evident from the calculated results that inclusion of the boundary layer modelling enhances the accuracy of the calculations and the boundary layer considerably alters the flow characteristics on all the wing span stations. The swirl predicted by the blade performance theory describes the local effect of the slipstream on the immersed wing section's aerodynamic characteristics to a fair degree of accuracy. The effect of the axial induced velocity component calculated by the blade performance (Method II) theory appears to be more accurate than the effect, calculated by the vortex ring theory (Method I). Possible ways to improve the discrepancies are as follows:

- (1) Inclusion of a method for representing the effect of the wing on the propeller aerodynamic characteristics. This would require that the

calculations be made in an iterative manner between the wing and the propeller. A suitable method for treating the transonic flow over the propeller blades due to the relative velocity consisting of the high subsonic freestream and the rotational velocity should be developed for the propeller performance calculation. The applicability of the vortex relations in the localized transonic flow is questionable.

(2) Due to the high energy slipstream, even at subsonic freestream conditions, certain portions of the wing section immersed in the slipstream attains supercritical Mach numbers. The validity of the subsonic panel methods to treat the localized transonic regime are not generally accurate even in the lower range of the supercritical local Mach numbers. For accurate calculations at these high subsonic free stream Mach numbers, a transonic code (ref. 29) should be combined with the slipstream model.

(3) The three dimensional boundary layer model should be coupled with the panel code such that the iterations are carried out automatically till the C_N convergence is obtained without the user's interruption.

12.0 REFERENCES

1. Mitchell, G. A.; and Mikkelson, D. C.: Summary and Recent Results from the NASA Advanced High Speed Propeller Research Program, NASA TM-82891, June 1982.
2. Rohrback, C: A Report on the Aerodynamic Design and Wind Tunnel Test of a Propfan Model, AIAA Paper No. 76-667, presented at the AIAA/SAE 12th Propulsion Conference, Palo Alto, CA, July 26-29, 1976.
3. Baum, J. A., Dumais, P. J., Mayo, M. G., Metzger, F. B., Shenkman, A. M. and Walker, G. G.: Propfan Data Support Study, Tech. Report, NASA CR-152141, 1978.
4. Mendoza, J. P.: Interference Effects of Aircraft Components on the Local Blade Angle of Attack of a Wing Mounted Propeller, NASA TM-78587, June, 1979.
5. Fox, S. R. and Smetana, F. O.: Integration of Propeller Slipstreams into the Aerodynamic Analyses of Bodies, SAE Paper 810566, Presented at the Business Aircraft Meeting and Exposition, Wichita, KA, April 7-10, 1981.
6. Welge, H. R.: Propfan Integration at Cruise Speeds, AGARD CP 301 on "Aerodynamics of Power Plant Installation", Sept. 1981.
7. Smith, R. C., Levin, A. C.: Propfan Installation Aerodynamics of a Supercritical Swept Wing Transport Configuration, AIAA Paper 81-1563, Presented at the AIAA/SAE/ASME 17th Joint Propulsion Conference Colorado Spring, CO, July 27-29, 1981.
8. Bartlett, G.: An Experimental Investigation of Propfan Installation on an Unswept Supercritical Wing, Masters Thesis, George Washington University, Aug. 1983.
9. Hess, J. L.: Calculation of Potential Flow About Arbitrary Three-Dimensional Lifting Bodies, Douglas Aircraft Co., Report MDC-J5679-01, (Contract N00019-C-71-0524), Oct. 1972. (Available from DTIC as AD 755480.)
10. Castles, W., Jr. and Deleeuw, J. H.: The Normal Component of the Induced Velocity in the Vicinity of a Lifting Rotor and Some Examples of its Application, NACA Report 1184, 1954.
11. Heyson, H. H., and Katzoff, S.: Induced Velocities Near a Lifting Rotor-Fuselage Induced Flow Field Computational Method, NACA TR 1184, 1954.
12. Freeman, C. E.: Development and Validation of a Combined Rotor-Fuselage Induced Flow Field Computational Method, NASA TP-1656, AVRADCOM TR 80-B-3, 1980.

13. Kellogg, O. D.: Foundation of Potential Flow Theory, Frederick Ungar Pub. Co., 1929.
14. Harlock, J. H.: Actuator Disk Theory, McGraw Hill, NY, 1978.
15. Glauert, H.: Airplane Propellers. Airscrew Theory, Vol. IV of Aerodynamic Theory, Div.: L. Chapter I, Sec. 4, W. F. Durand, ed. Julius Springer (Berlin), 1935, pp. 179-180.
16. Heyson, H. H.: A Brief Survey of Rotary Wing Induced Velocity Theory, NASA TM-78741, 1978.
17. Heyson, H. H.: A Note on the Mean Value of Induced Velocity for a Helicopter Rotor, NASA TN D-240, May 1960.
18. Aljabri, A. S.: The Prediction of Propeller/Wing Interaction Effects, Paper Presented in the 13th Congress of the International Council of the Aeronautical Science, AIAA Aircraft Systems and Technology Conference, Aug. 22-27, 1982, Seattle, WA.
19. McCormick, B. W.: Aerodynamics of VSTOL Flight, Academic Press, New York. London 1967.
20. Stepniewski, W. Z.: Rotary Wing Aerodynamics, Vol. I, Basic Theories of Rotor Aerodynamics (with Application to Helicopters) NASA CR-3082, 1979.
21. Gillian, Ronnie E.: Aircraft Noise Prediction Program User's Manual, NASA TM-84486, 1982.
22. Morgan, H. L., Jr.: A Computer Program for the Analysis of Multi-Element Airfoils in Two Dimensional Subsonic, Viscous Flow, NASA SP 347, Pt. II, pp. 713-747, 1975.
23. Mack, D. P.: Calculation of Potential Flow About Arbitrary Three-Dimensional Lifting Bodies, Users Manual, McDonnell Douglas Report No. MDC J5679-02, Oct. 1972.
24. Jeracki, R. J., Mikkelsen, D. C., and Blaha, B. J.: Wind Tunnel Performance of Four Energy Efficient Propellers Designed for Mach 0.8 Cruise, NASA TM 79124, 1979.
25. Bartlett, D. W.; and Patterson, J. C., Jr.: NASA Supercritical-Wing Technology, NASA TM 78731, 1978.
26. Kjelgaard, S. O.: Evaluation of a Surface Panel Method Coupled with Several Boundary Layer Analyses, AIAA Paper 83-0011, presented at the AIAA 21st Aerospace Sciences Meetings, Jan. 10-13, 1983, Reno, Nevada.
27. Street, C. L.: Viscous - Inviscid Interaction for Transonic Wing-Body Configurations Including Wake Effects, AIAA Journal Vol. 20,

No. 7, pp. 915, July, 1982.

28. Chandrasekaran, B.; and Bartlett, G.: Method for Calculating Effects of a Profan on Aircraft Aerodynamic at Subsonic Speeds, AIAA-83-1216, presented at AIAA/SAE/ASME 19th Joint Propulsion Conference, June 27-29, 1983, Seattle, Washington.
29. Caughey, D. A.; and Jameson, A.: Numerical Calculation of Transonic Potential Flow About Wing-Body Combinations, AIAA Journal, Vol. 17, No. 2, pp. 175-181, 1979.

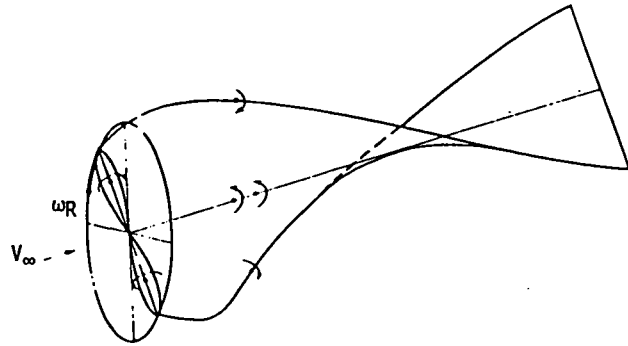
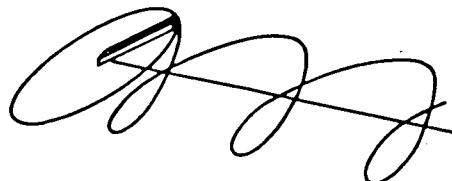
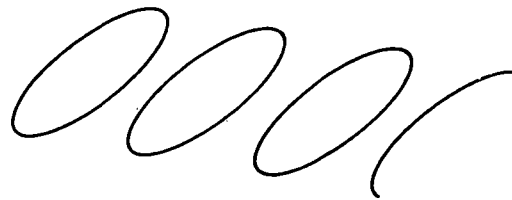


Figure 1. Bound and Trailing Vortex System for a Propeller.



(a) Spiral Vortex System



(b) Ring Vortex System

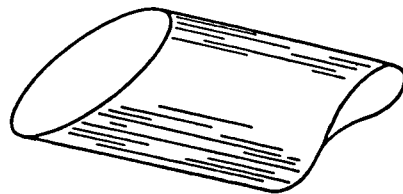


Figure 2. Wake System for Slipstream Model.

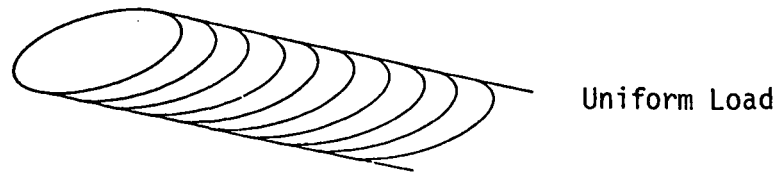


Figure 3. Vortex Ring Modelling for the Propeller Wake.

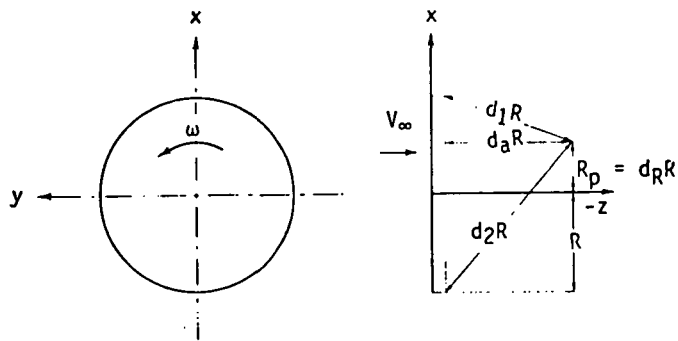


Figure 4. Definition of the Parameters Associated with the Vortex Tube Modelling.

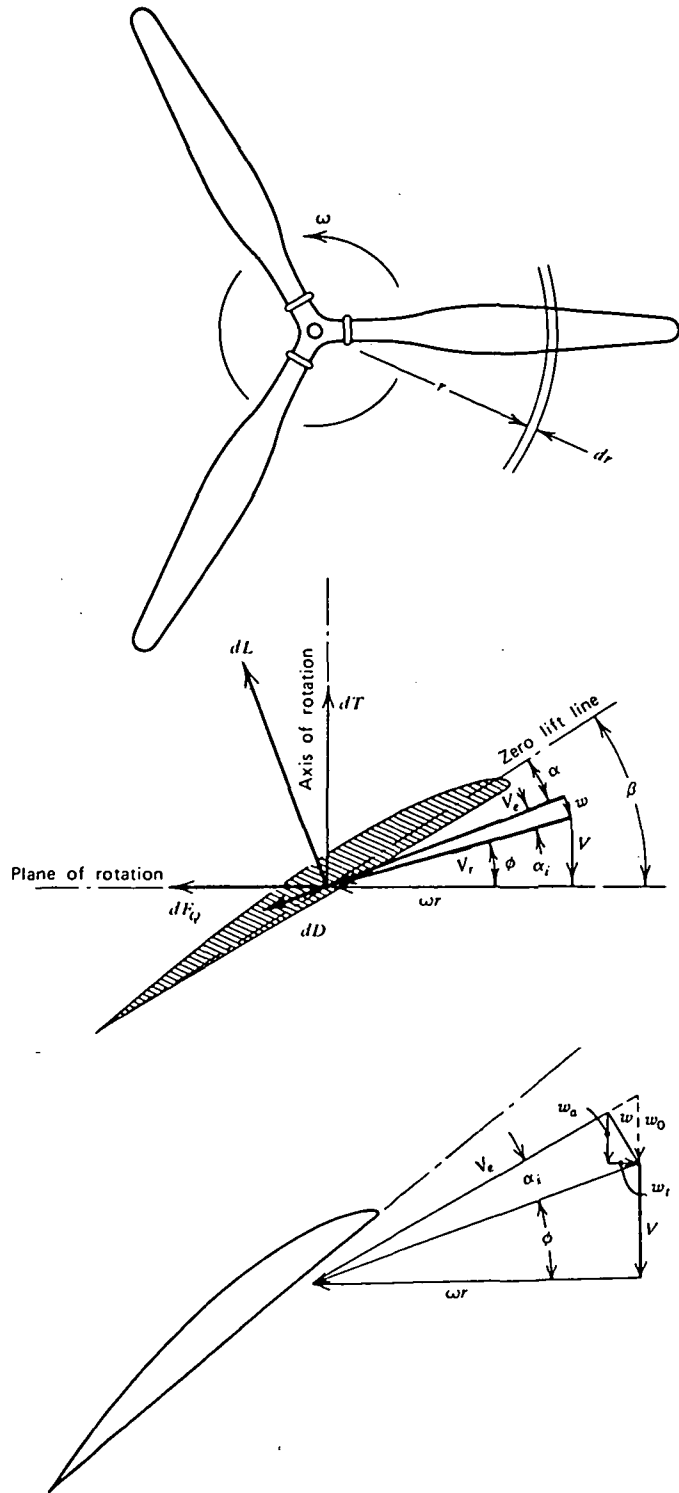


Figure 5. Velocity Diagram for a Blade Element Showing Induced Velocity Components.

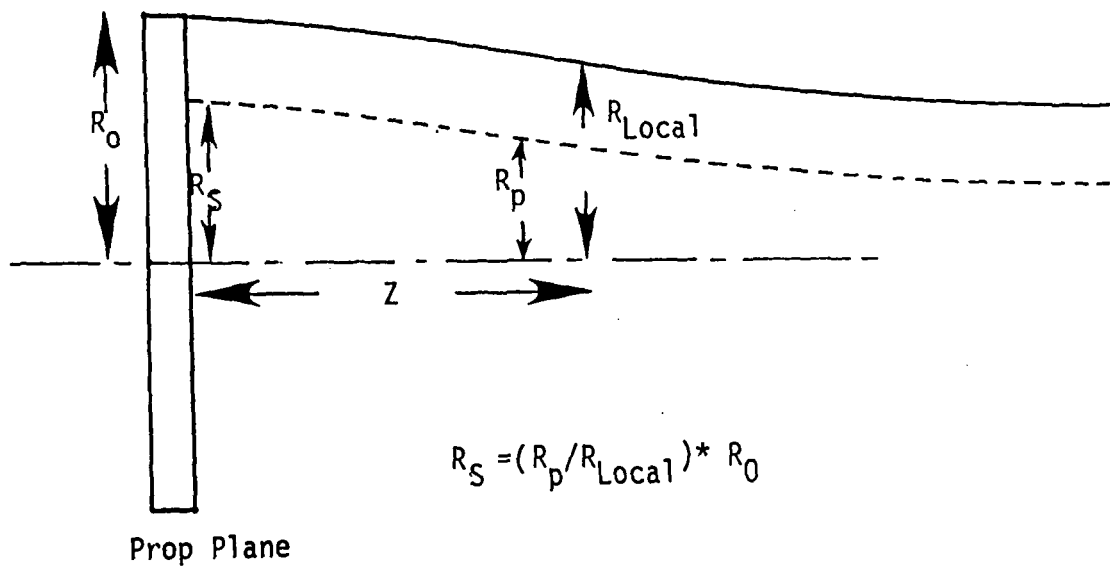


Figure 6. Definition of slipstream parameters.

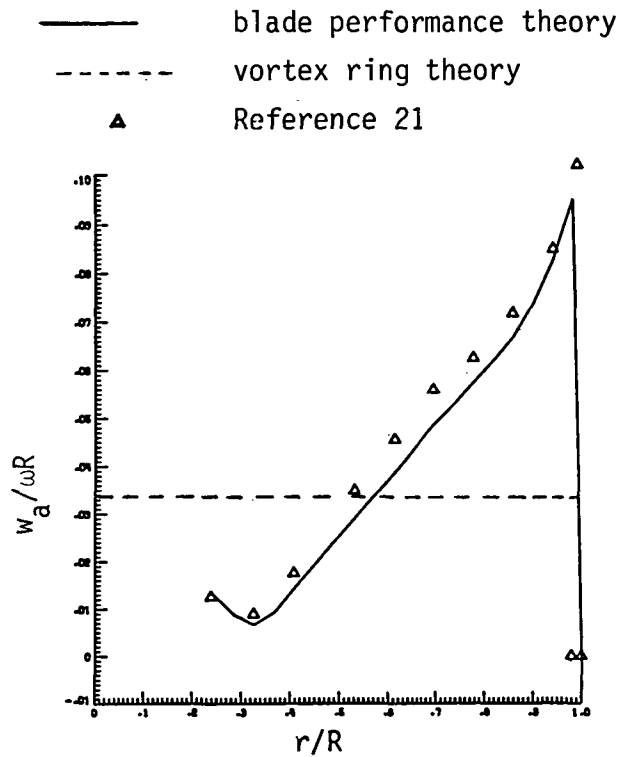


Figure 7. Axial induced velocity distribution along the blade radius of the propfan for a high thrusting load with $C_T = 0.343$, $M_\infty = 0.5$, $\alpha = 2.990$, $J = 2.367$, $\beta = 52.5$ degrees.

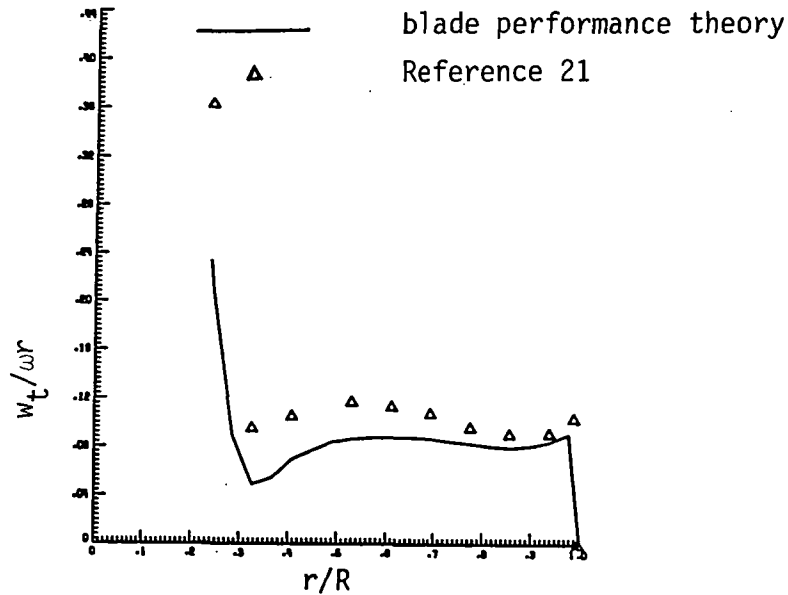
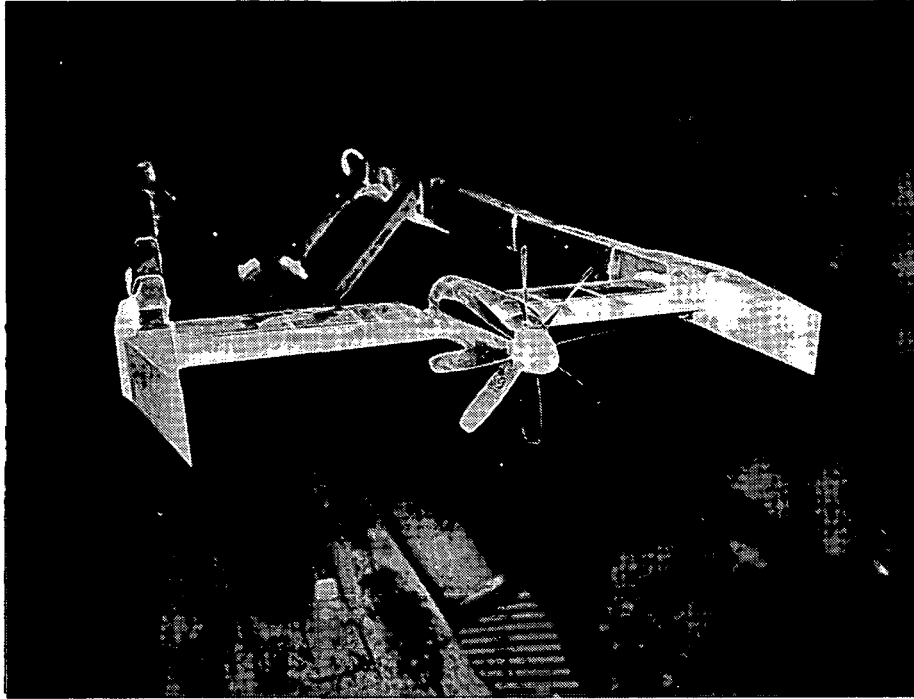
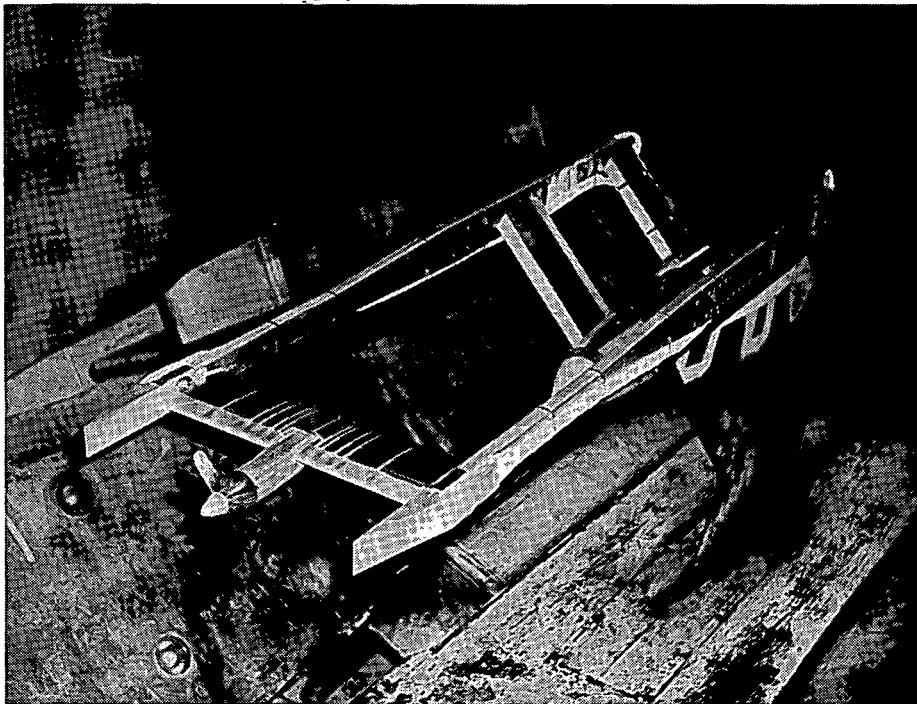


Figure 8. Induced angular velocity distribution along the blade radius of the propfan for a high thrusting load with $C_T = 0.343$, $M_\infty = 0.5$, $\alpha = 2.990$, $J = 2.367$, $\beta = 52.5$ degrees.

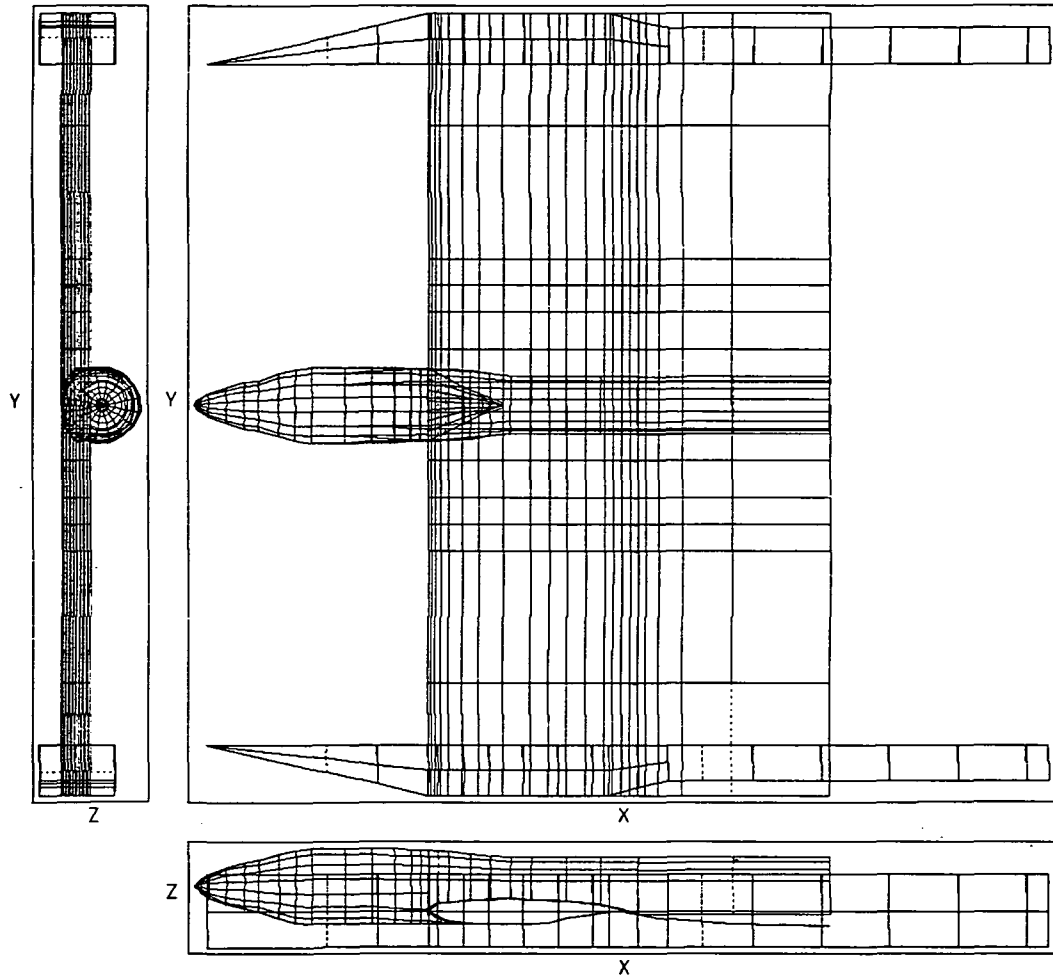


(a) Photograph of the wing/overwing nacelle/propeller in the wind tunnel.



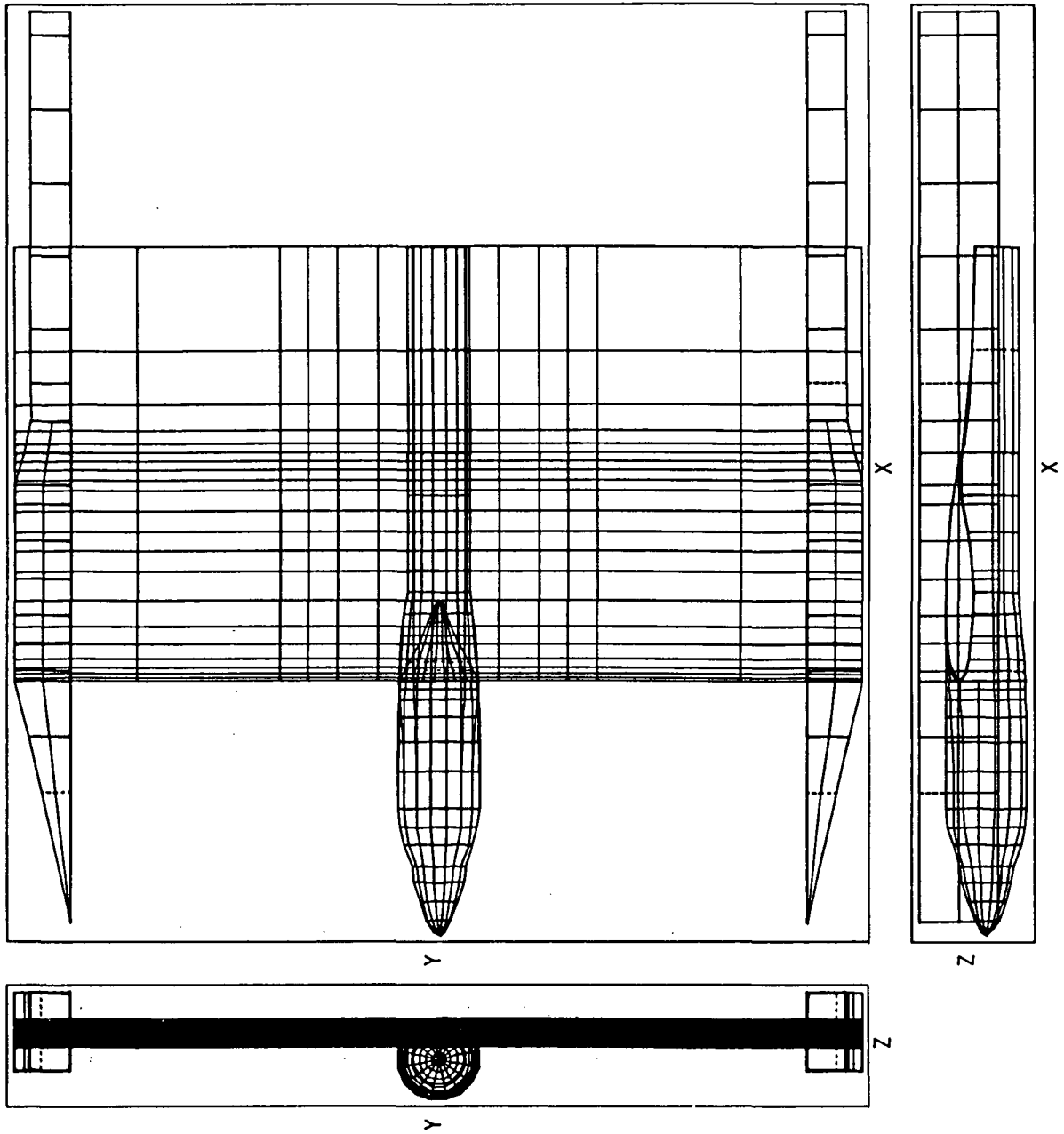
(b) Photograph of the wing/underwing nacelle/propeller in the wind tunnel.

Figure 9. Wing/nacelle/propfan configuration and the panelling used.



(c) Panelling for the wing/overwing nacelle with bifurcated system.

Figure 9. Continued.



(d) Panelling for the wing/underwing nacelle with bifurcated support system.

Figure 9. Concluded.

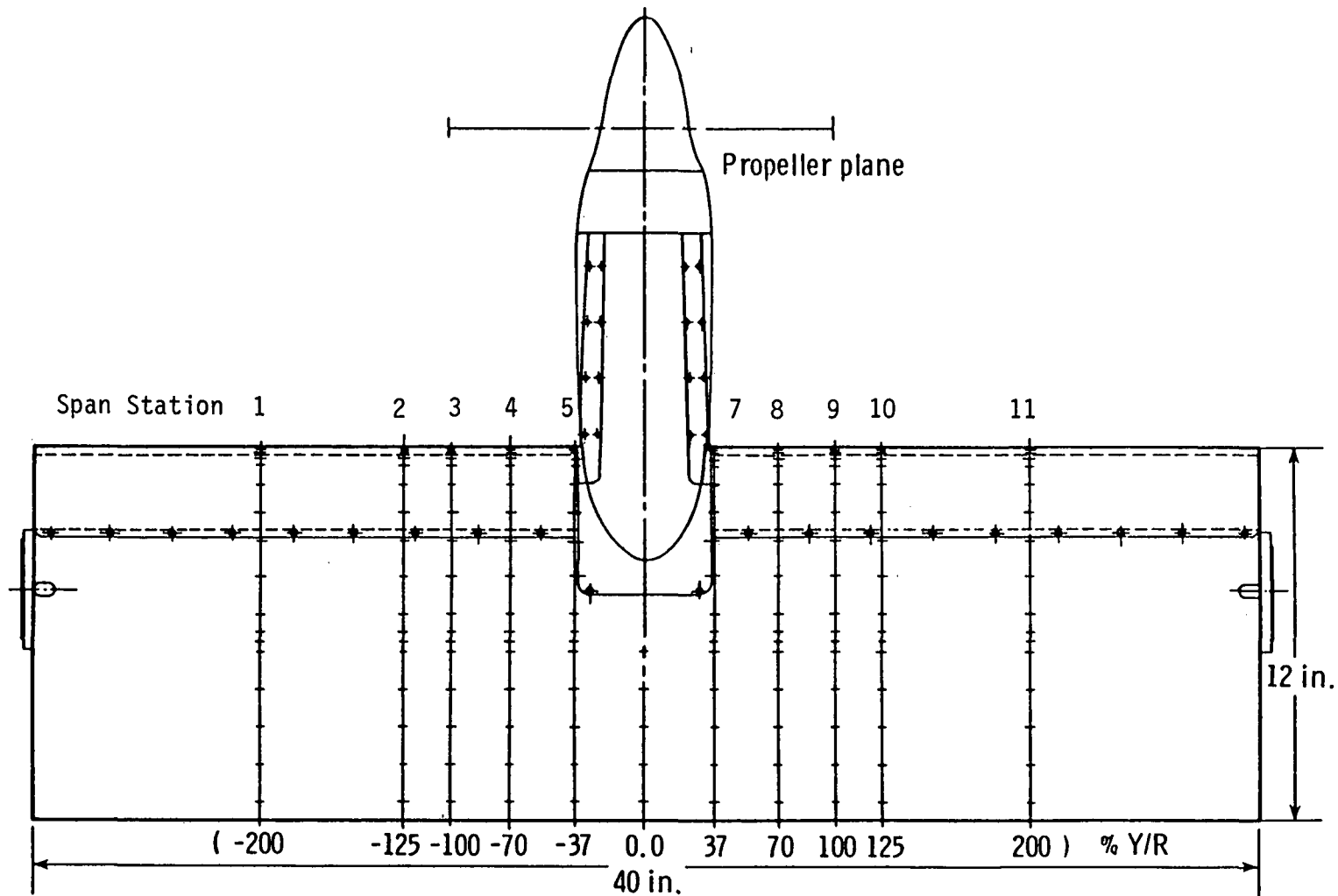


Figure 10. Model planform.

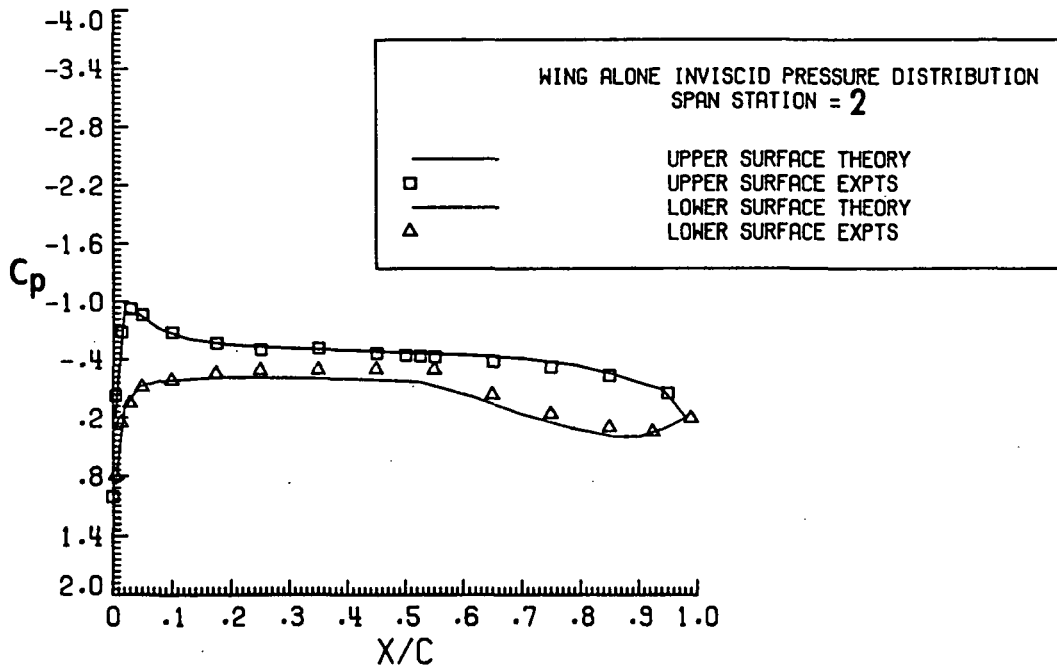
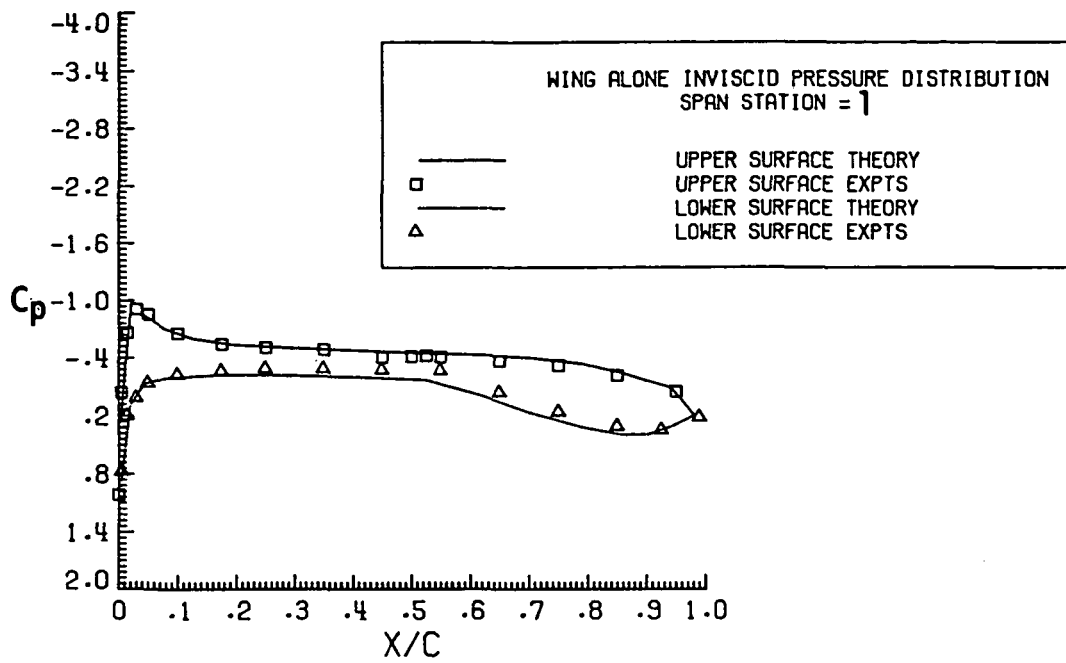


Figure 11. C_p Comparison for the Wing Alone Configuration at $M_\infty = 0.50$, $\alpha = 1.0$.

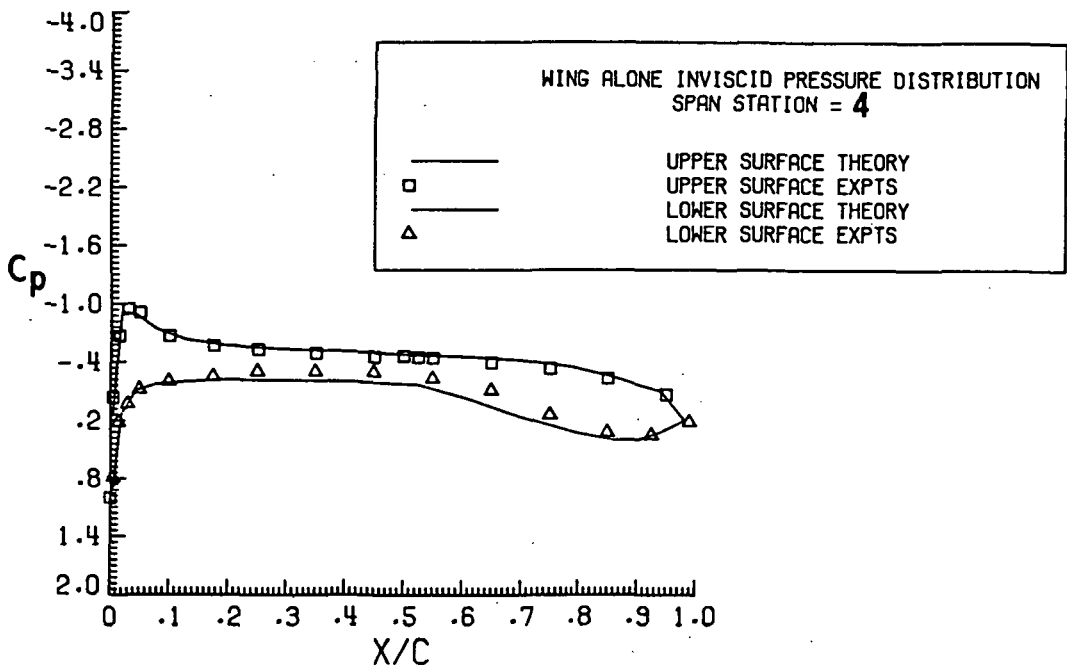
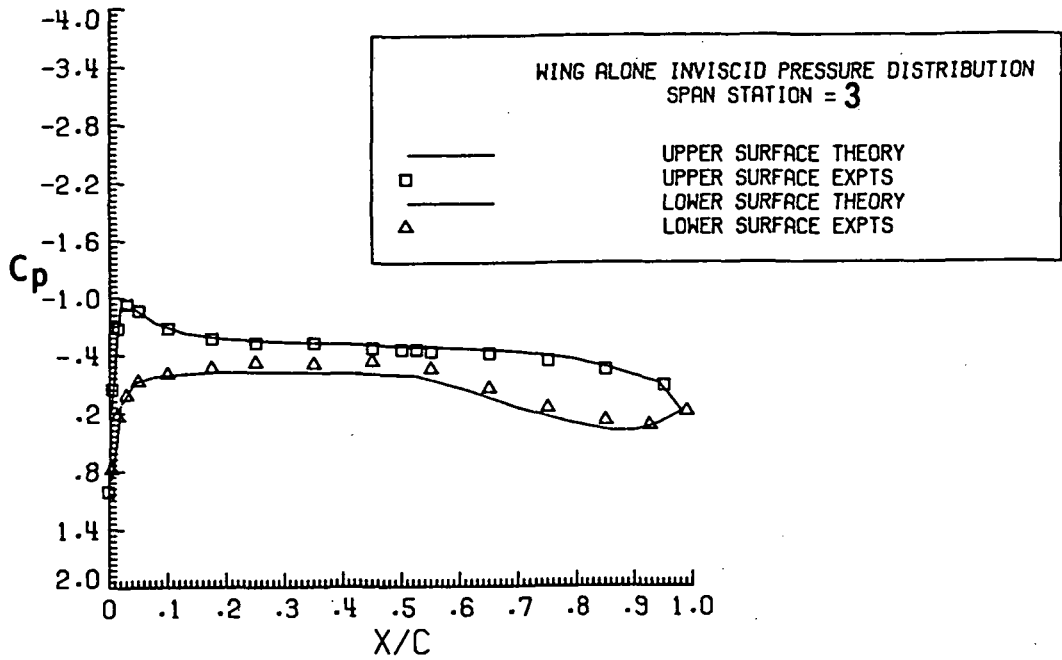


Figure 11. Continued.

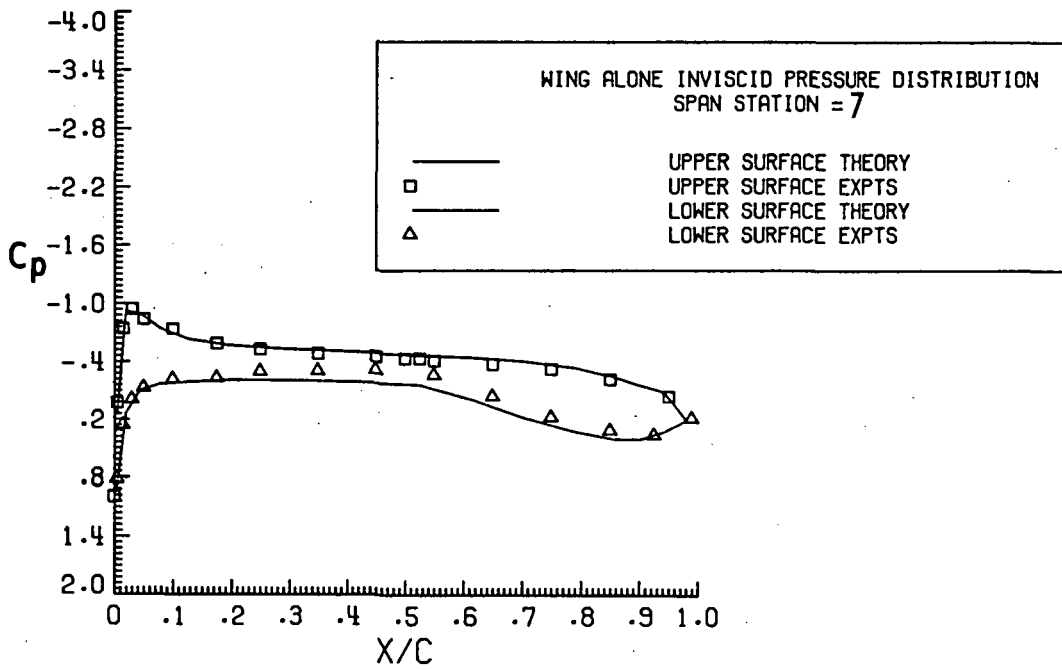
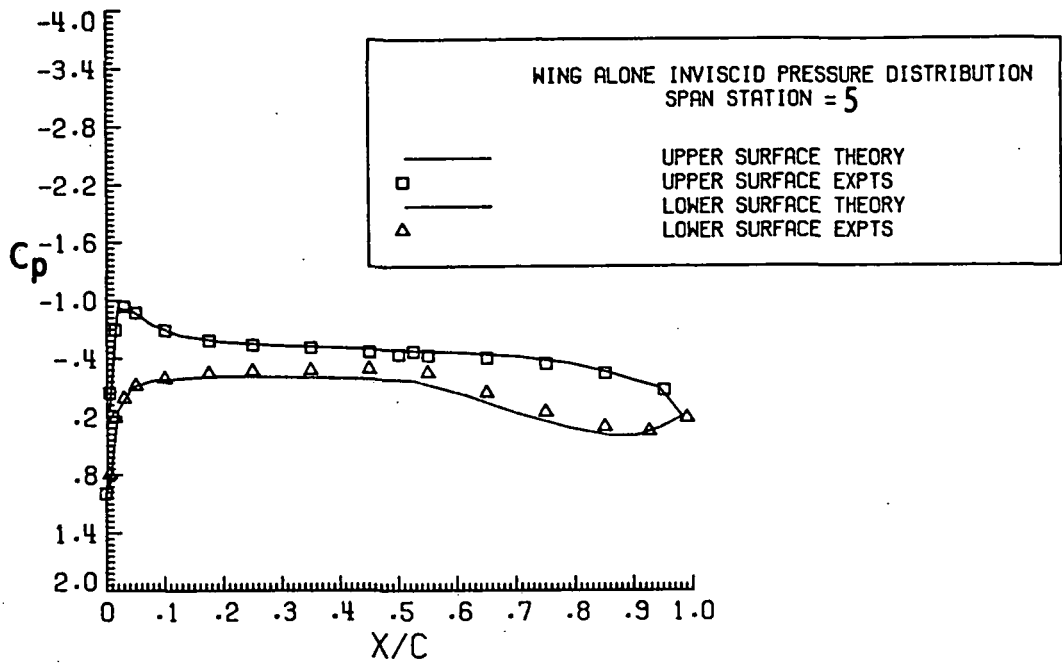


Figure 11. Continued.

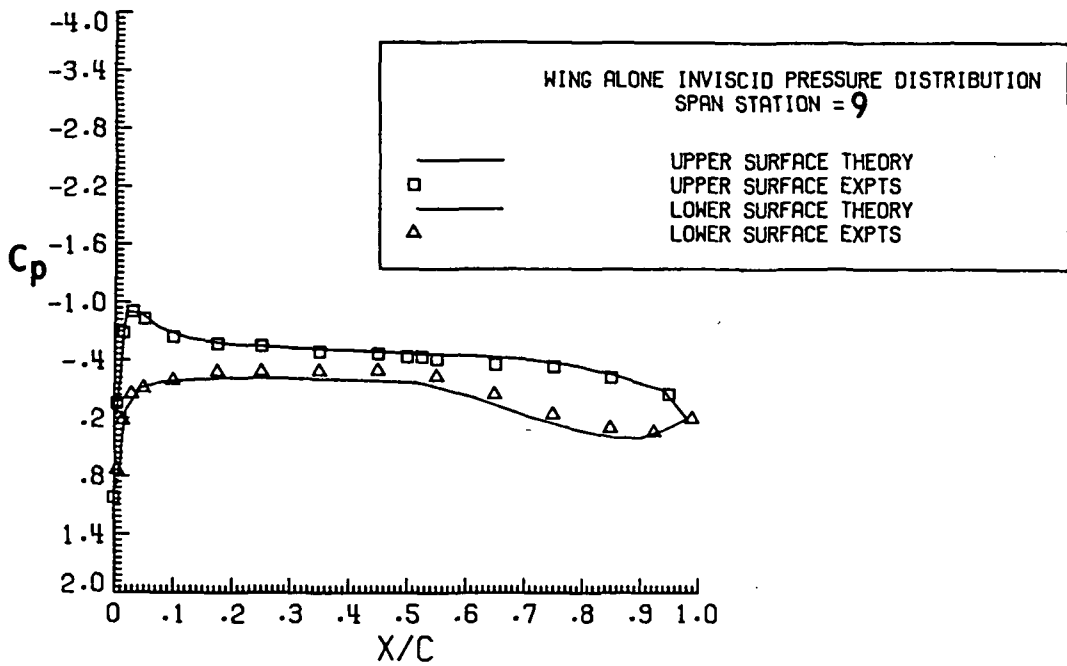
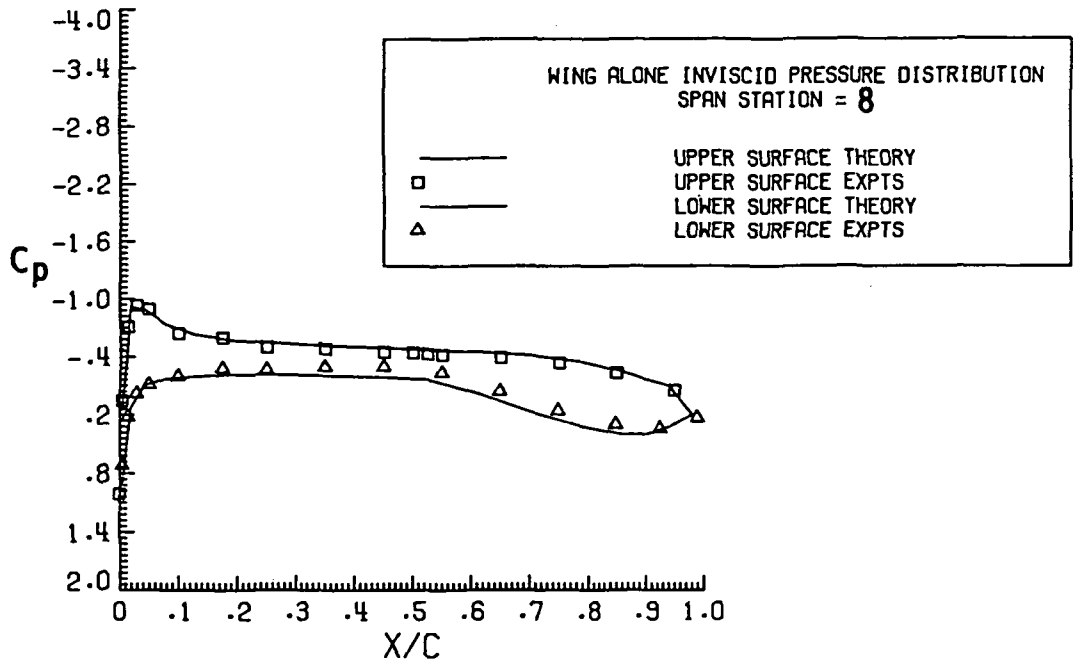


Figure 11. Continued.

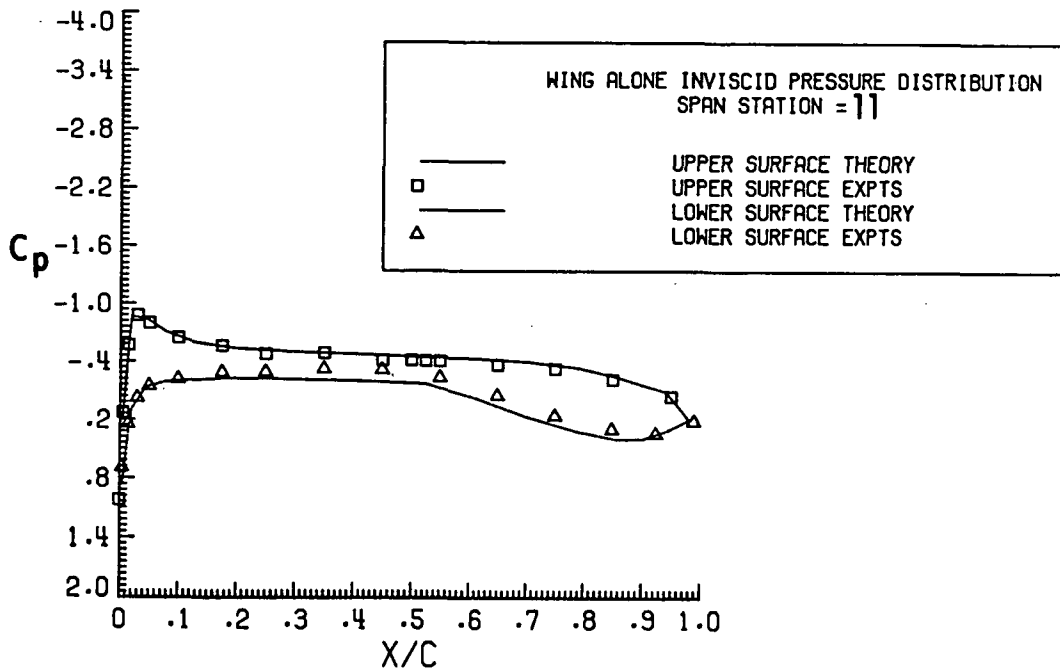
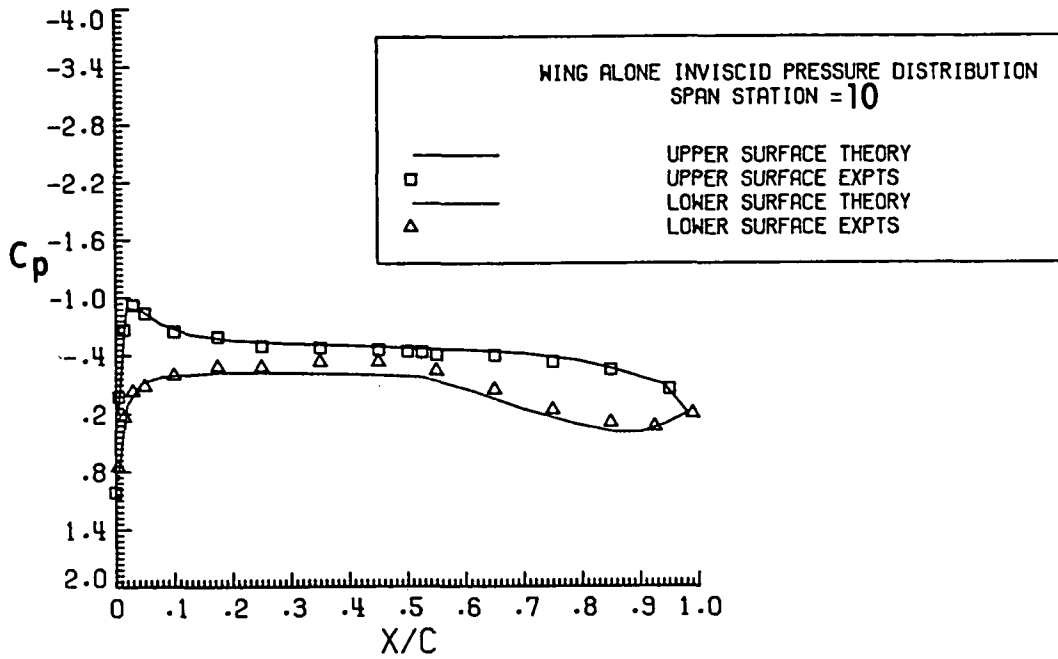


Figure 11. Concluded.

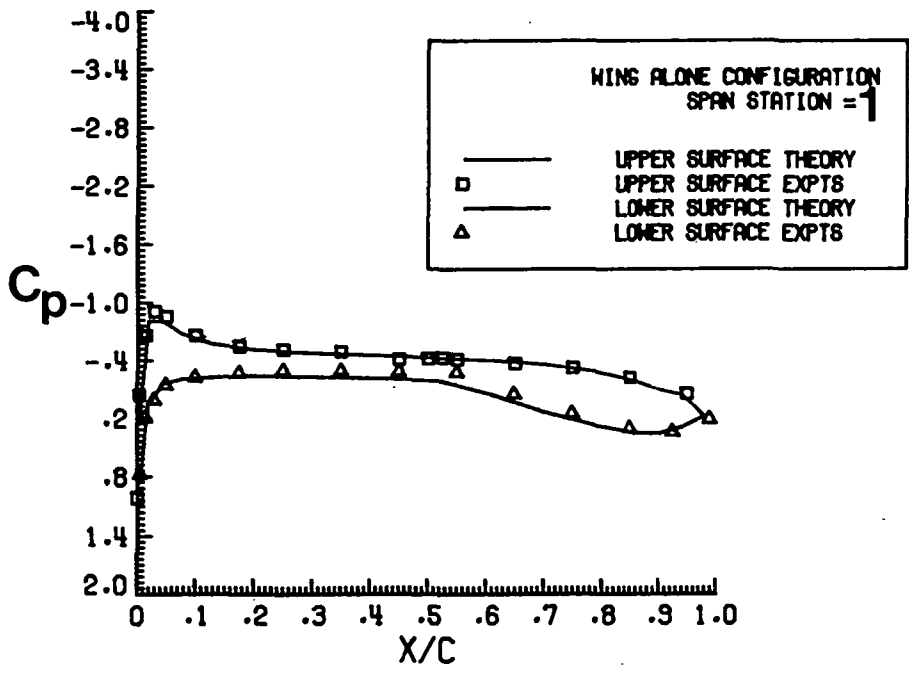


Figure 12. C_p Comparison for Wing Alone with Strip Boundary Layer Correction at $M_\infty = 0.5$, $\alpha = 1.0$ degree.

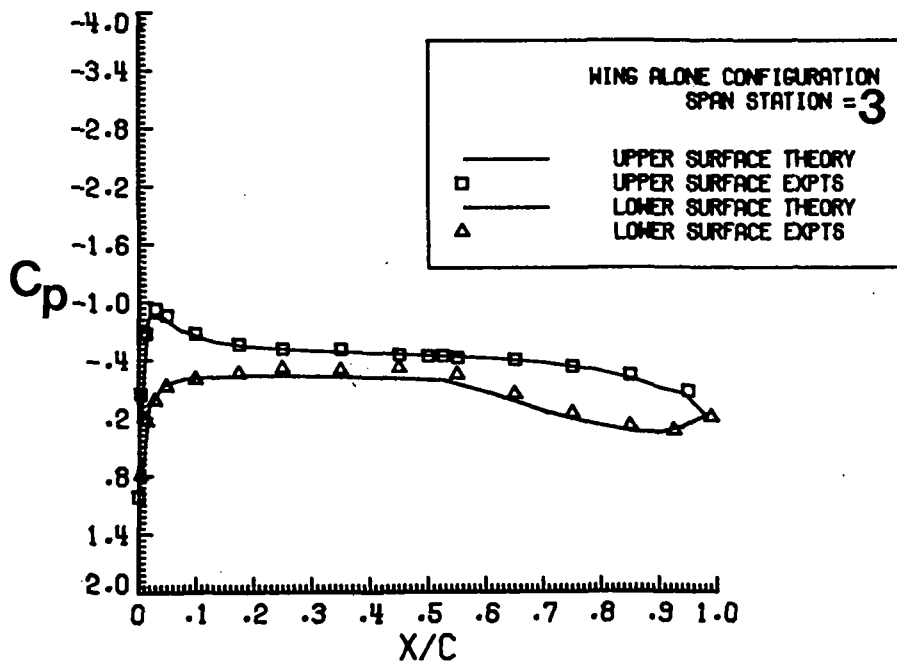
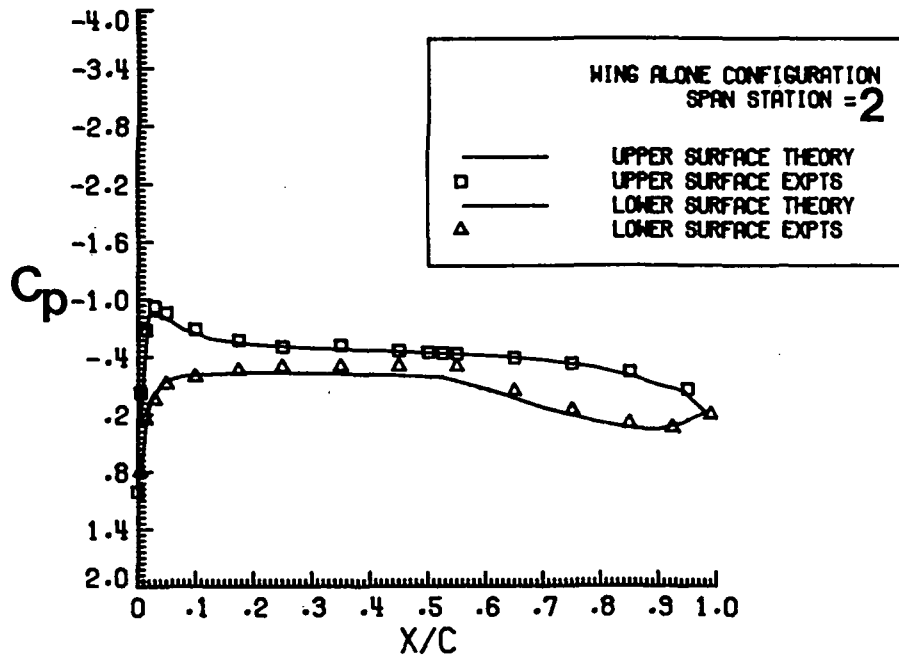


Figure 12. Continued.

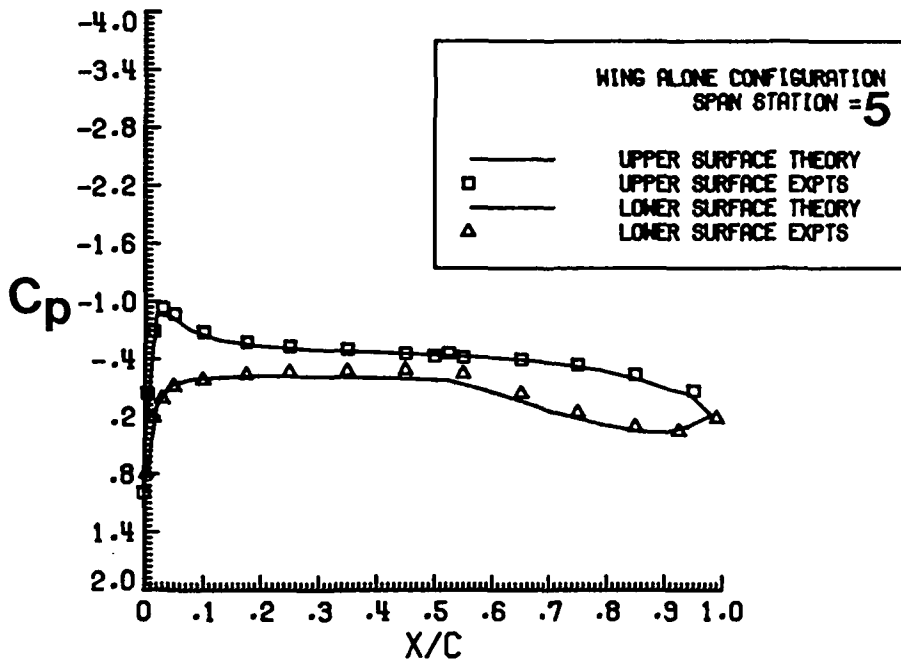
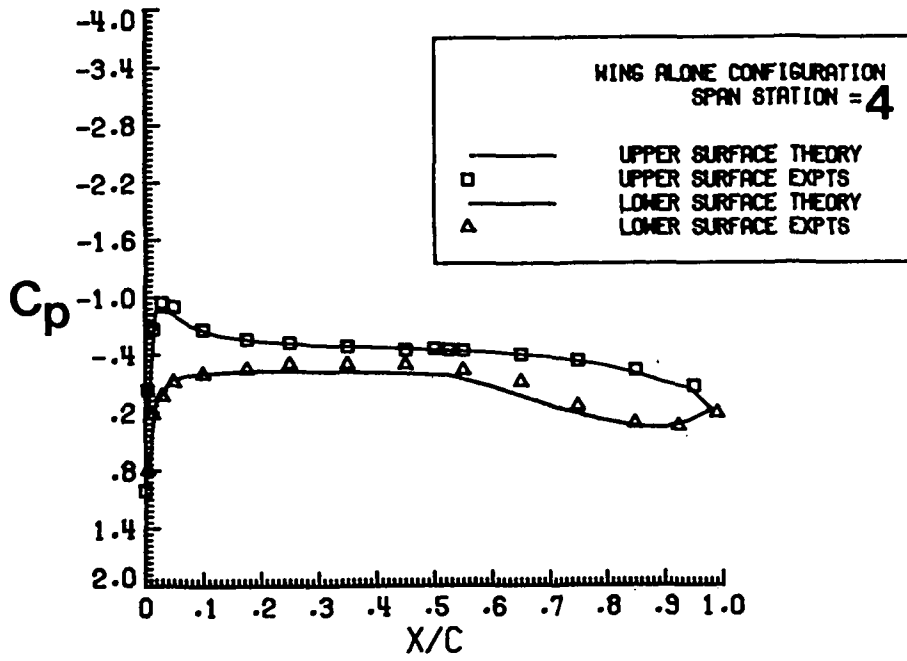


Figure 12. Continued.

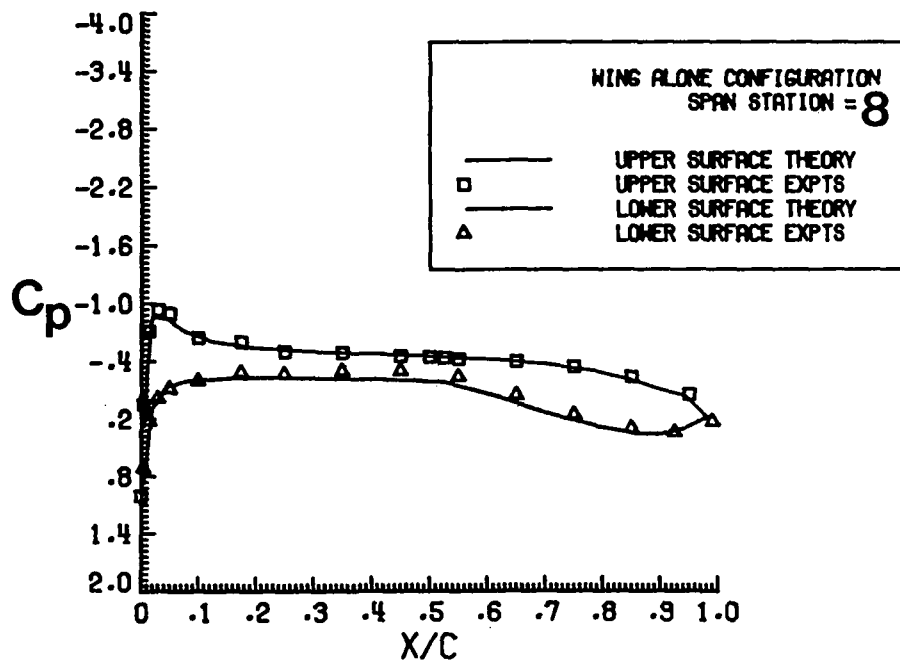
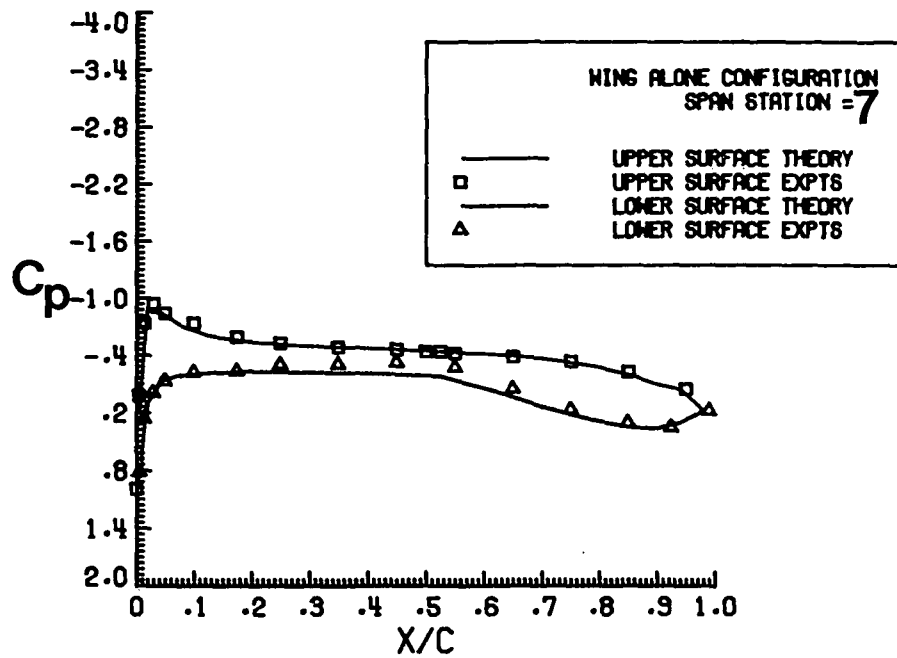


Figure 12. Continued.

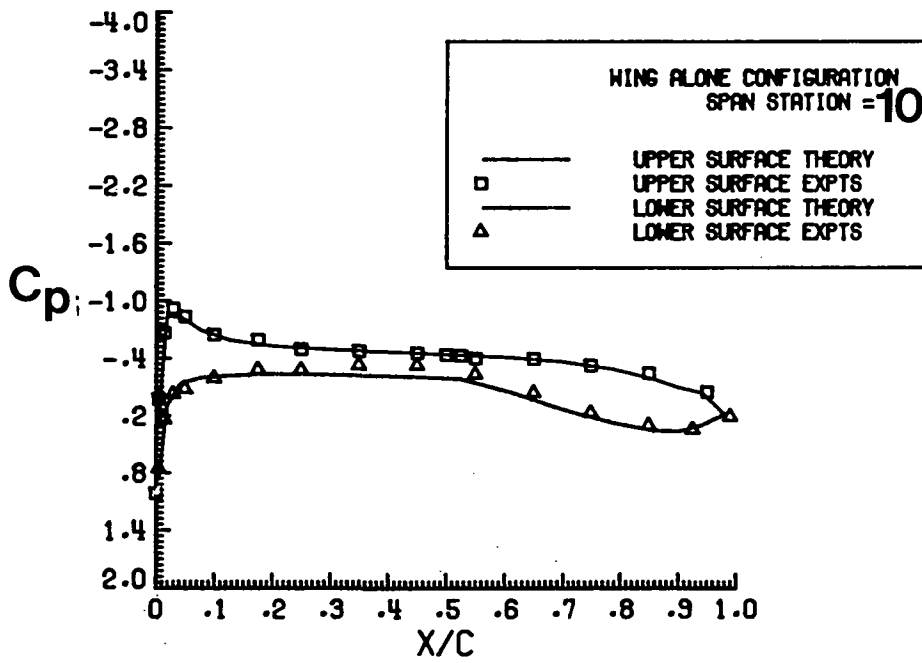
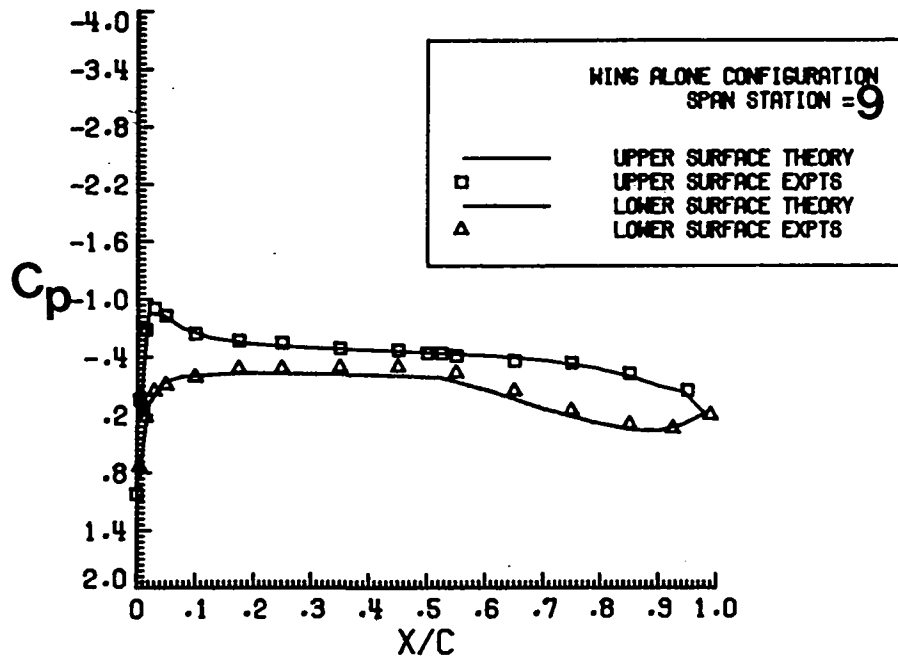


Figure 12. Continued.

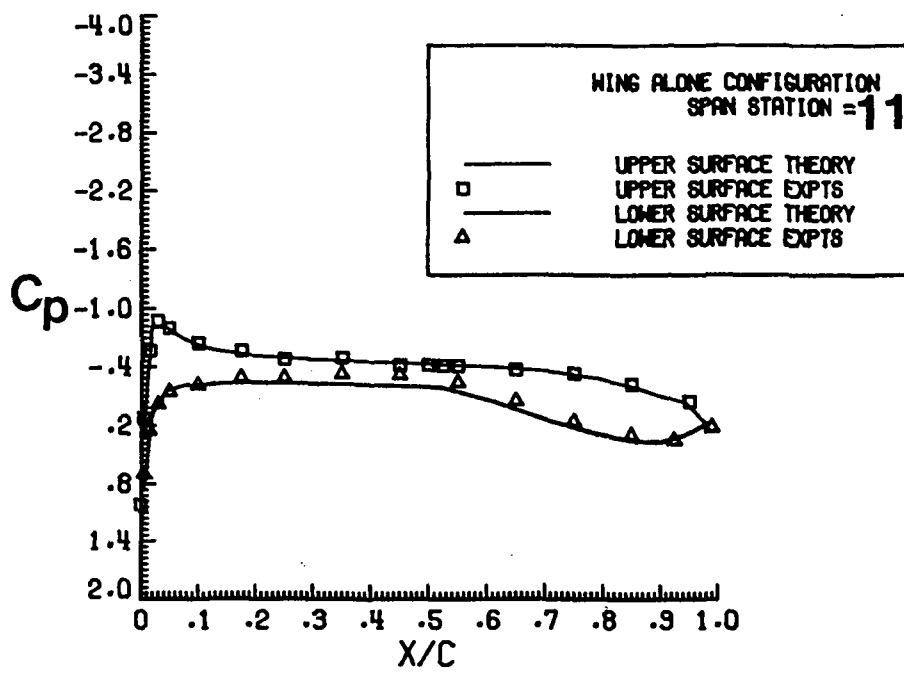


Figure 12. Concluded.

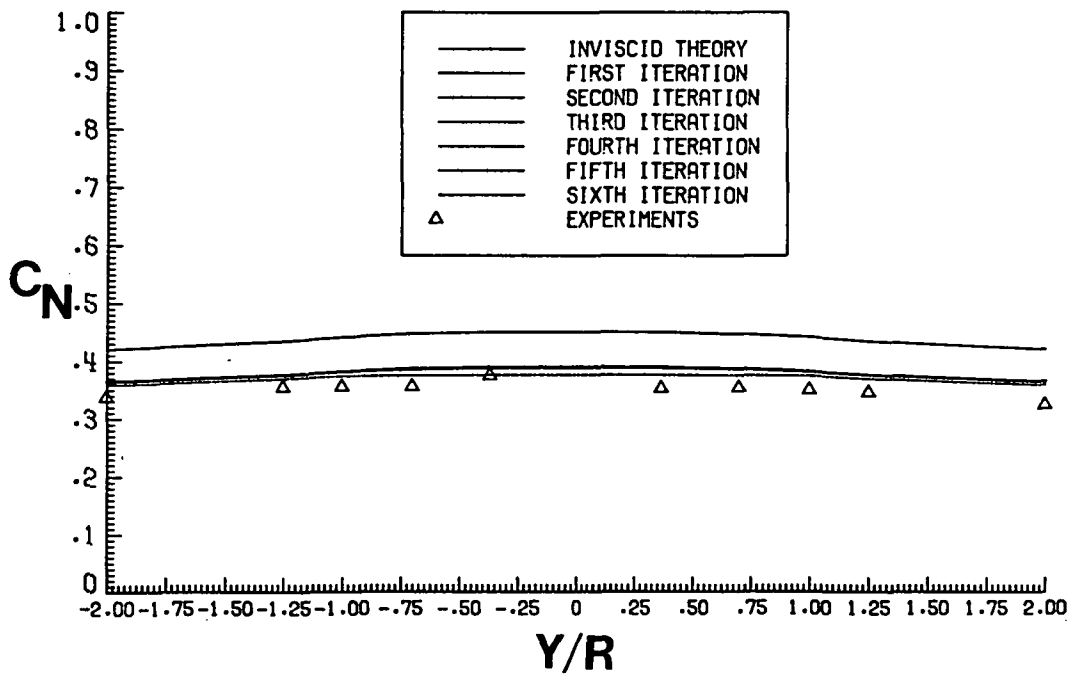


Figure 13. C_N Comparison for the Wing Alone with Strip Boundary Layer Correction, $M_\infty = 0.5$, $\alpha = 1.0$ degree.

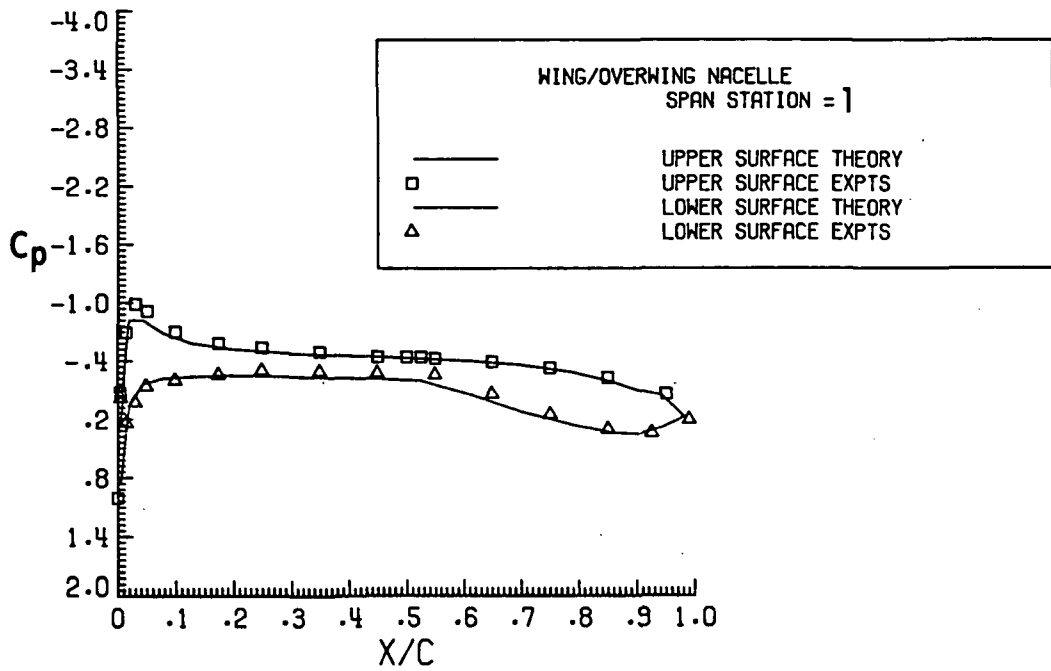


Figure 14. C_p Comparisons for Wing/Overwing Nacelle with Strip Boundary Layer Correction, $M_\infty = 0.5$, $\alpha = 1.0$ degree.

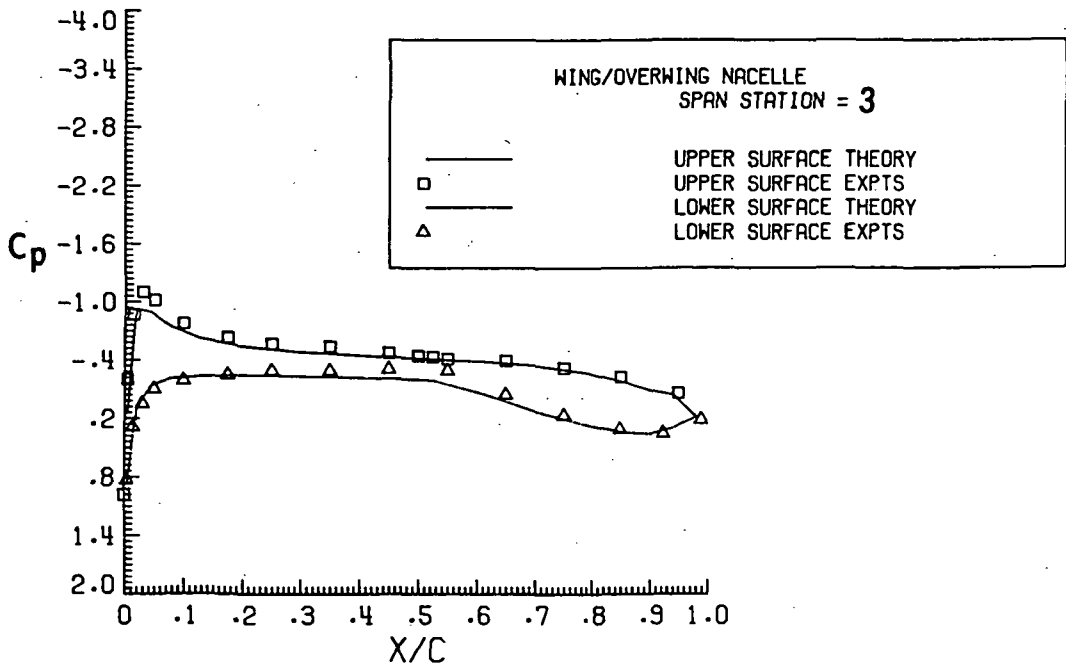
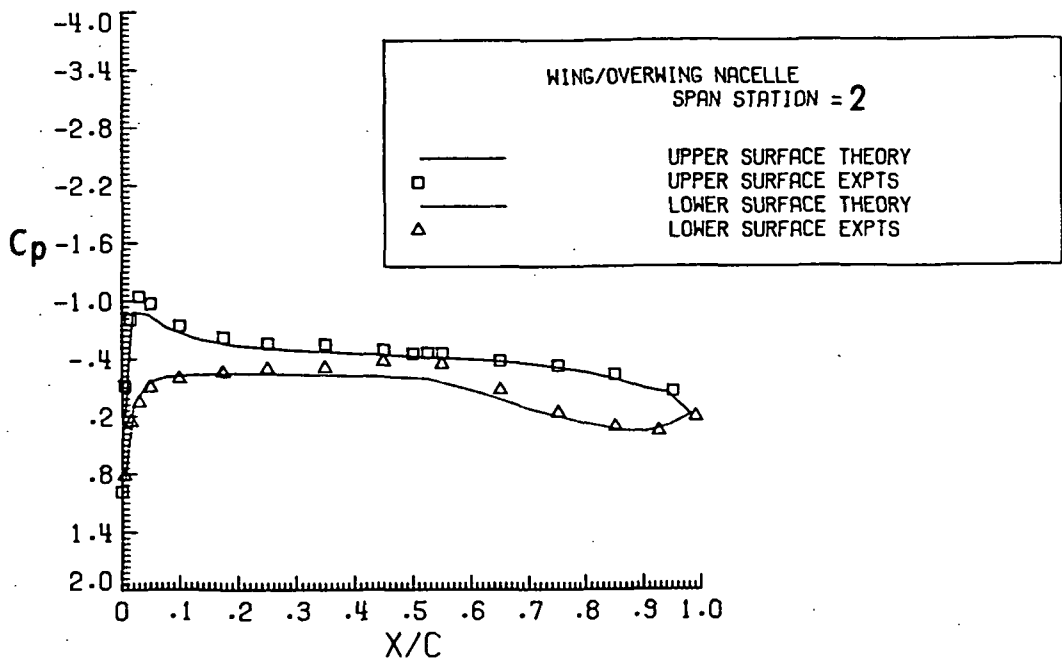


Figure 14. Continued.

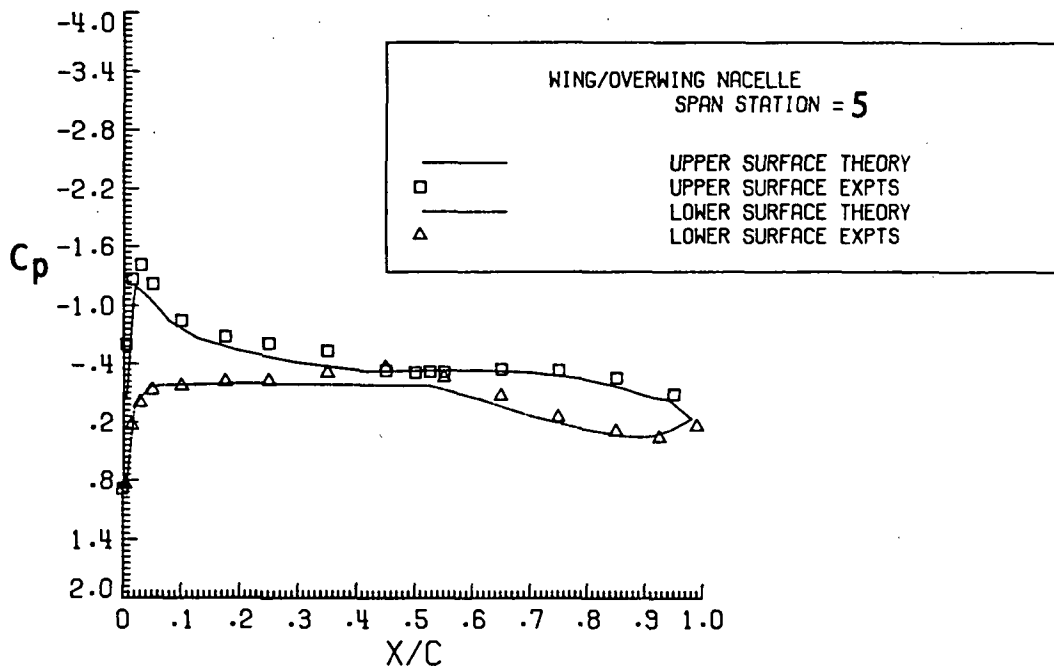
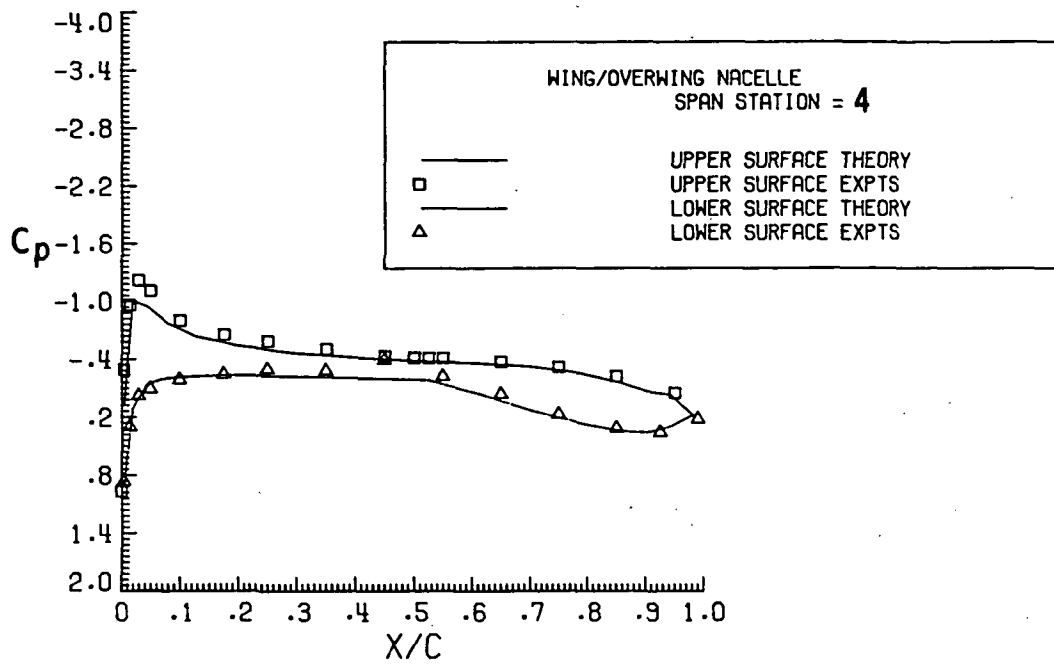


Figure 14. Continued.

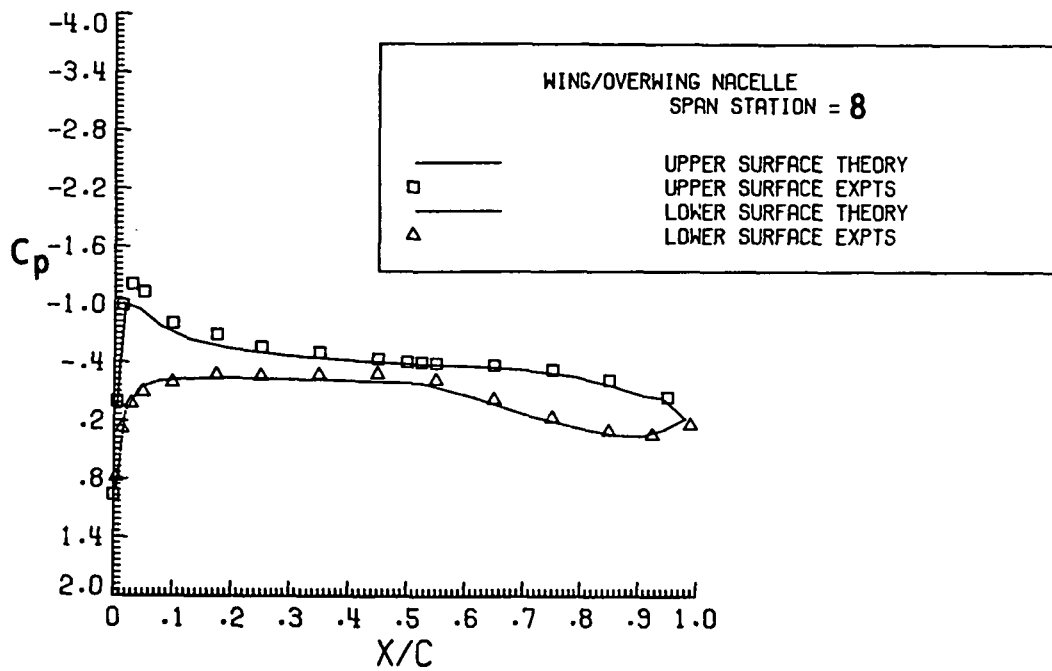
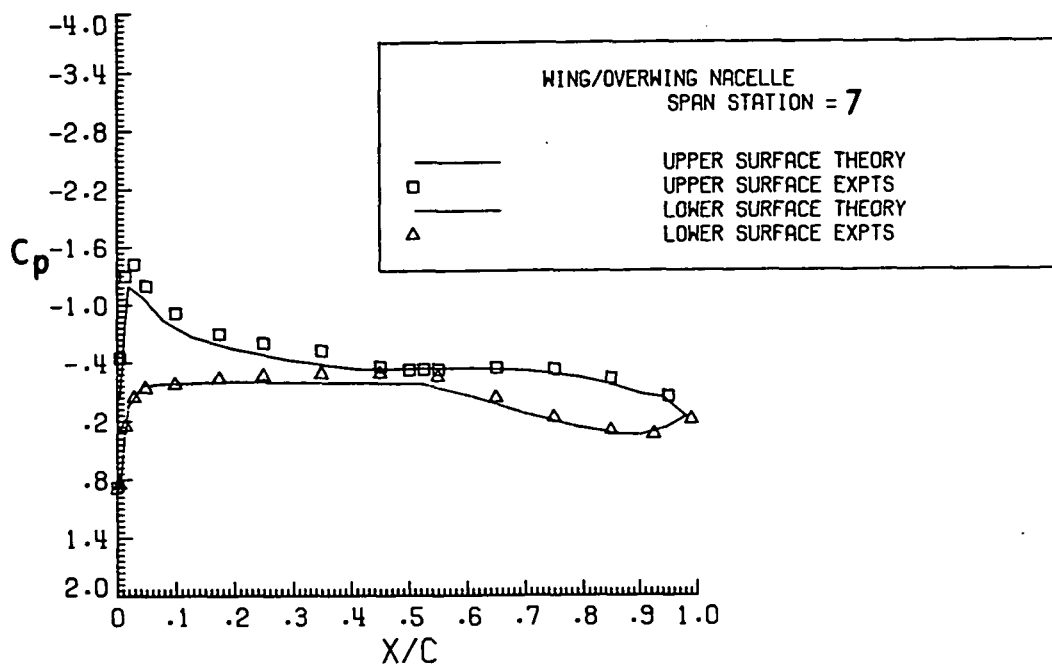


Figure 14. Continued.

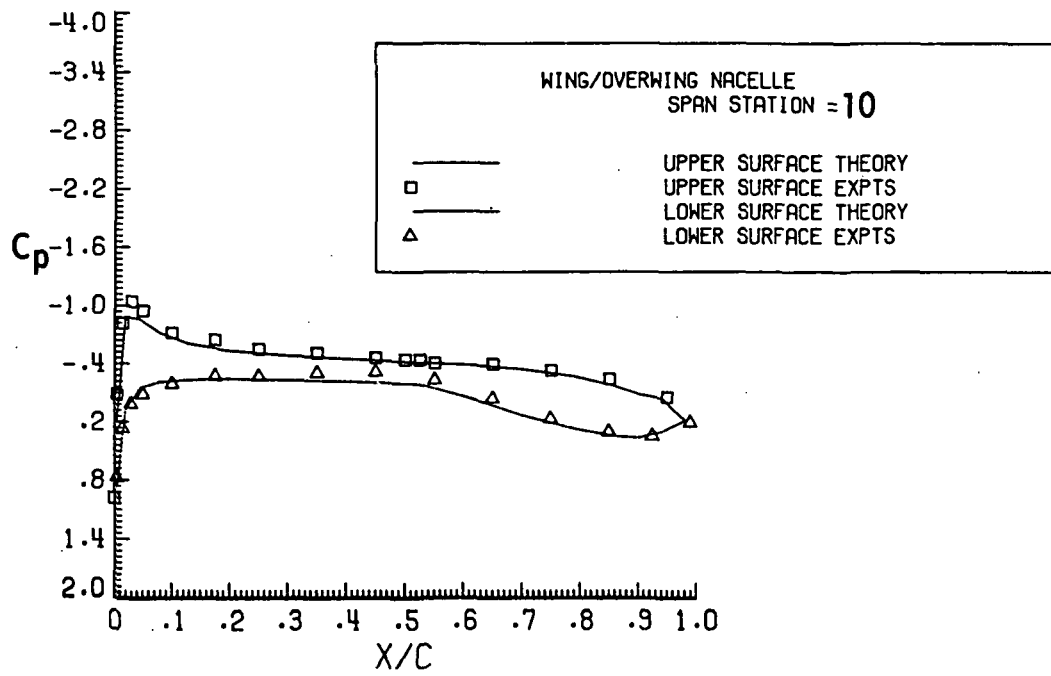
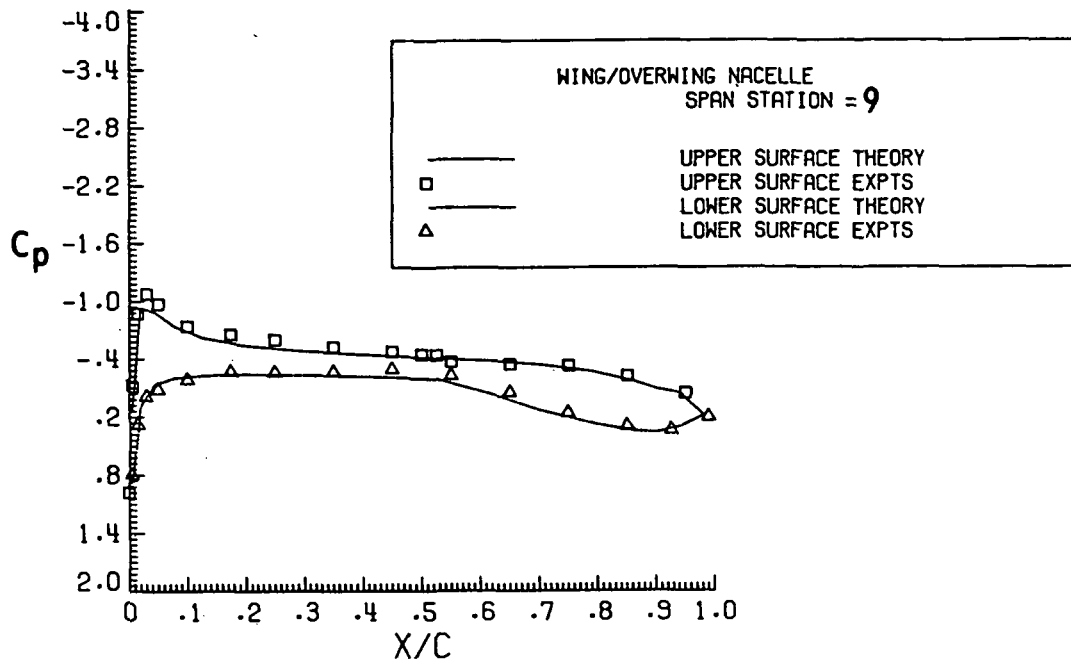


Figure 14. Continued.

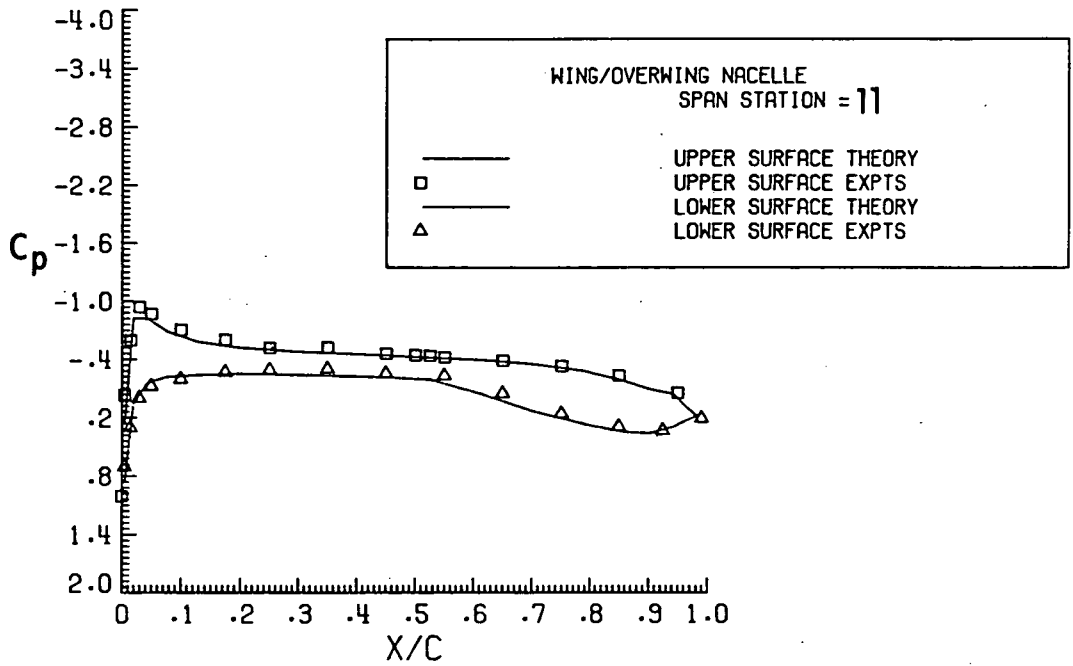


Figure 14. Concluded.

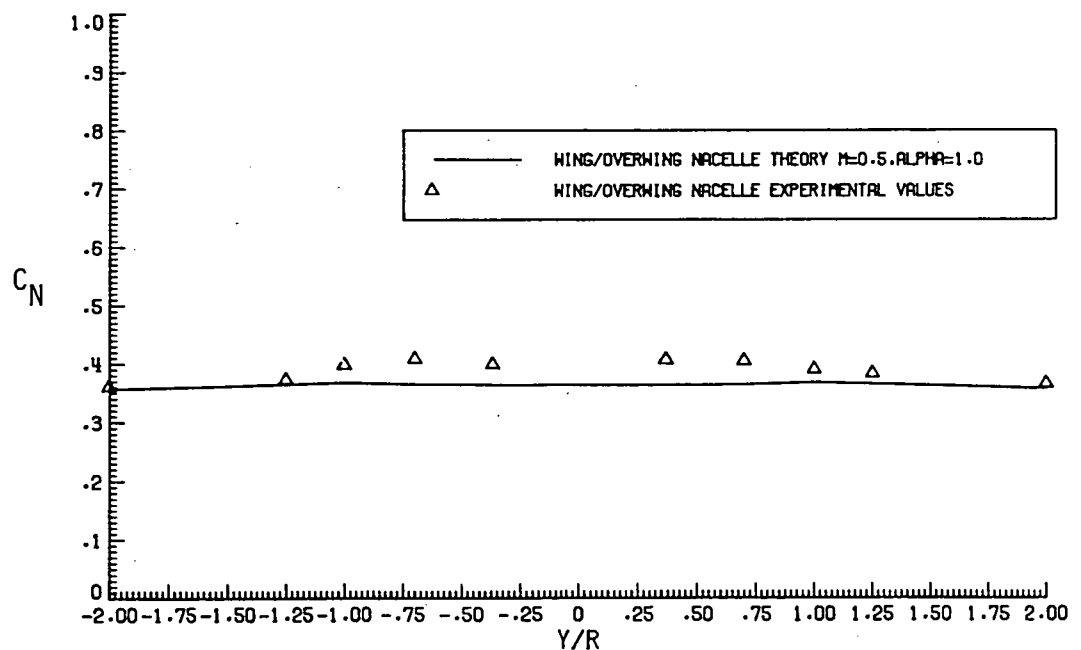


Figure 15. C_N Comparison for the Wing/Overwing Nacelle at $M_\infty = 0.5$, $\alpha = 1.0$ degrees.

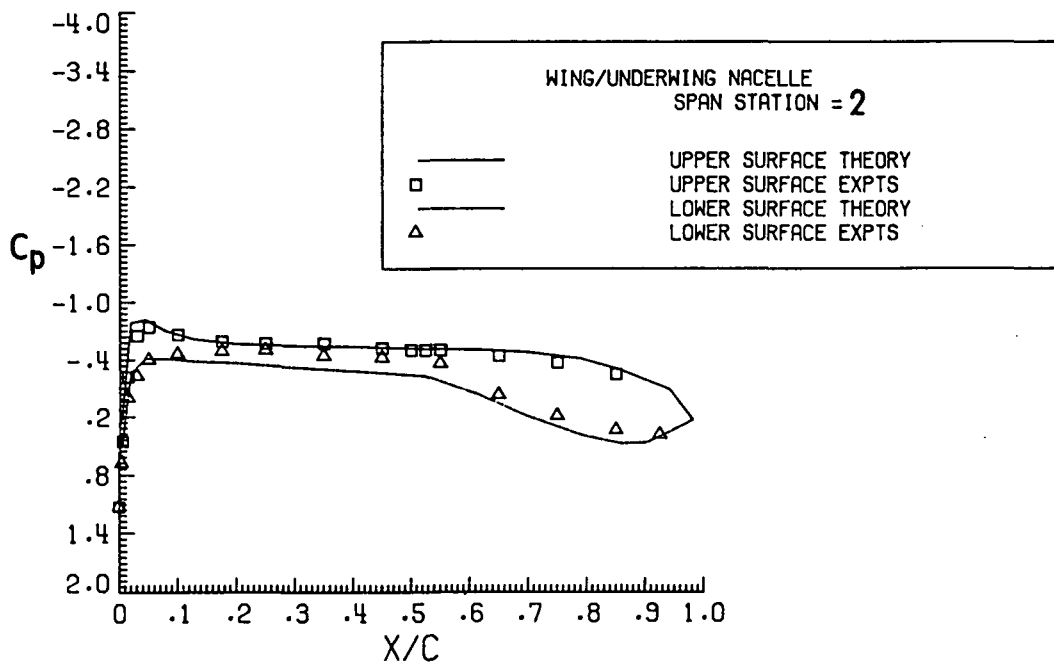
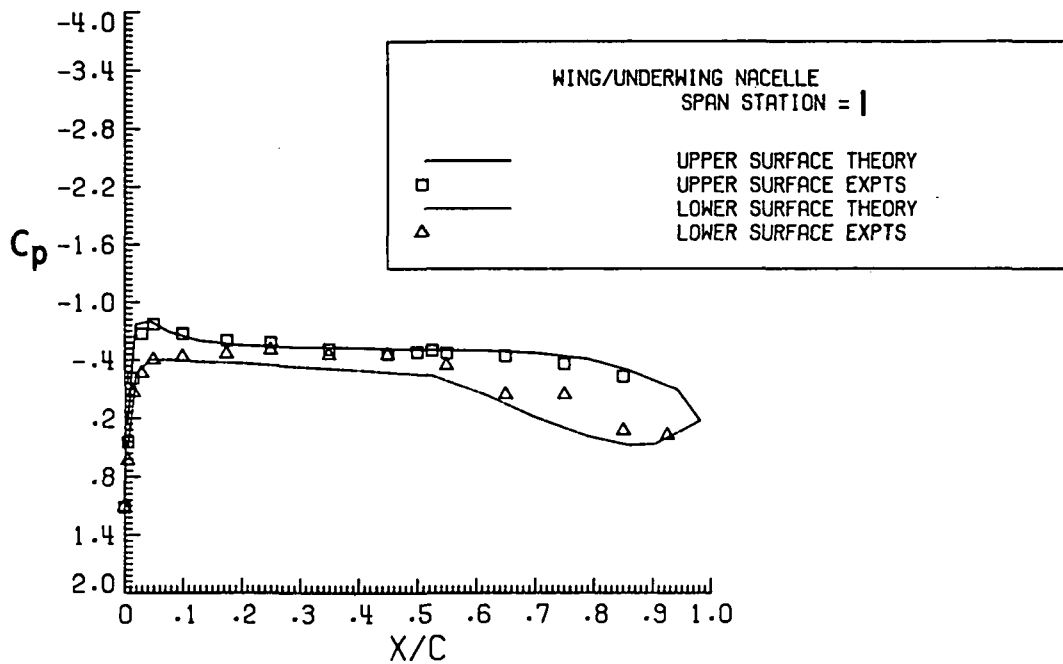


Figure 16. C_p Comparison for the Wing/Underwing Nacelle at $M_\infty = 0.702$, $\alpha = -0.025$ degrees. (Boundary layer not included in theory.)

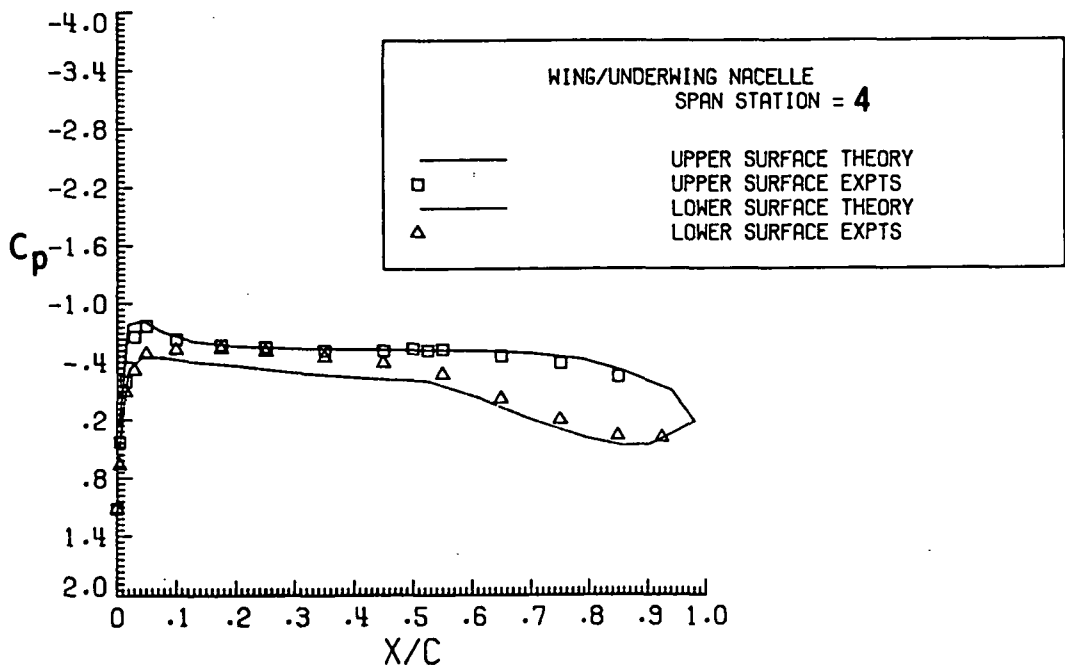
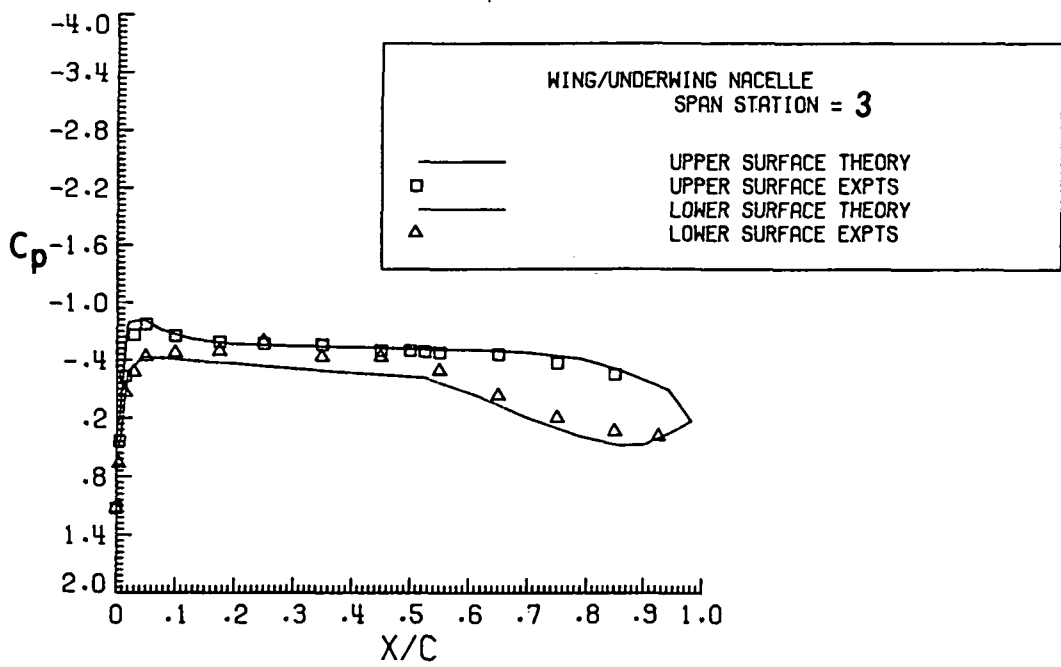


Figure 16. Continued.

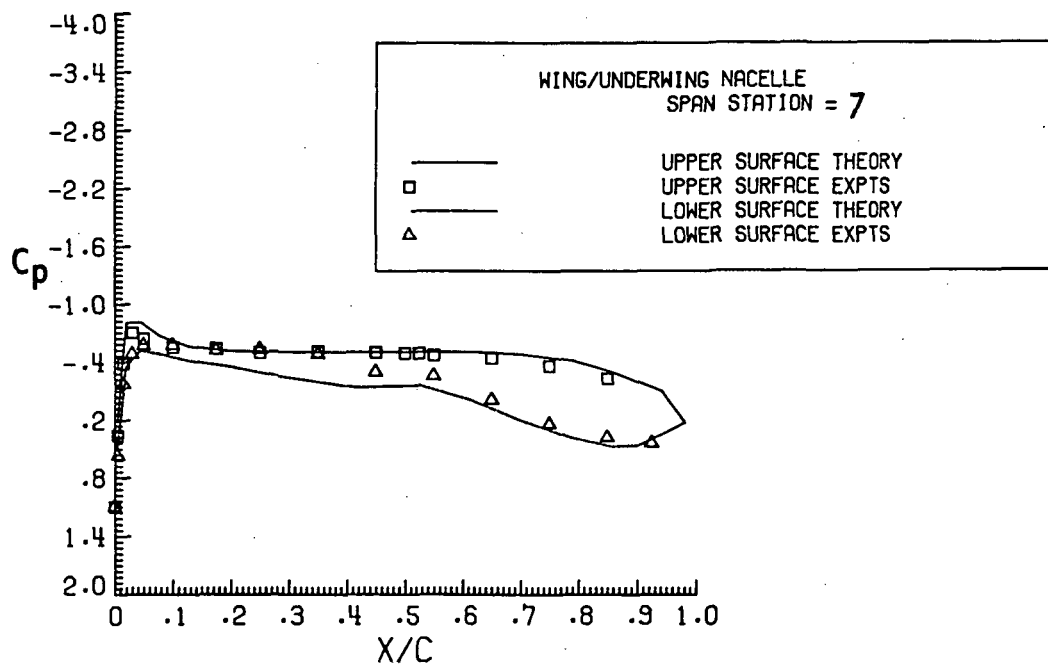
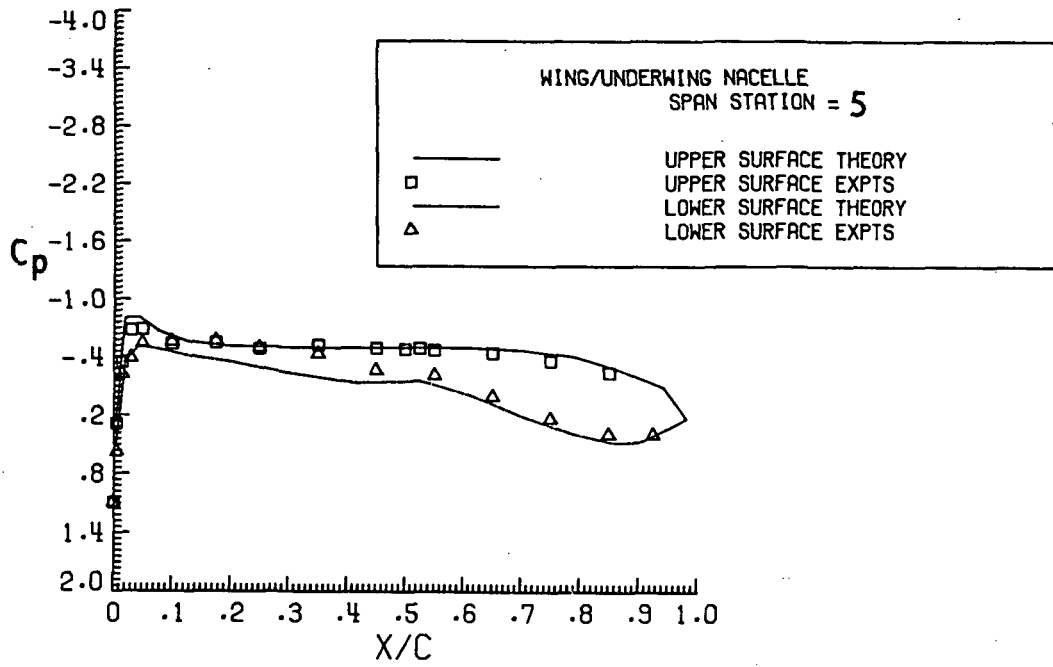


Figure 16. Continued.

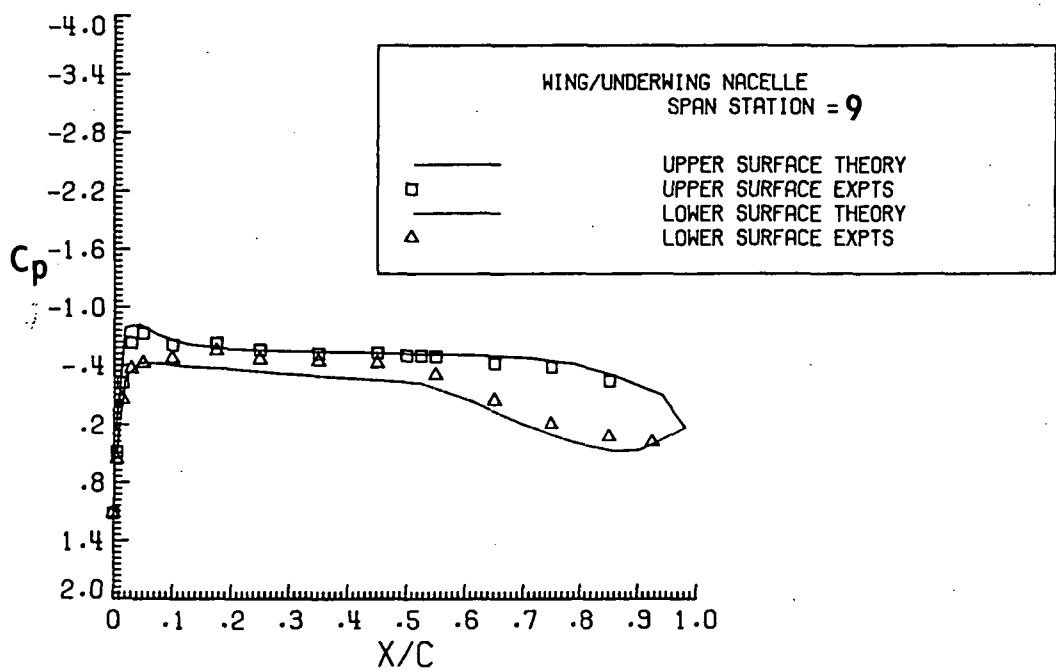
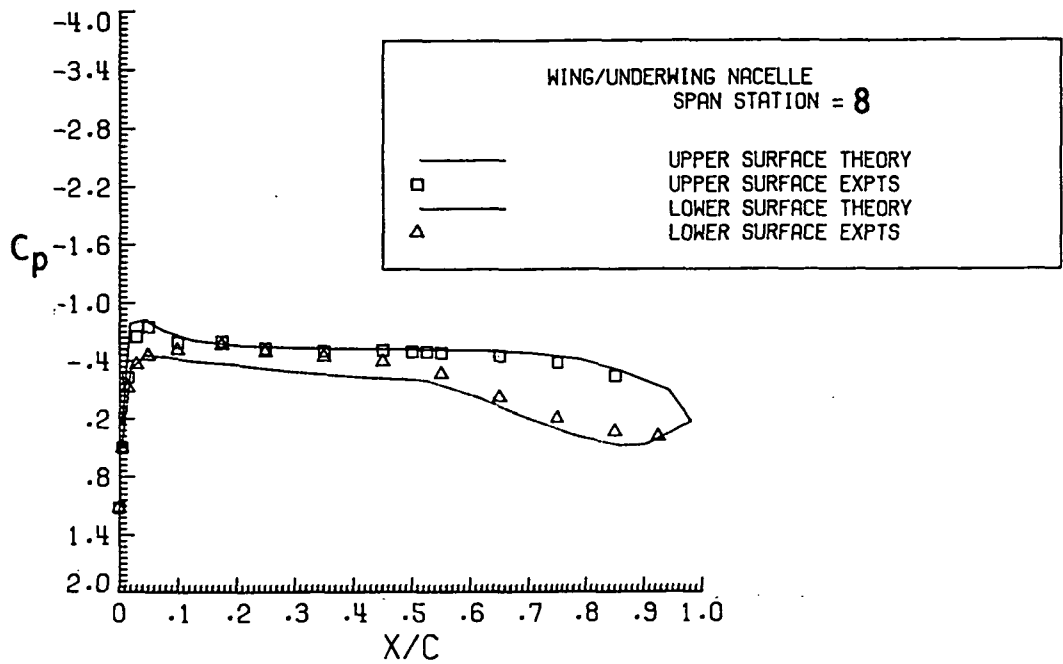


Figure 16. Continued.

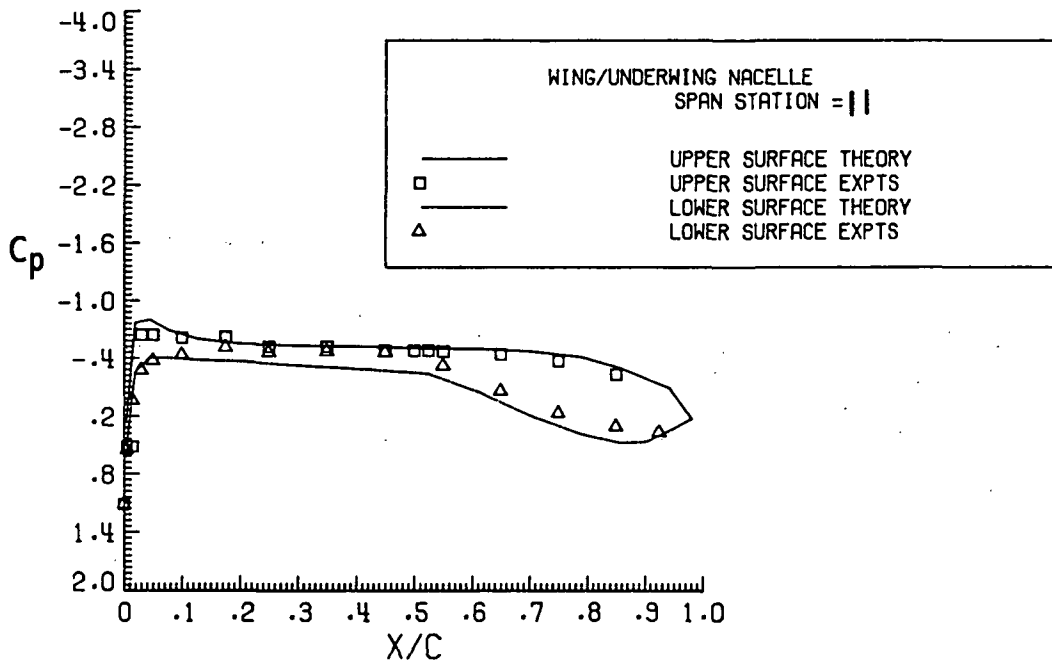
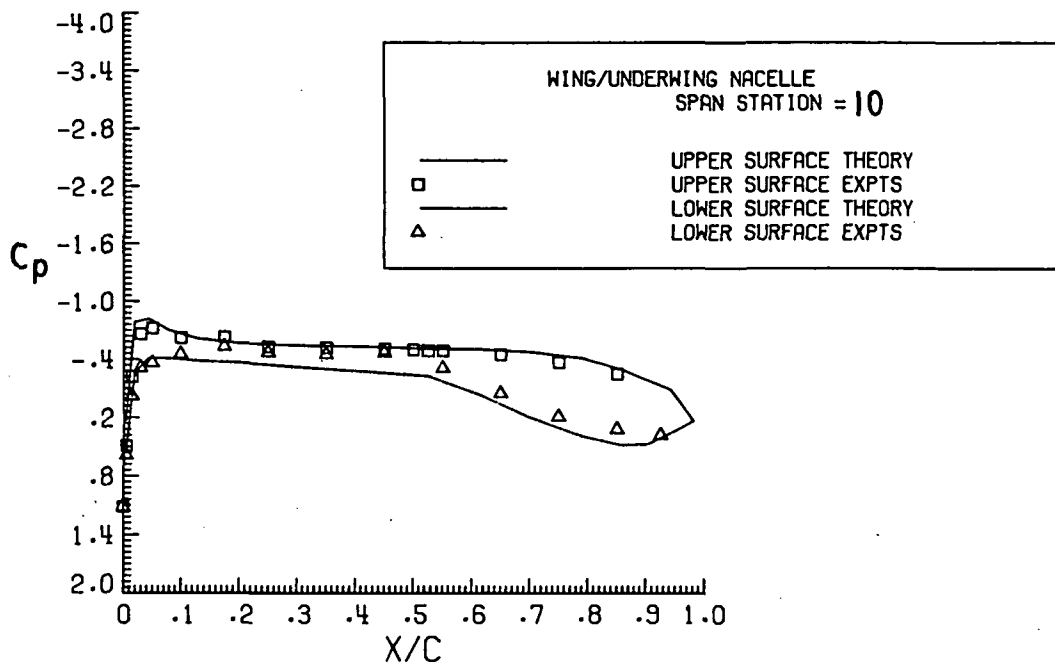


Figure 16. Concluded.

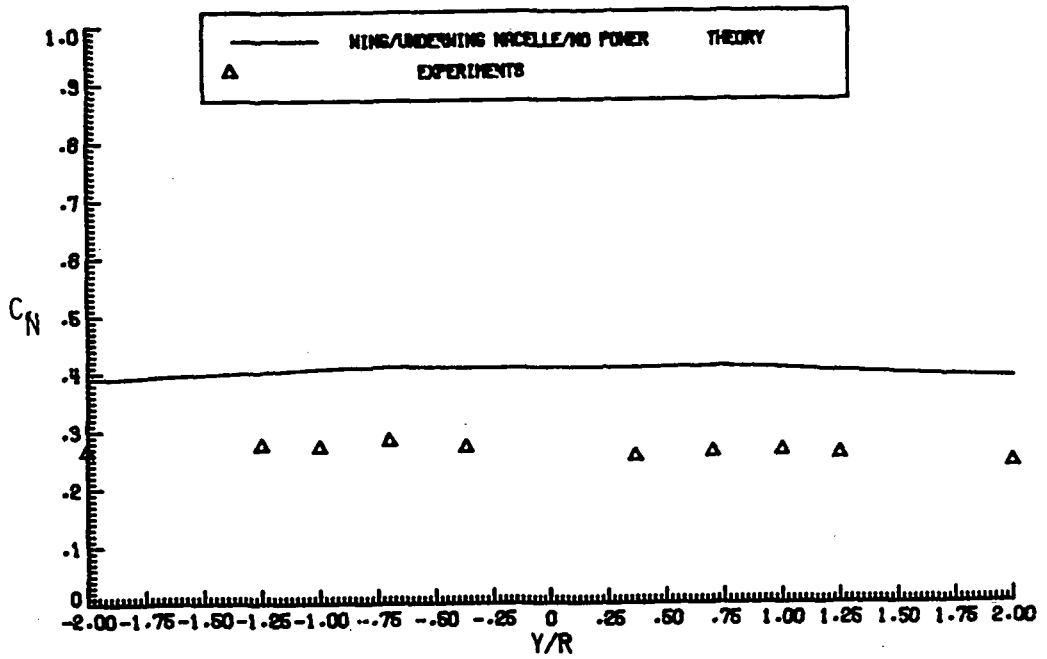


Figure 17. C_N Comparison for the Wing/Underwing Nacelle at $M_\infty = 0.702$, $\alpha = -0.025$ degrees. (Boundary layer not included in theory.)

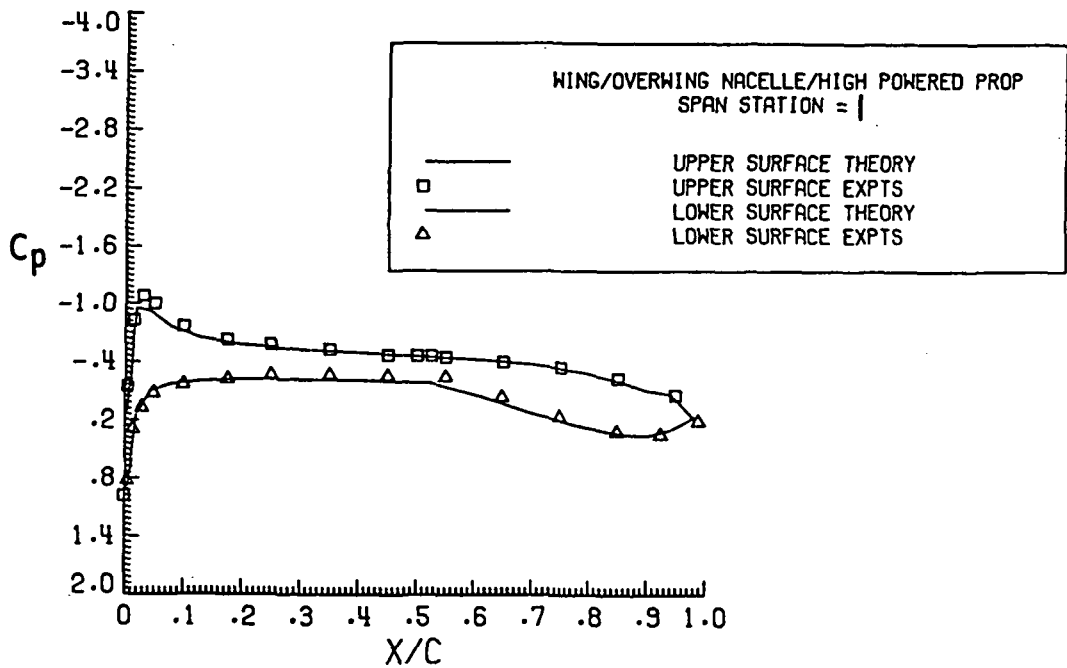


Figure 18. C_p Comparison for Wing/Overwing Nacelle/High Power by the Method I with $C_T = 0.443$, $M_\infty = 0.5$, $\alpha = 1.0$ degrees.

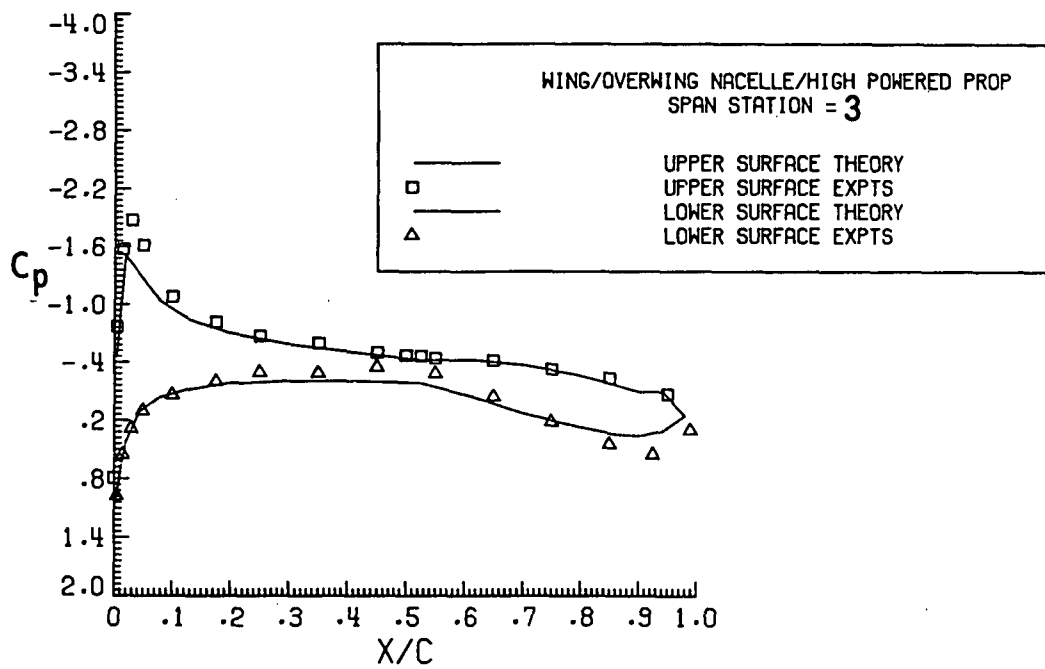
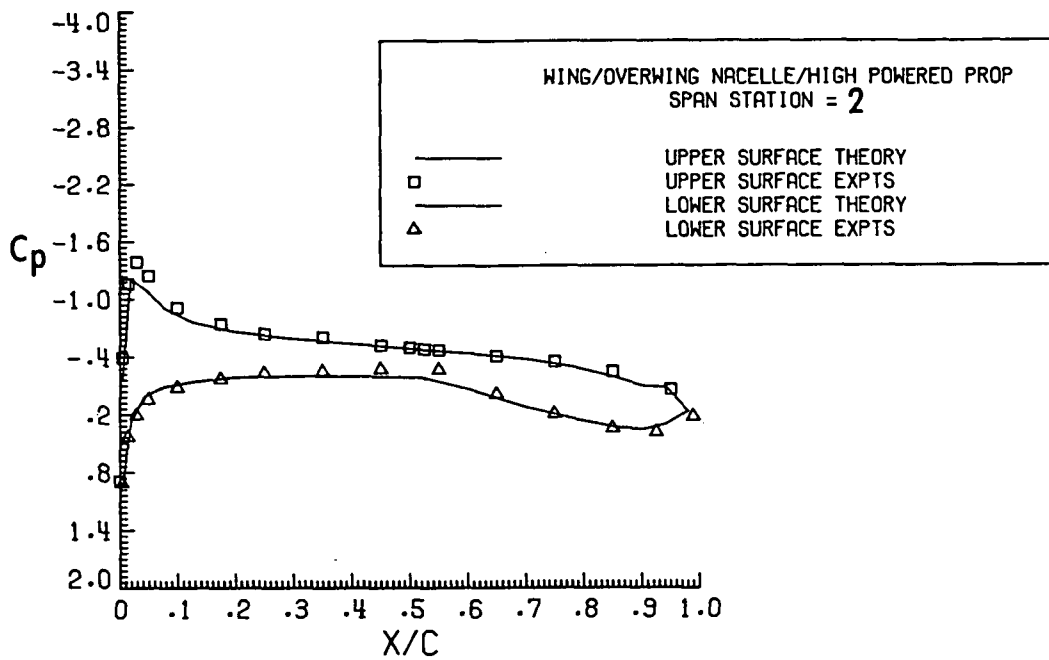


Figure 18. Continued.

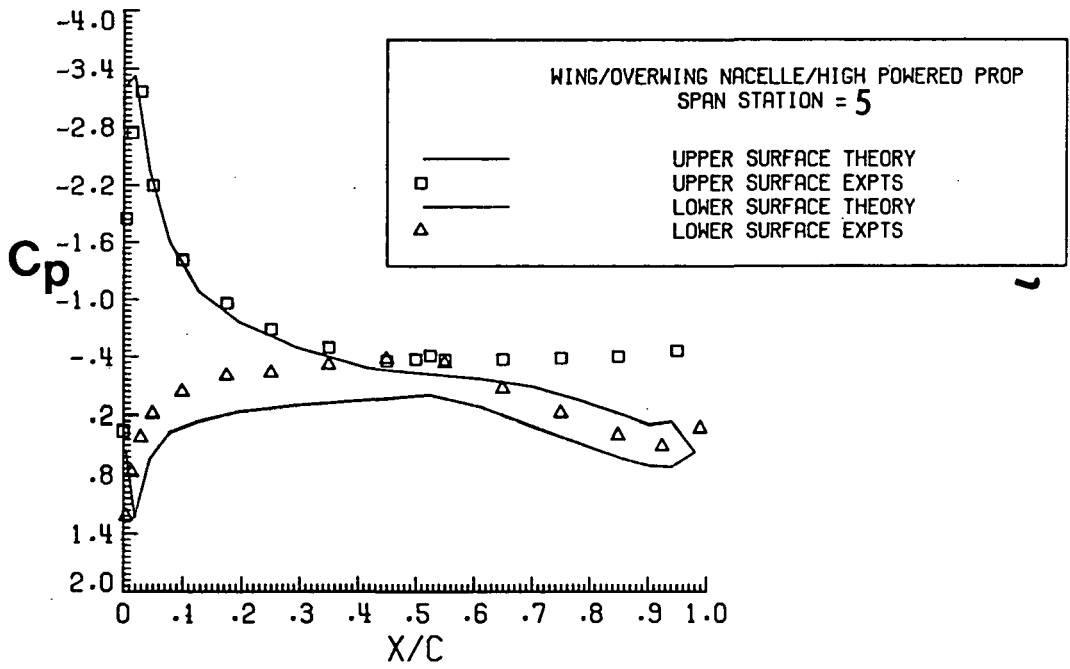
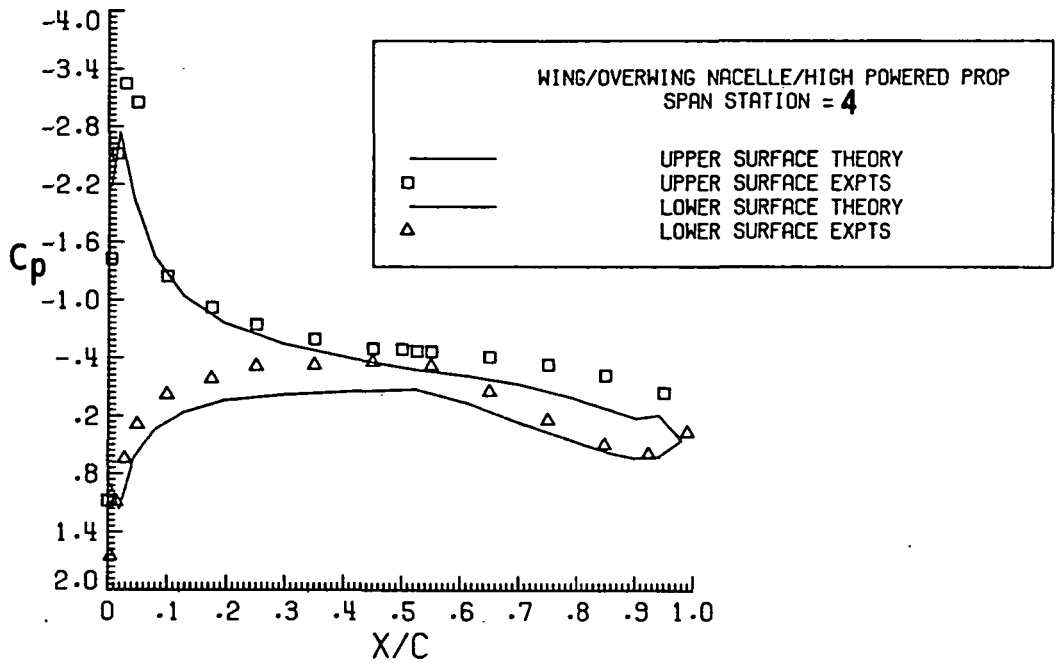


Figure 18. Continued.

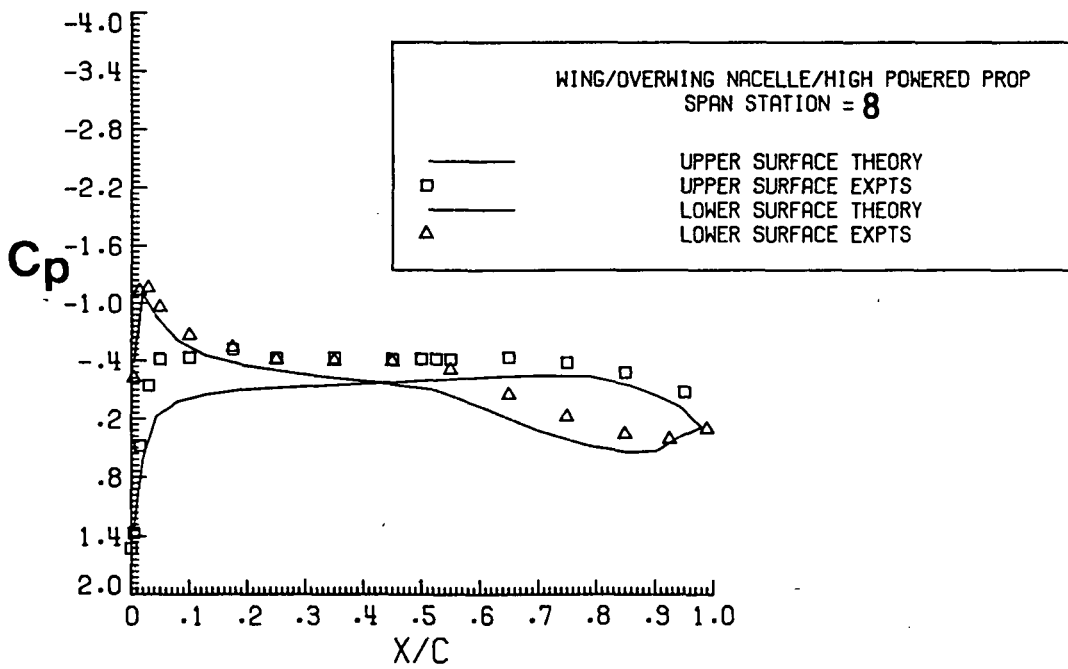
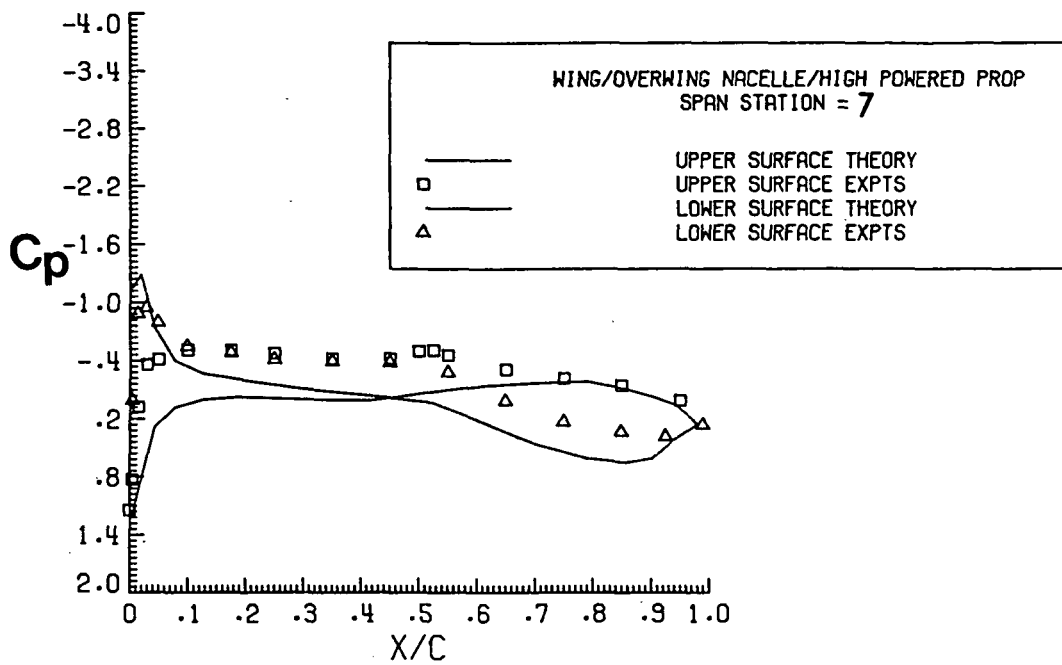


Figure 18. Continued.

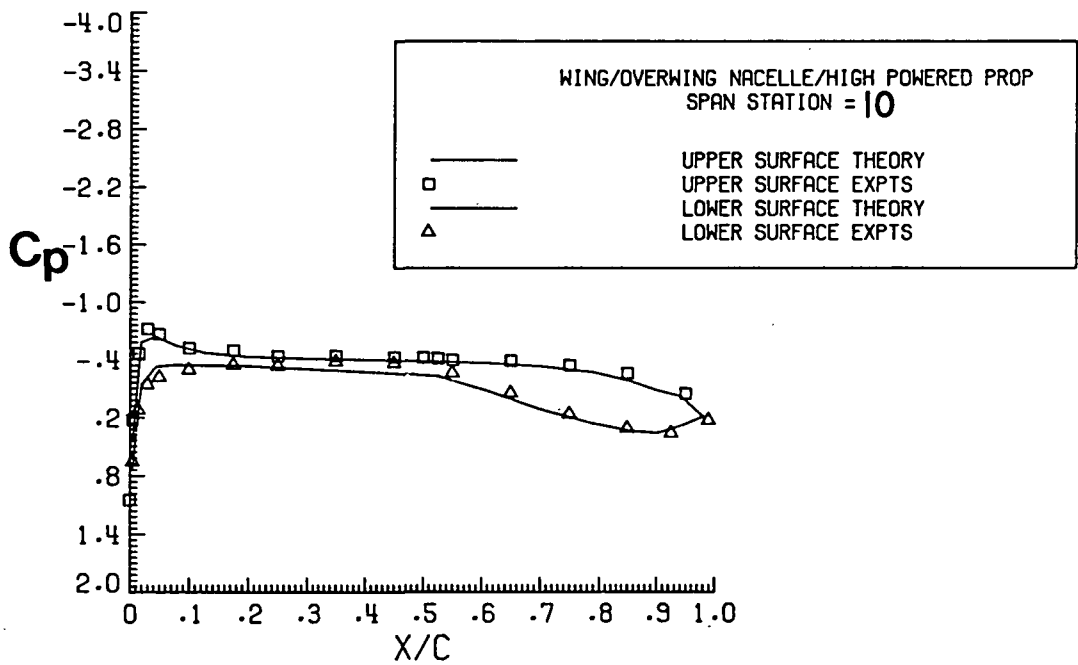
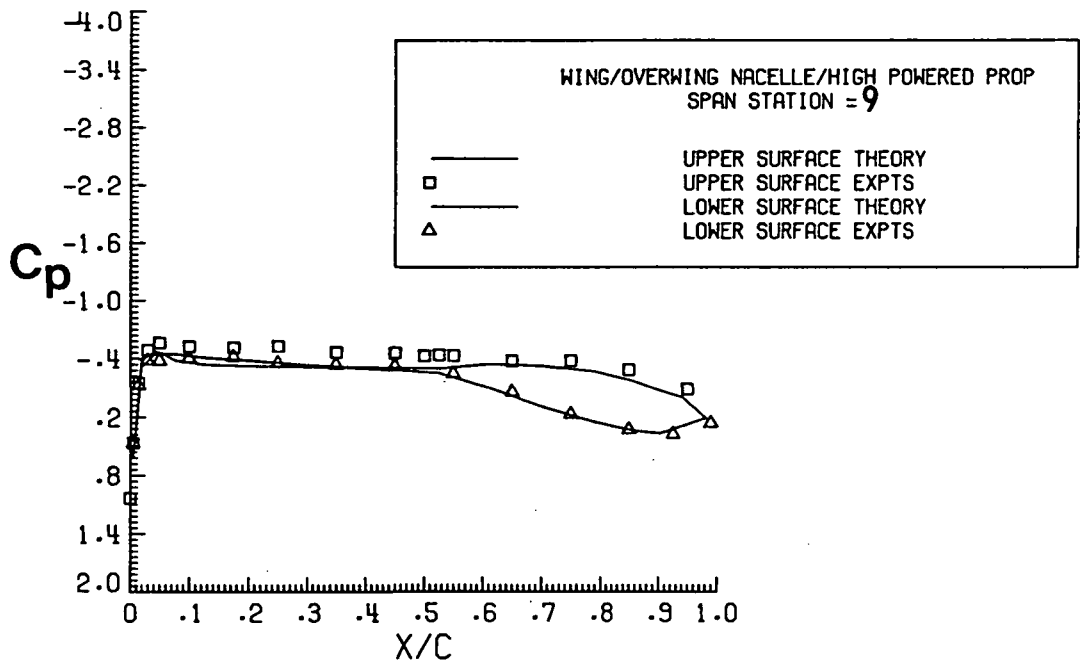


Figure 18. Continued.

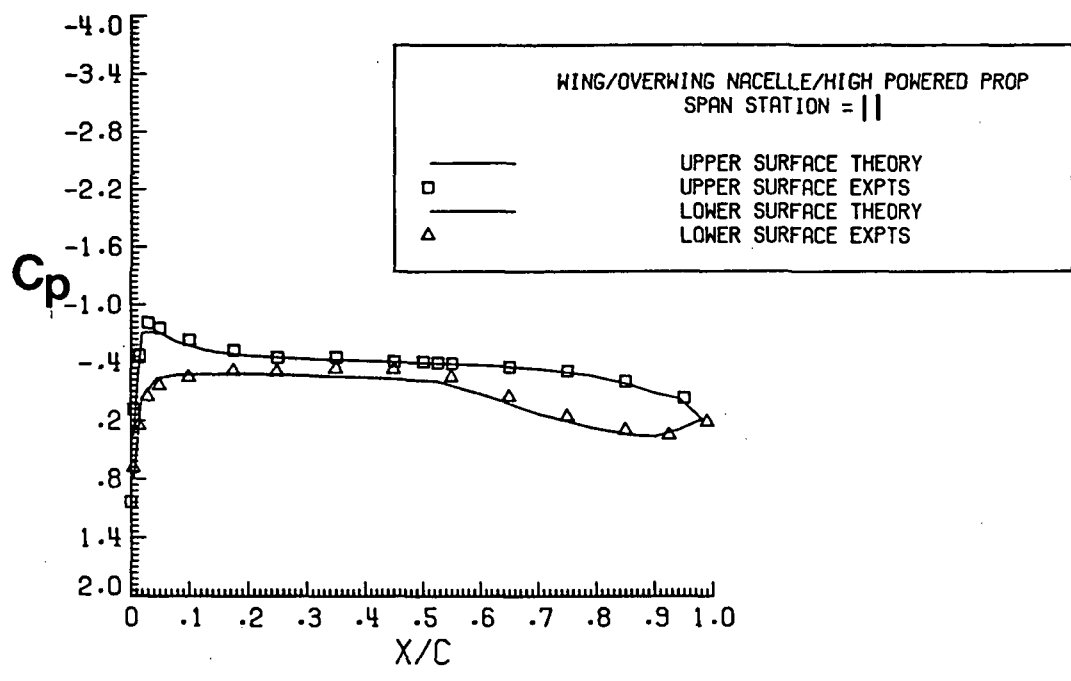


Figure 18. Concluded.

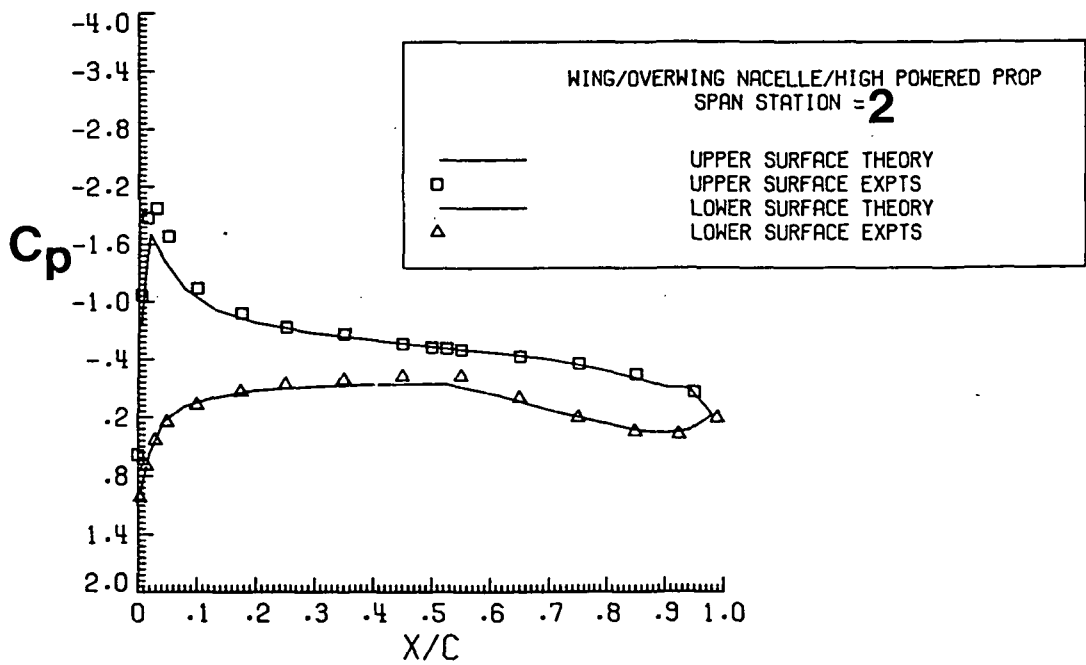
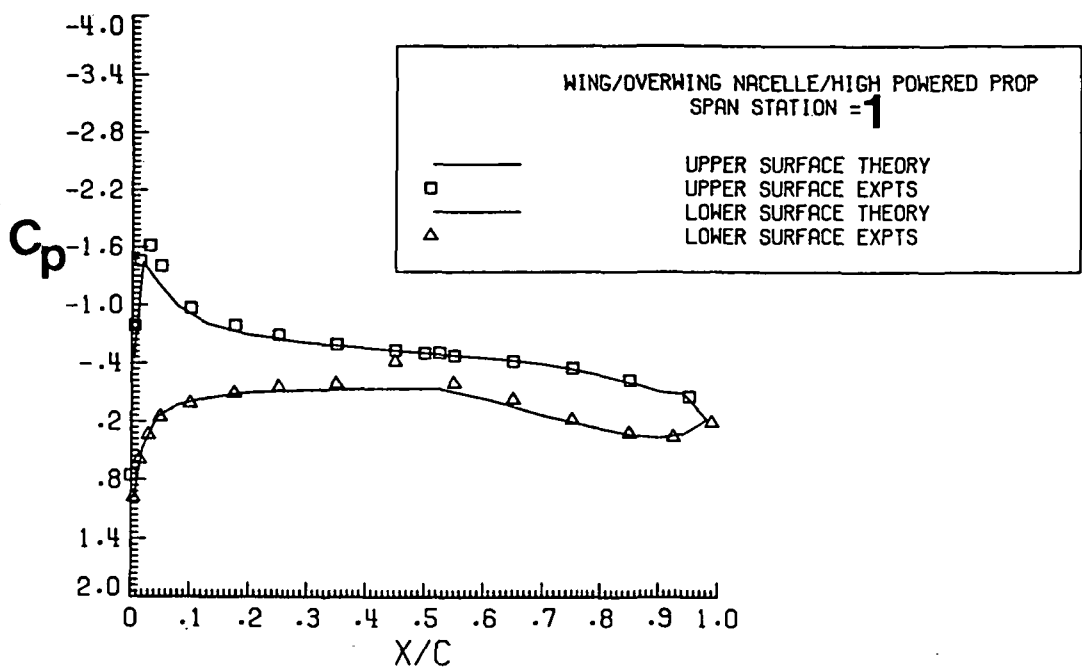


Figure 19. C_p Comparison for Wing/Overwing Nacelle/High Power by the Method I $C_T = 0.408$, $M_\infty = 0.5$, $\alpha = 2.992$ degrees.

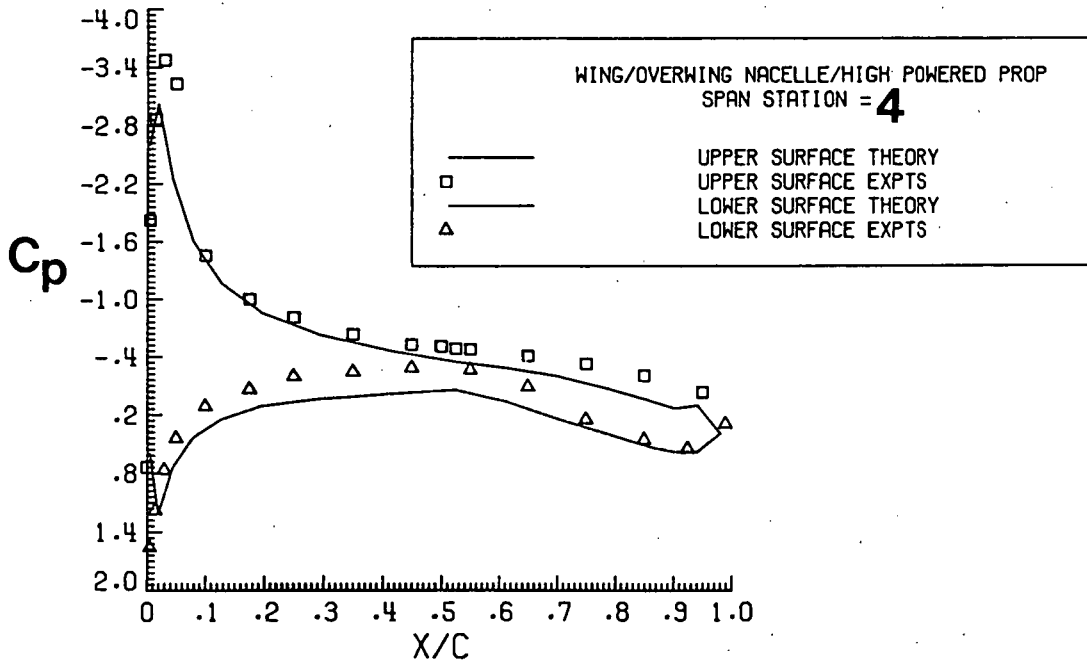
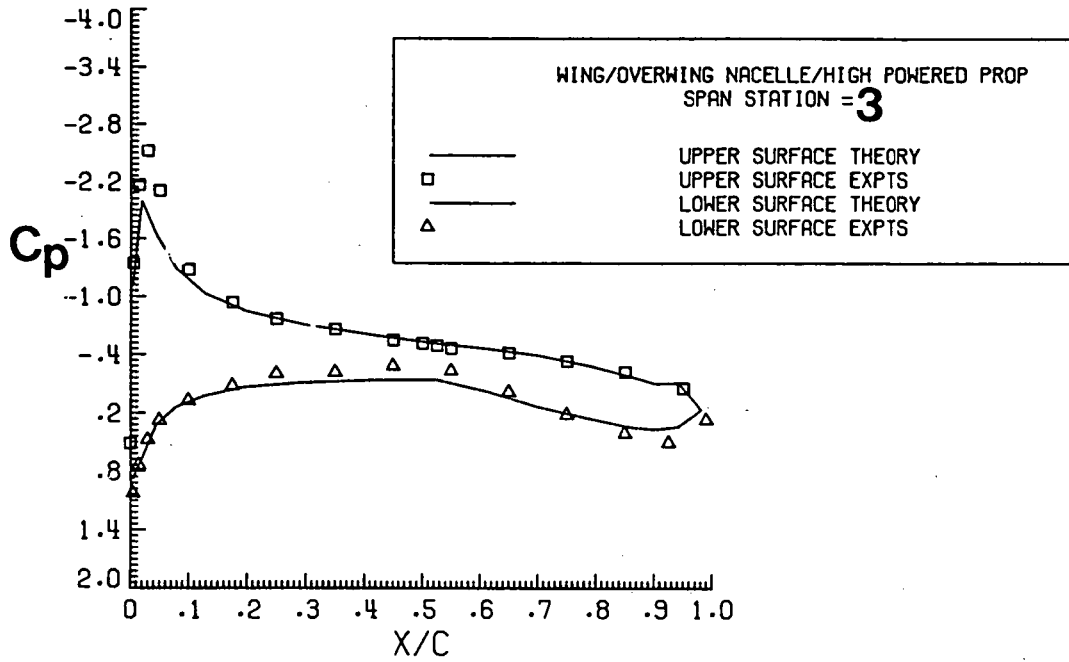


Figure 19. Continued.

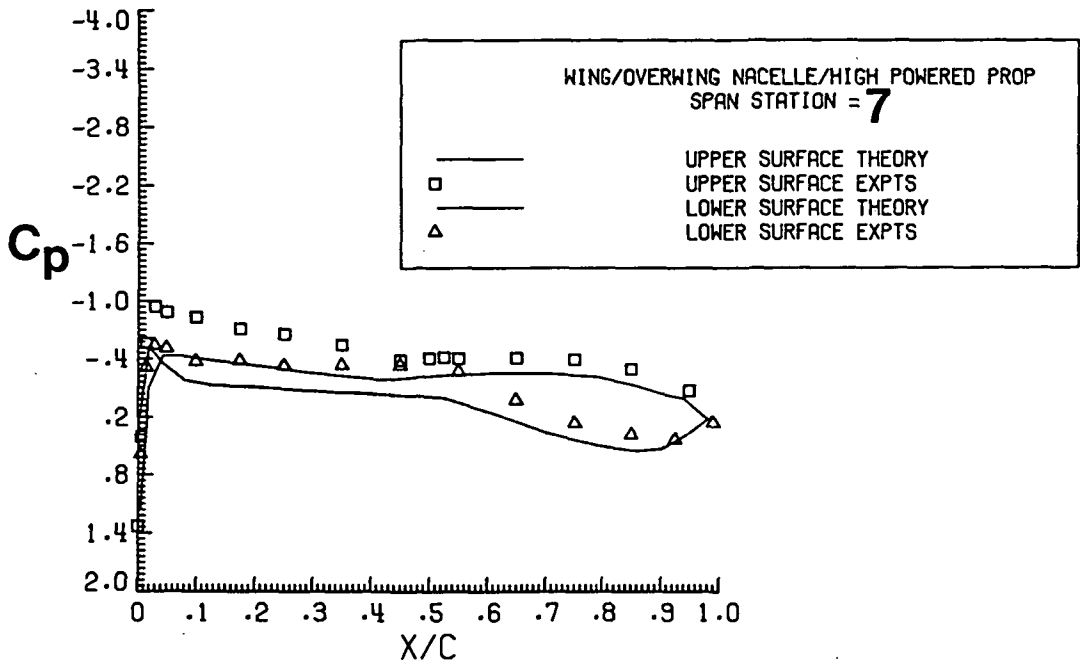
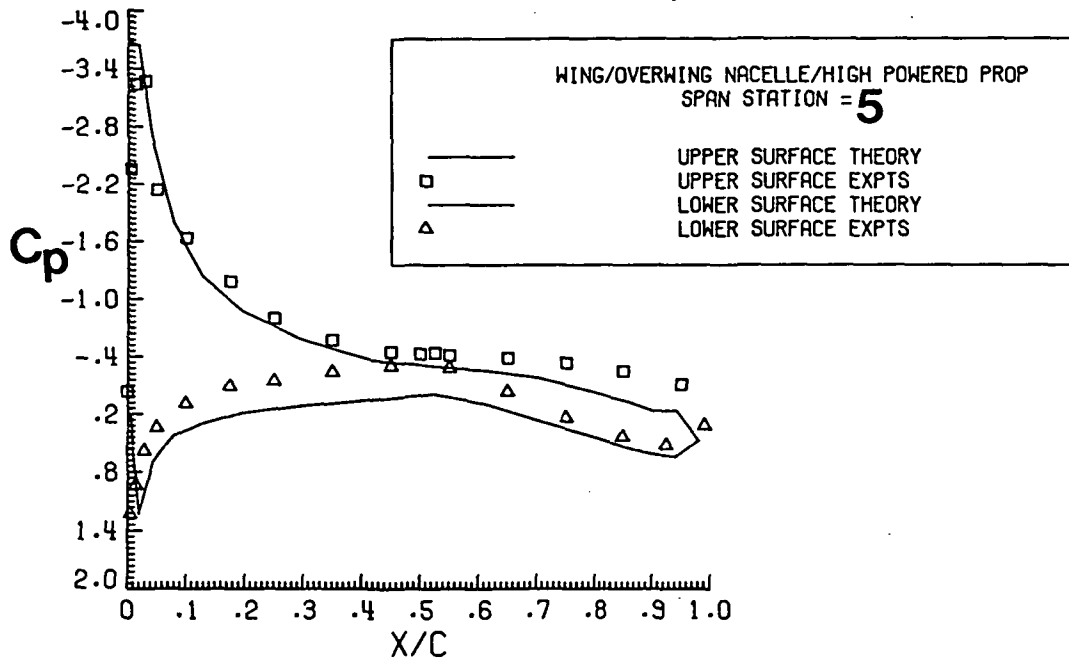


Figure 19. Continued.

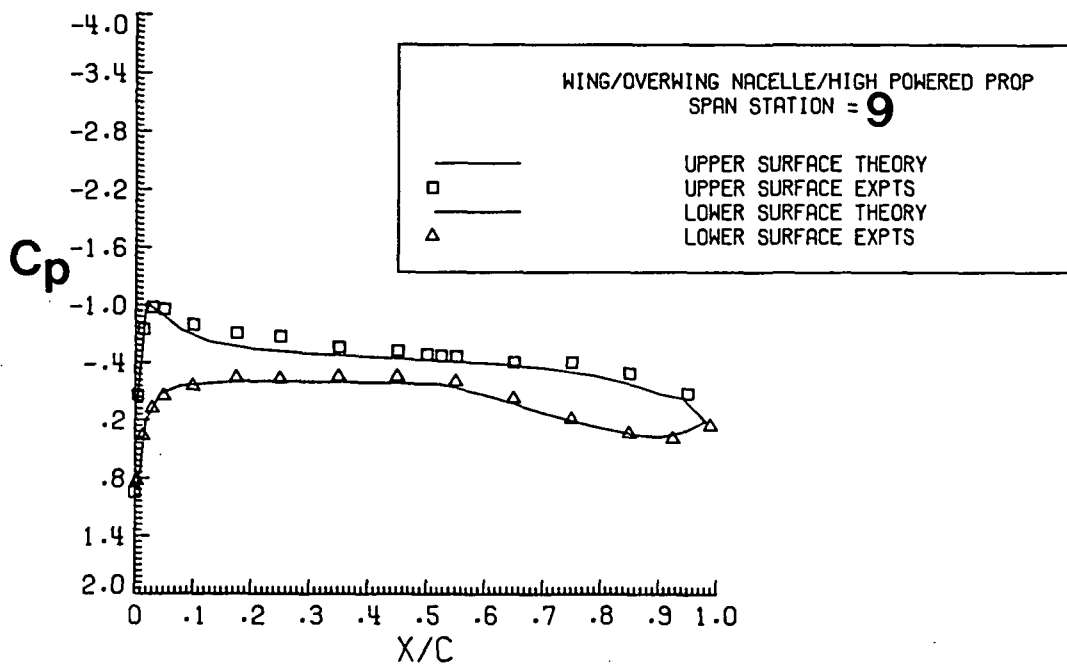
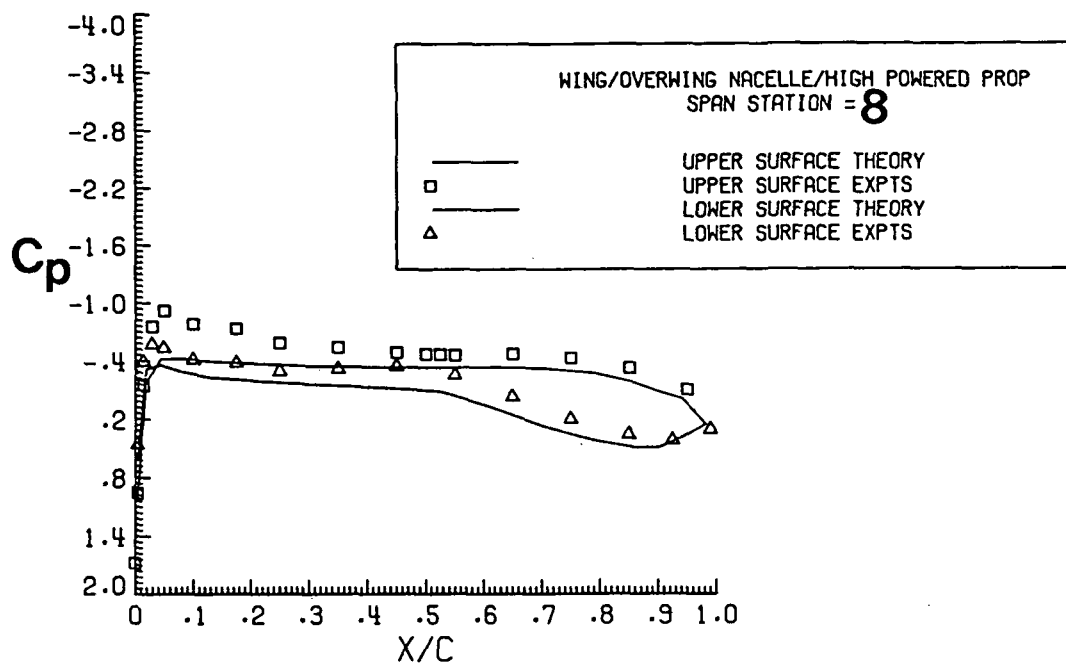


Figure 19. Continued.

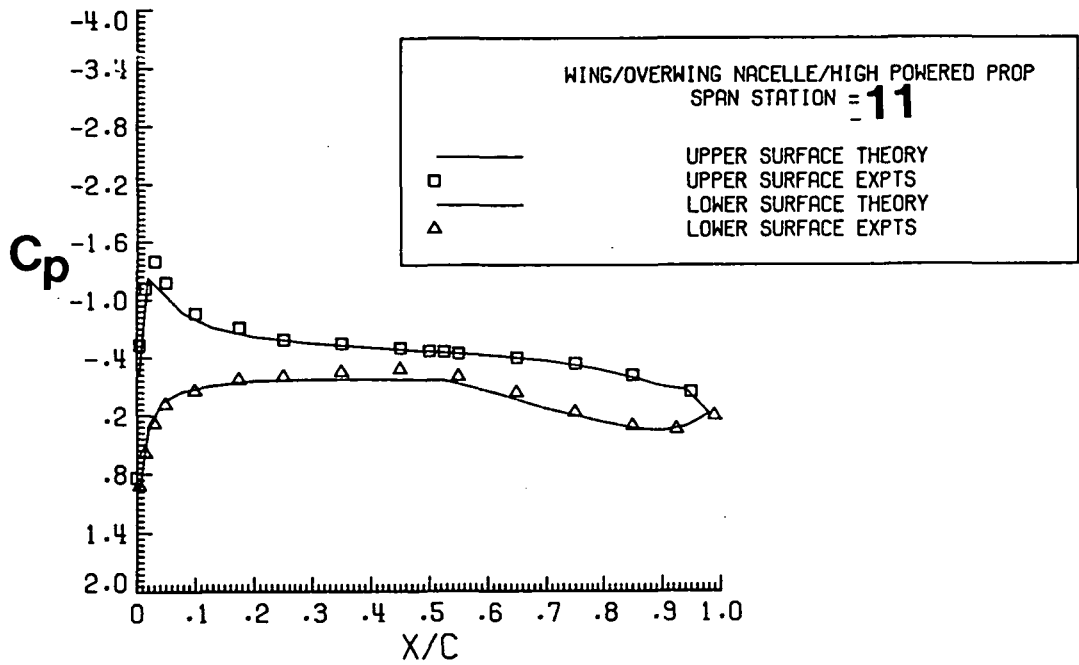
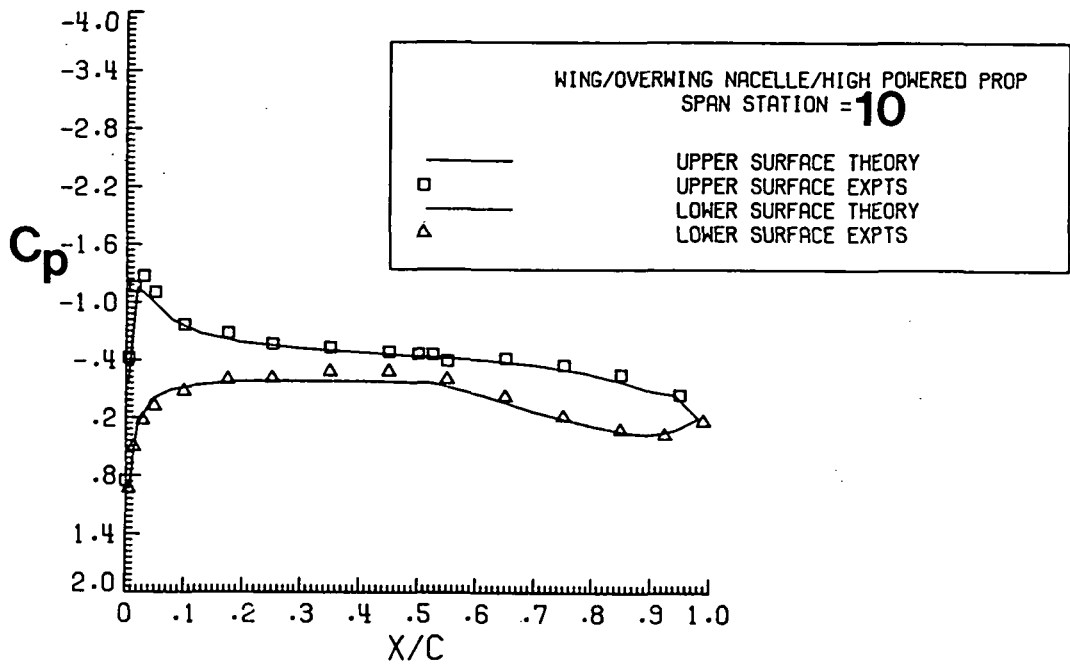


Figure 19. Concluded.

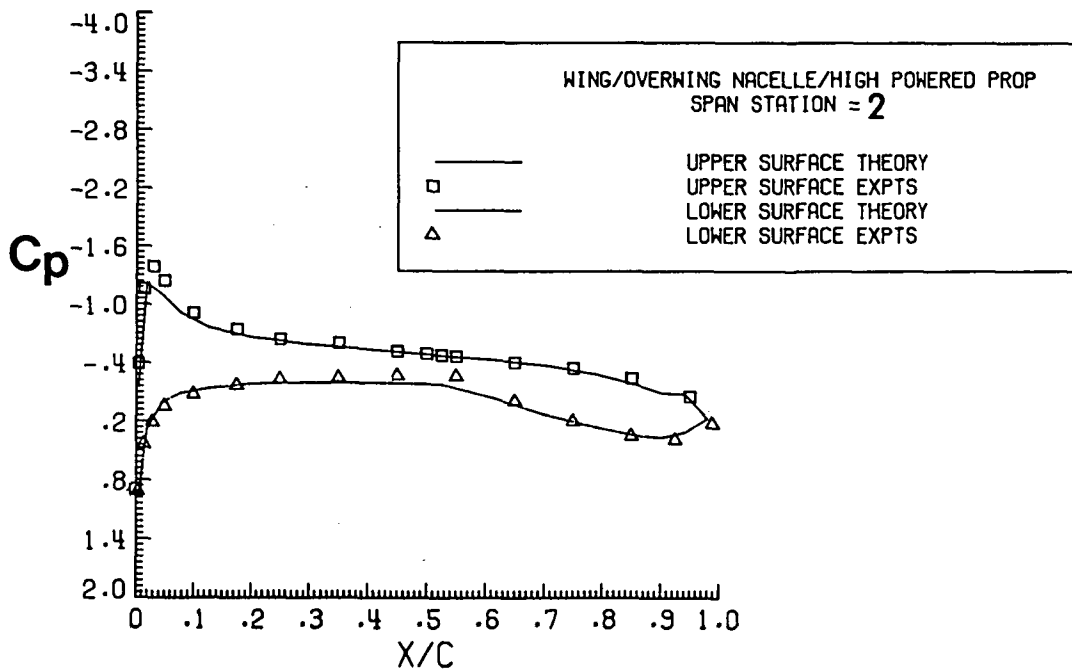
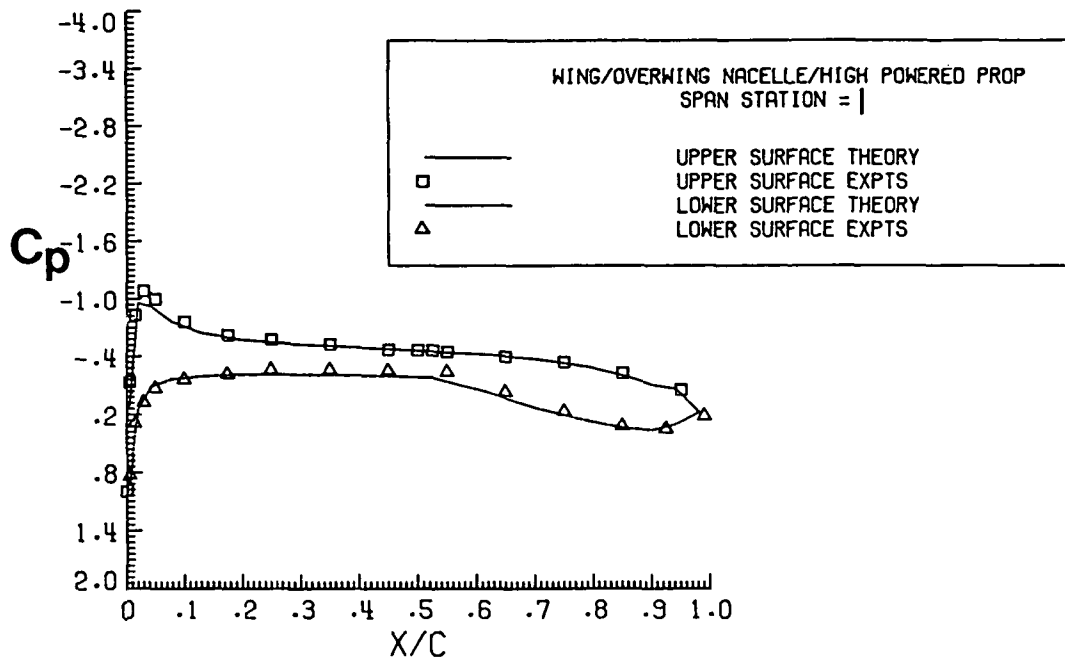


Figure 20. C_p Distribution Comparison for High Thrusting Load with $C_T = 0.443$ by Method II, $M_\infty = 0.5$, $\alpha = 1.0$ degree.

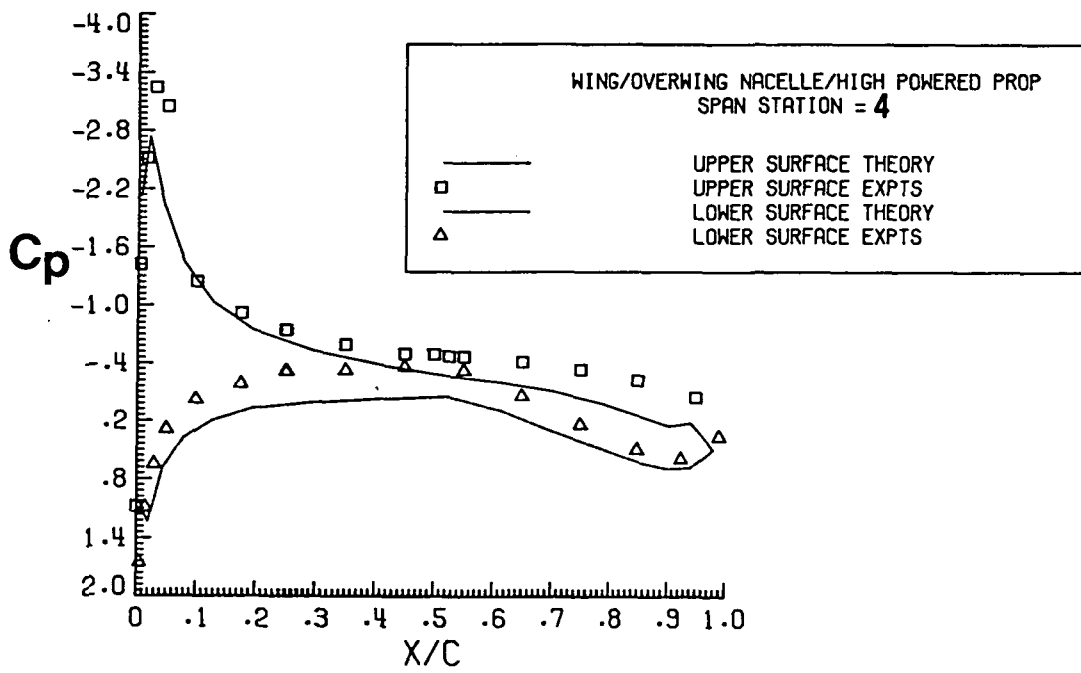
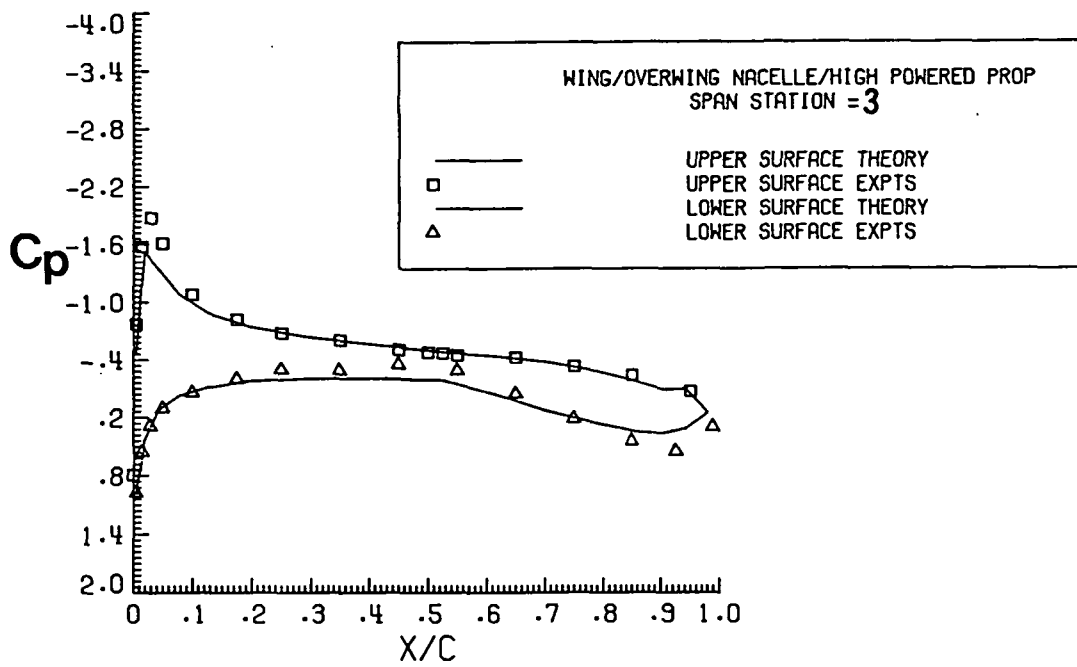


Figure 20. Continued.

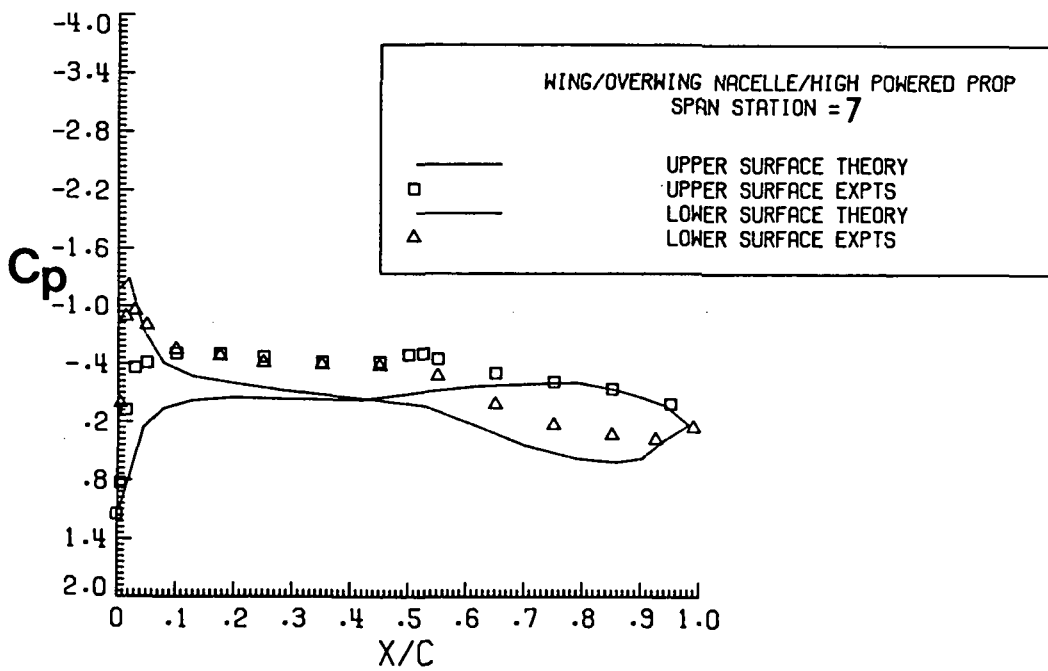
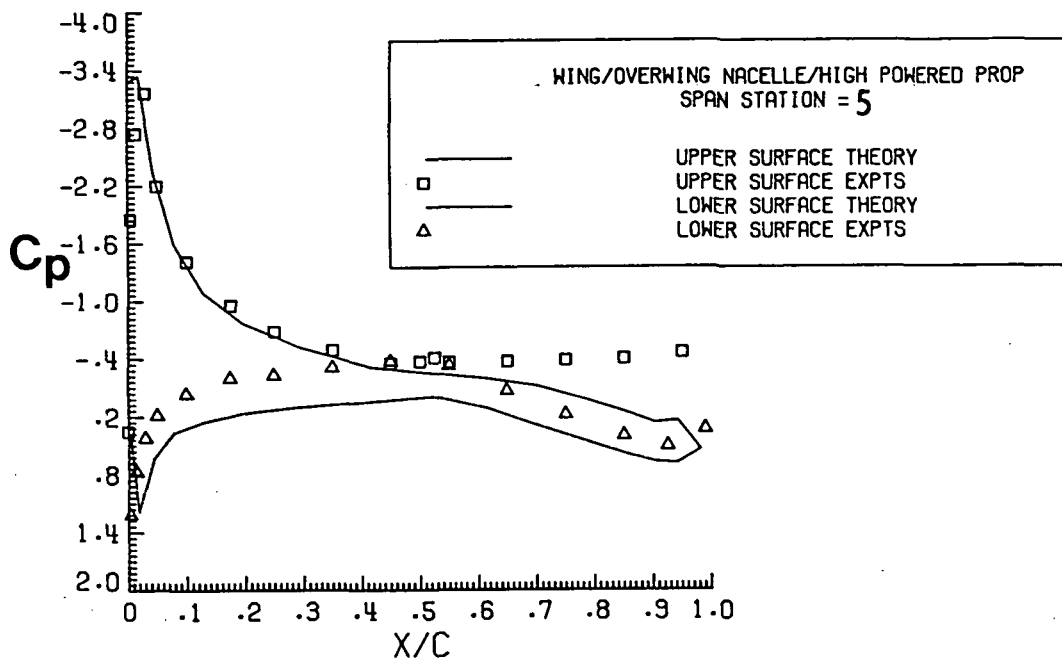


Figure 20. Continued.

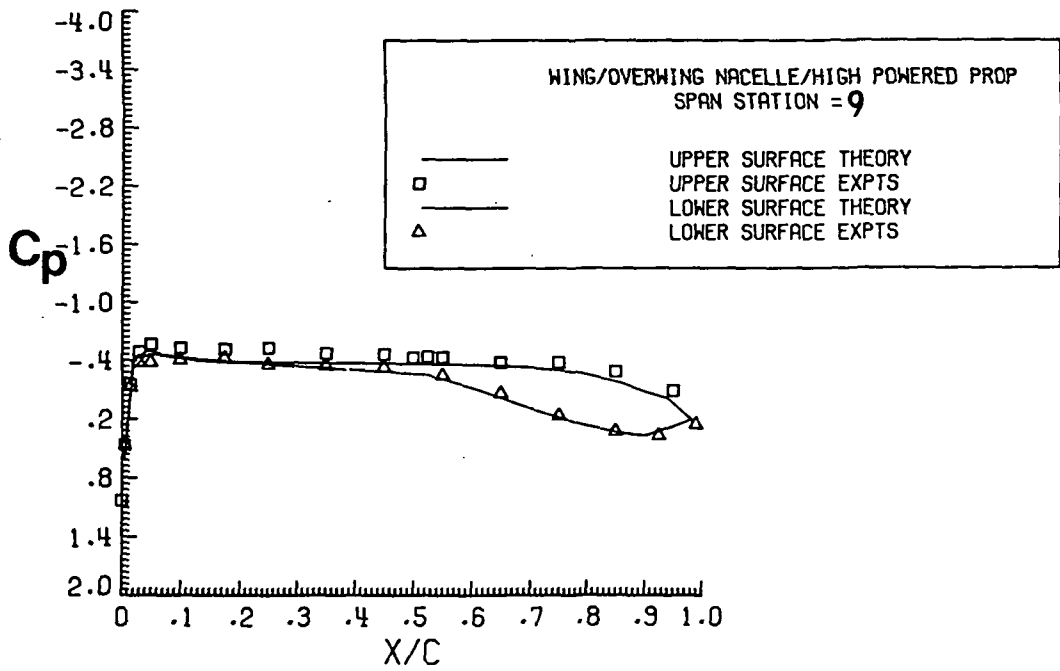
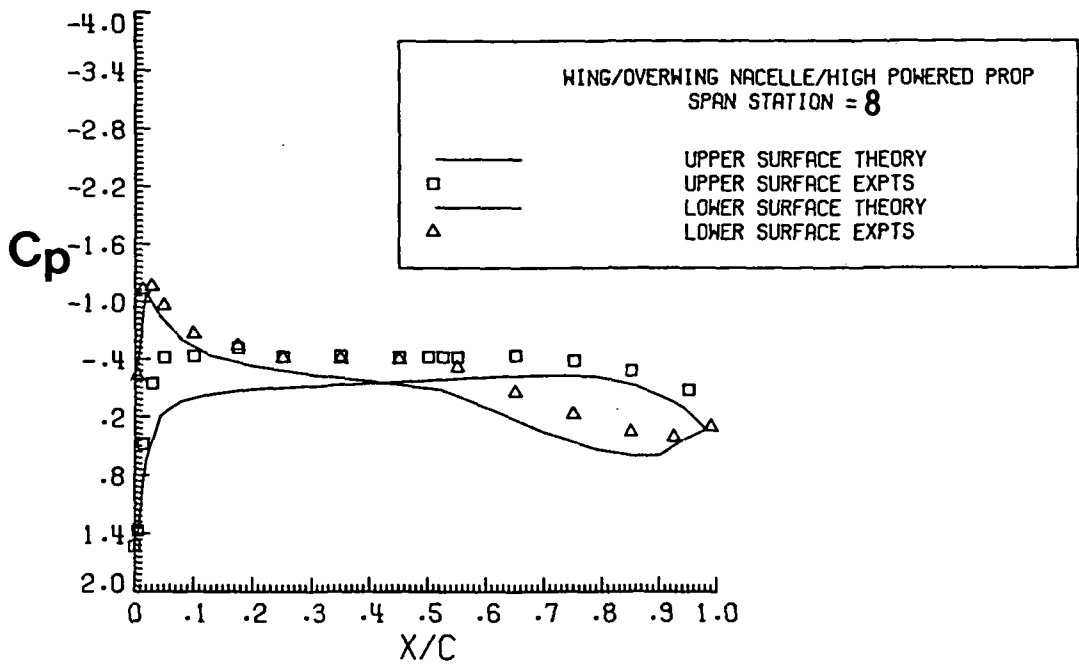


Figure 20. Continued.

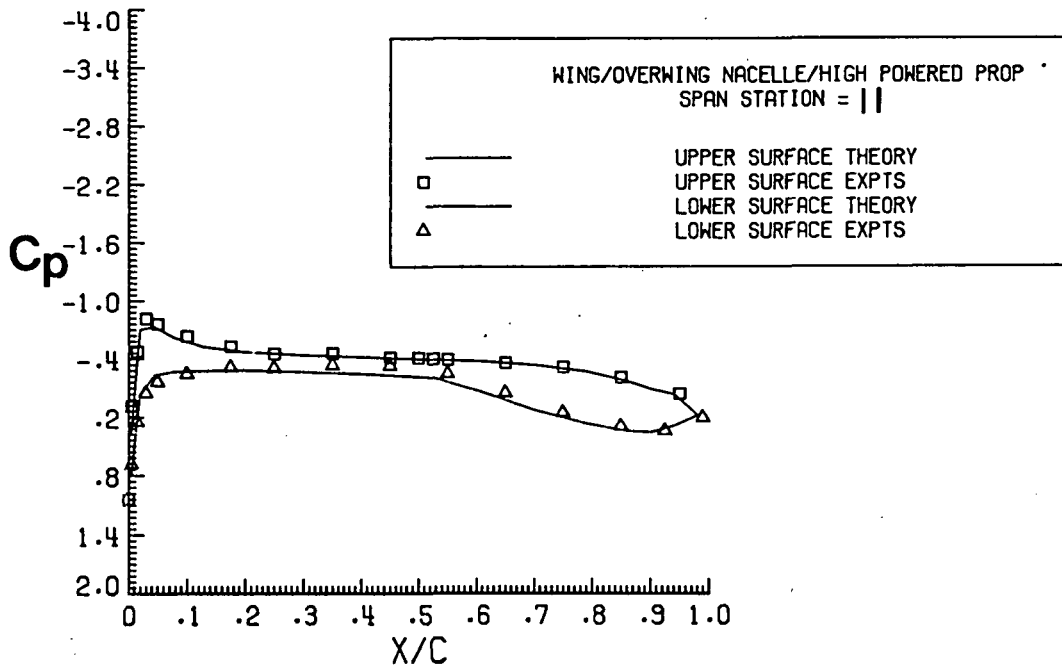
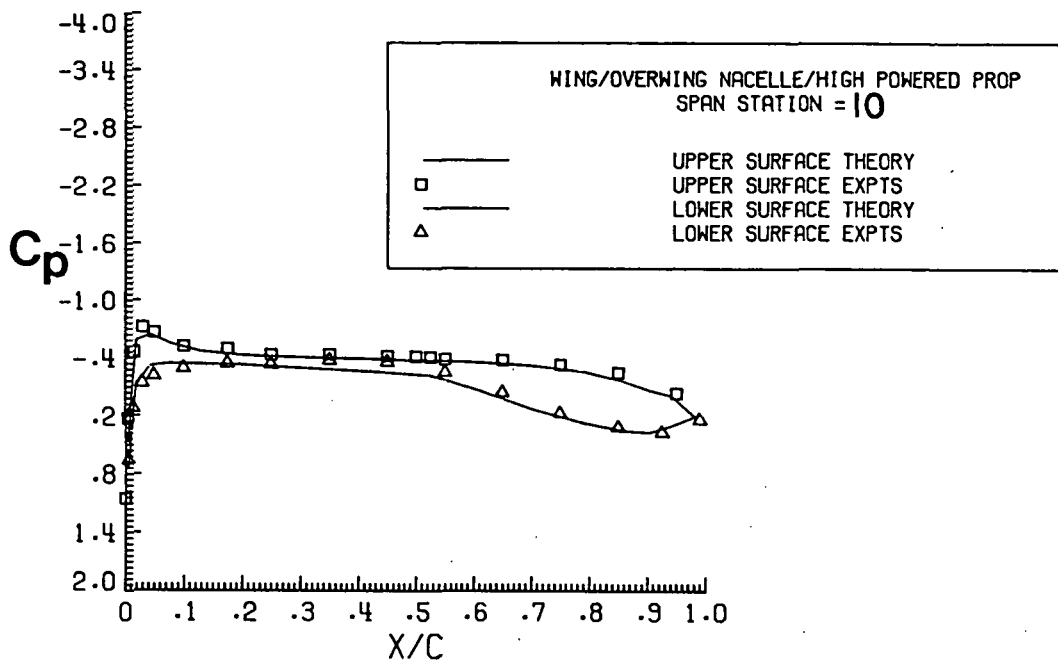


Figure 20. Concluded.

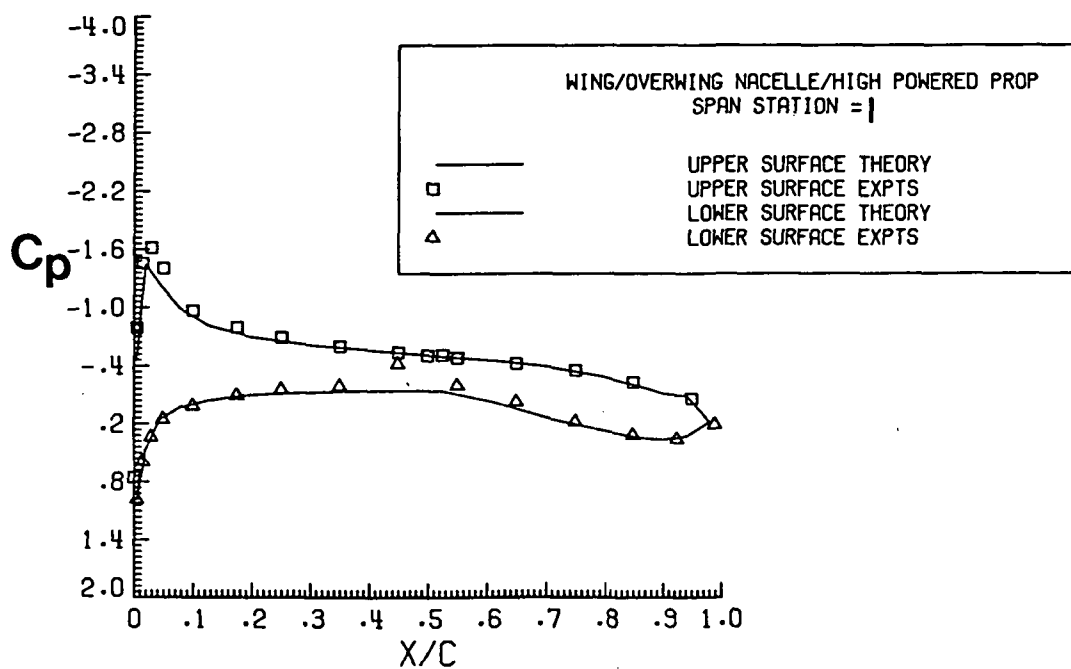


Figure 21. C_p Distribution Comparison for High Thrusting Load
with $C_T = 0.408$ by Method II, $M_\infty = 0.5$,
 $\alpha = 2.992$ degrees.

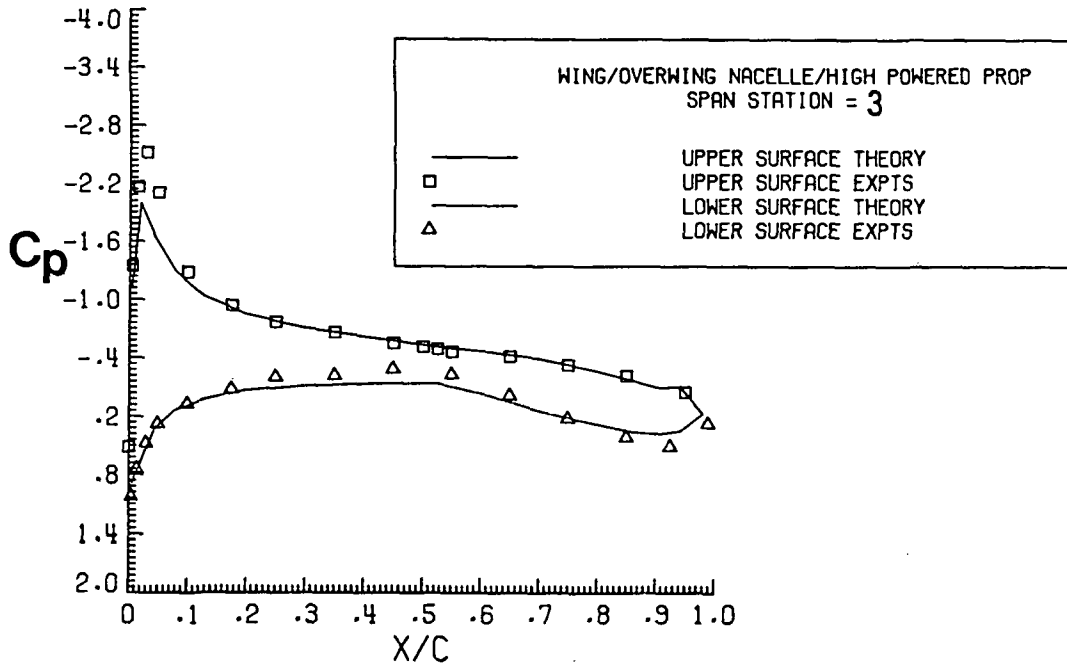
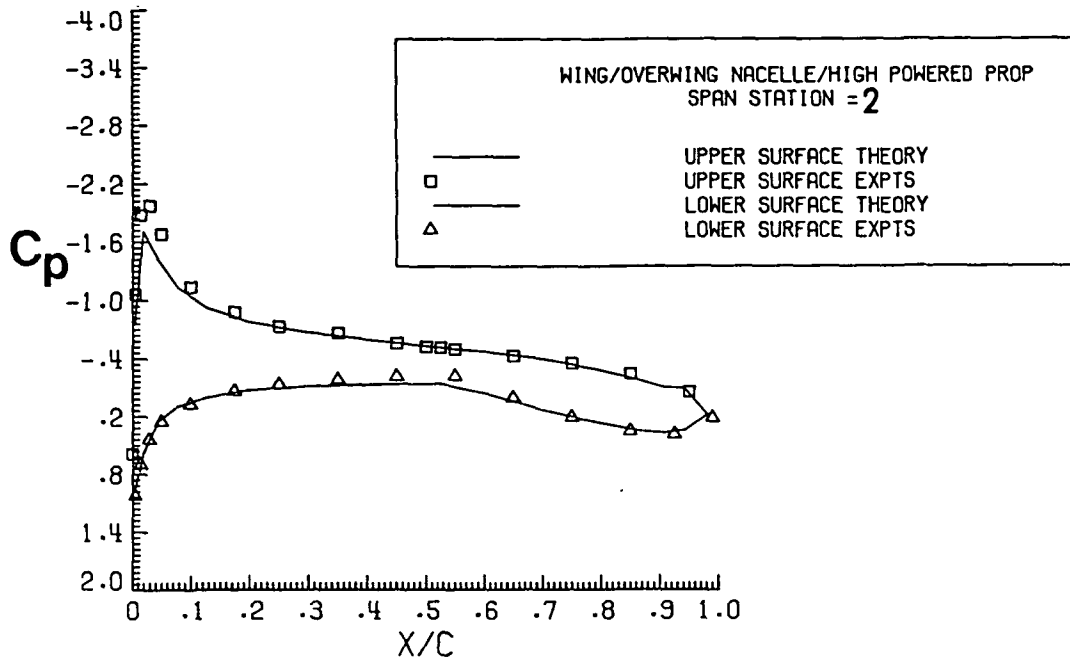


Figure 21. Continued.

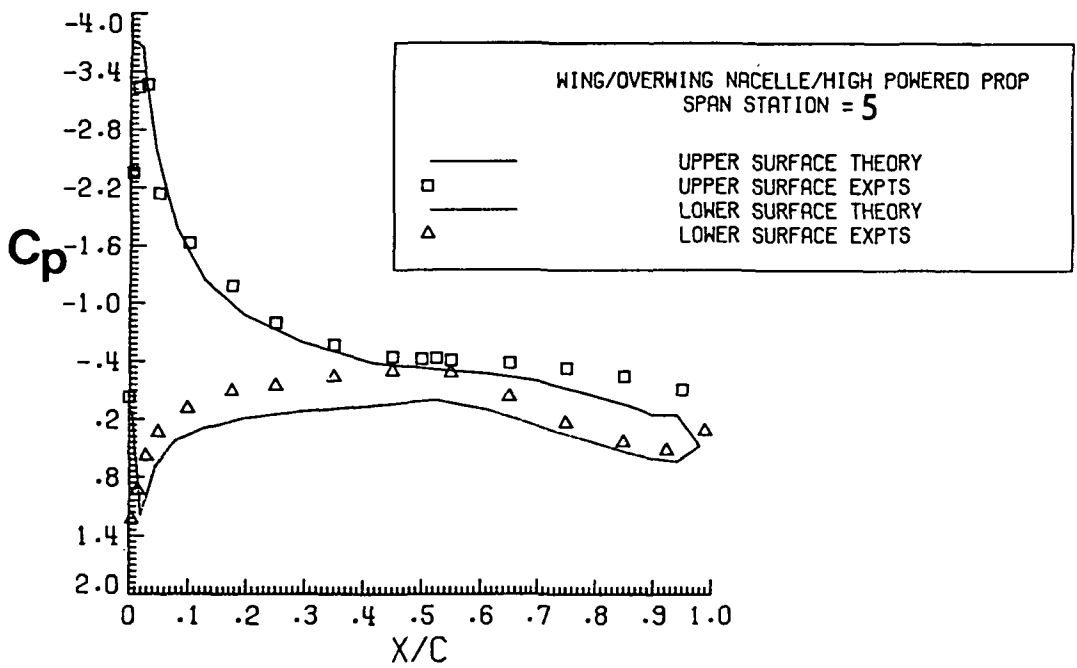
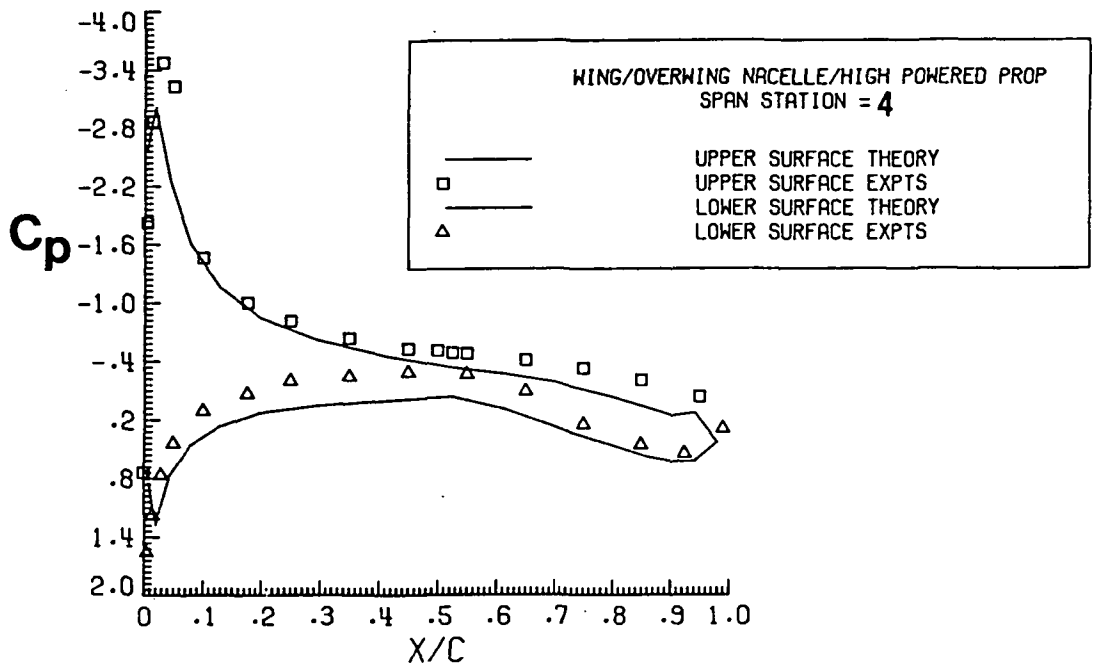


Figure 21. Continued.

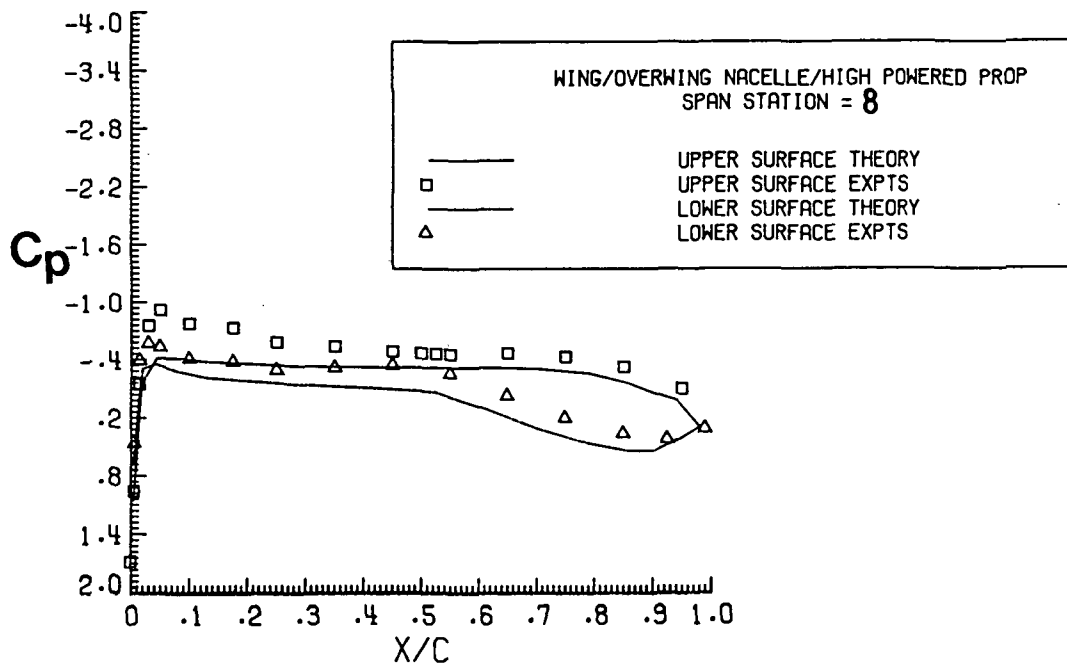
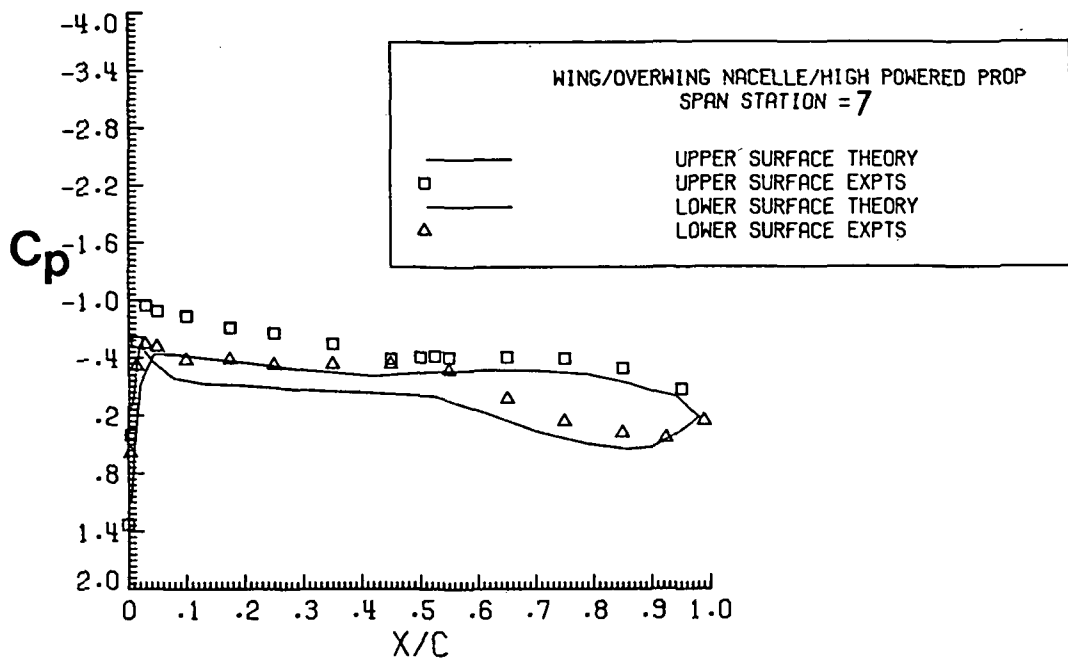


Figure 21. . Continued.

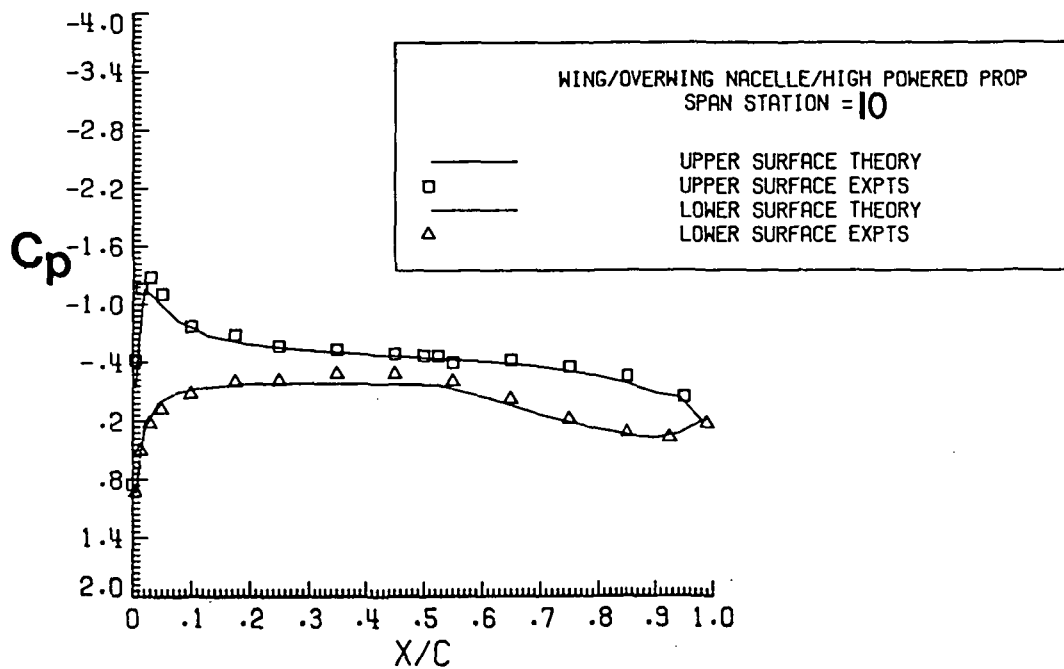
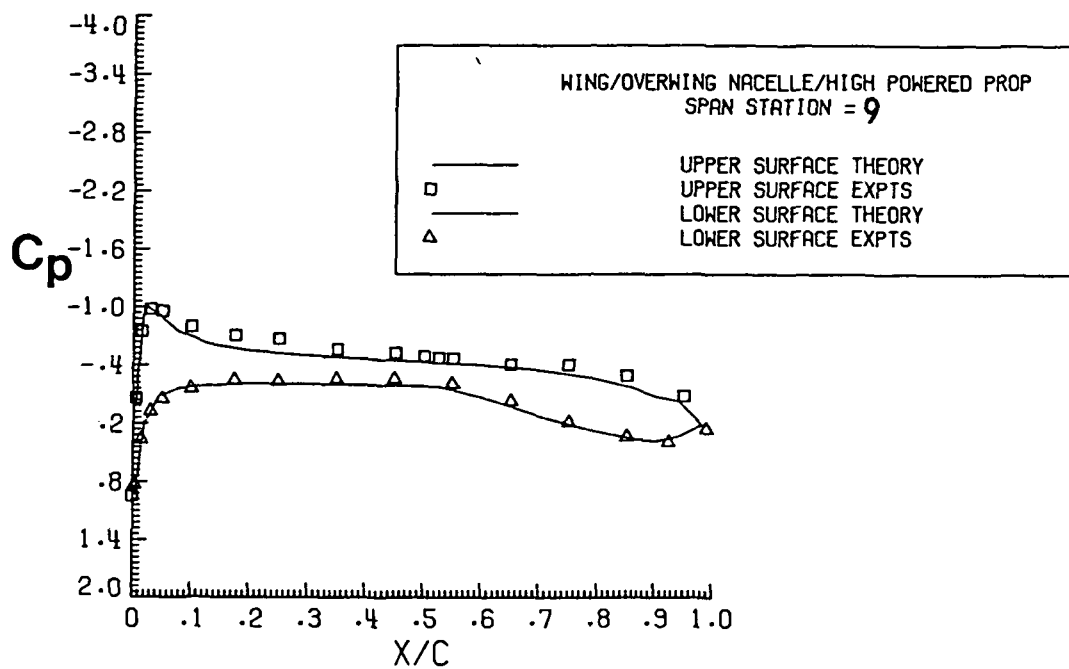


Figure 21. Continued.

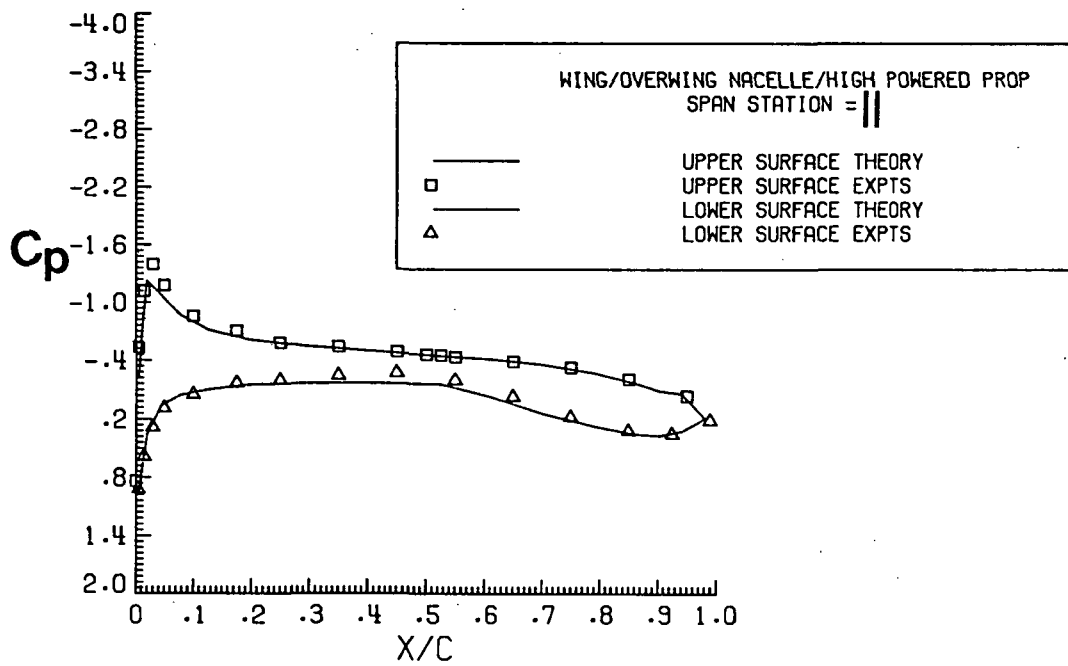


Figure 21. Concluded.

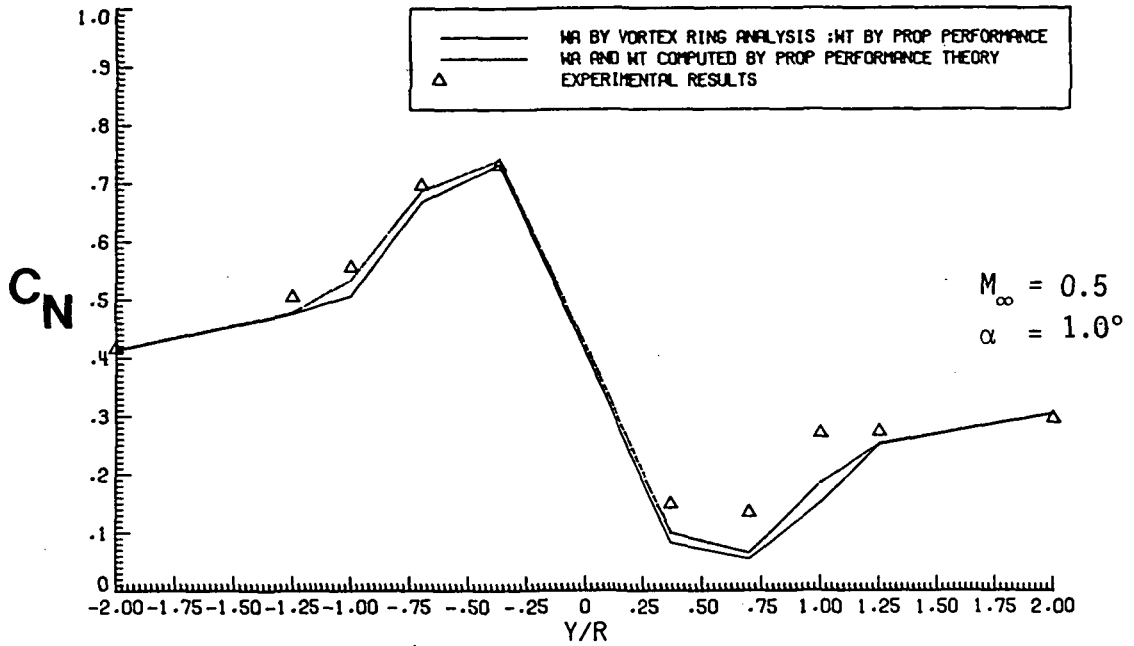


Figure 22. C_N Comparison of the Method II with Method I for High Thrusting Load with $C_T = 0.443$.

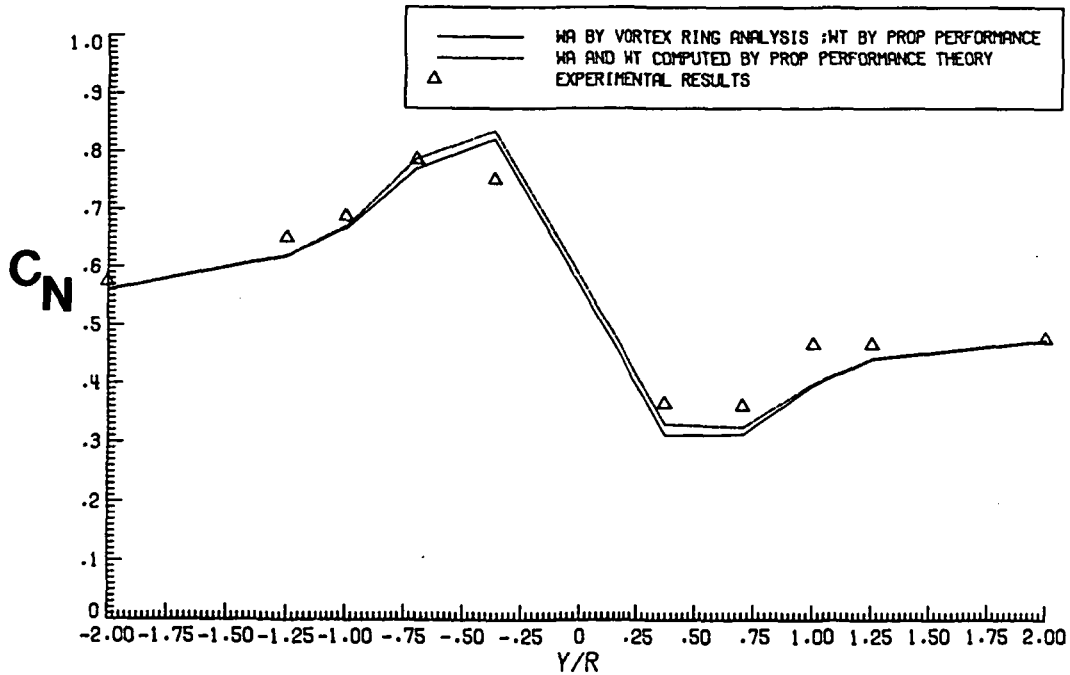


Figure 23. C_N Comparison of Method II with Method I for High Thrusting Load with $C_T = 0.408$, $M_\infty = 0.5$, $\alpha = 2.992$ degrees.

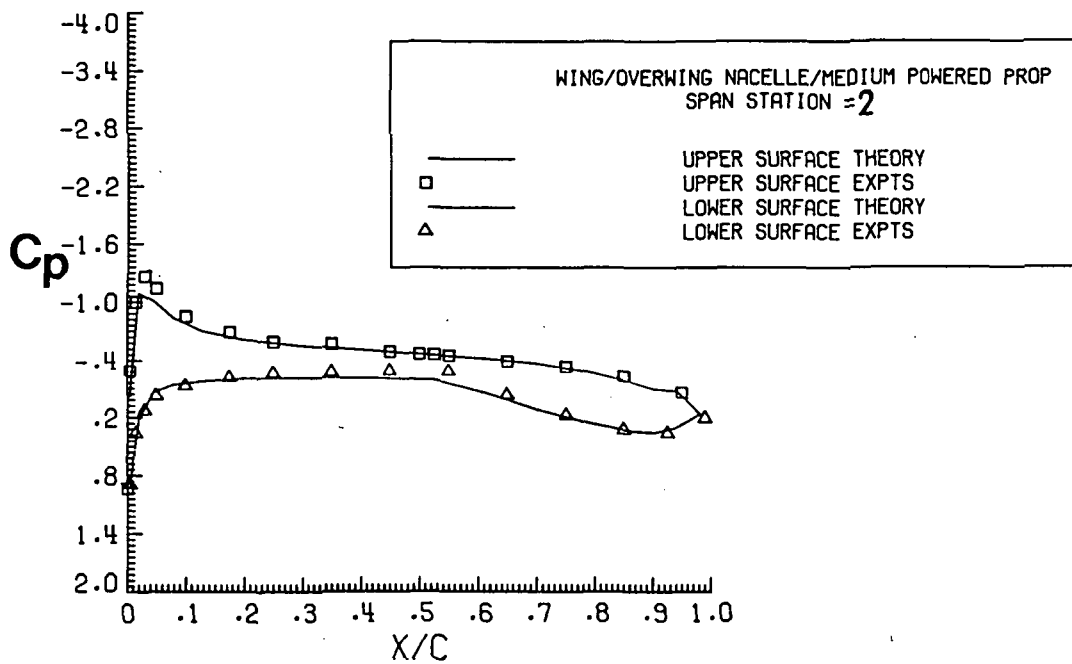
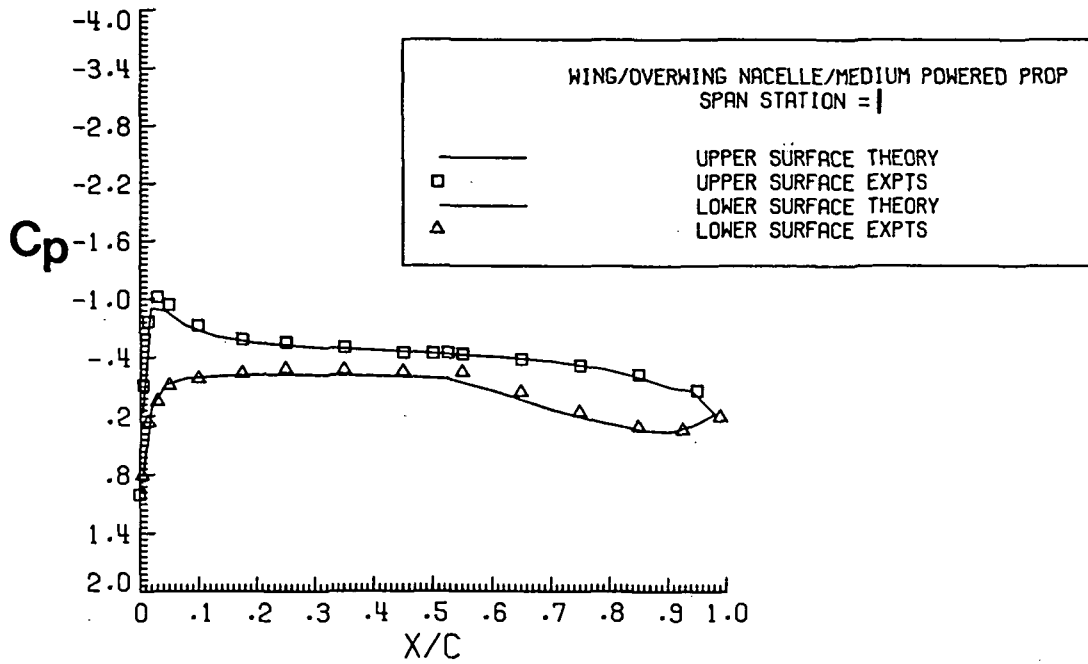


Figure 24. C_p Distribution Comparison for a Medium Power Load with $C_T = 0.338$, $M_\infty = 0.5$, $\alpha = 1.0$ degree.

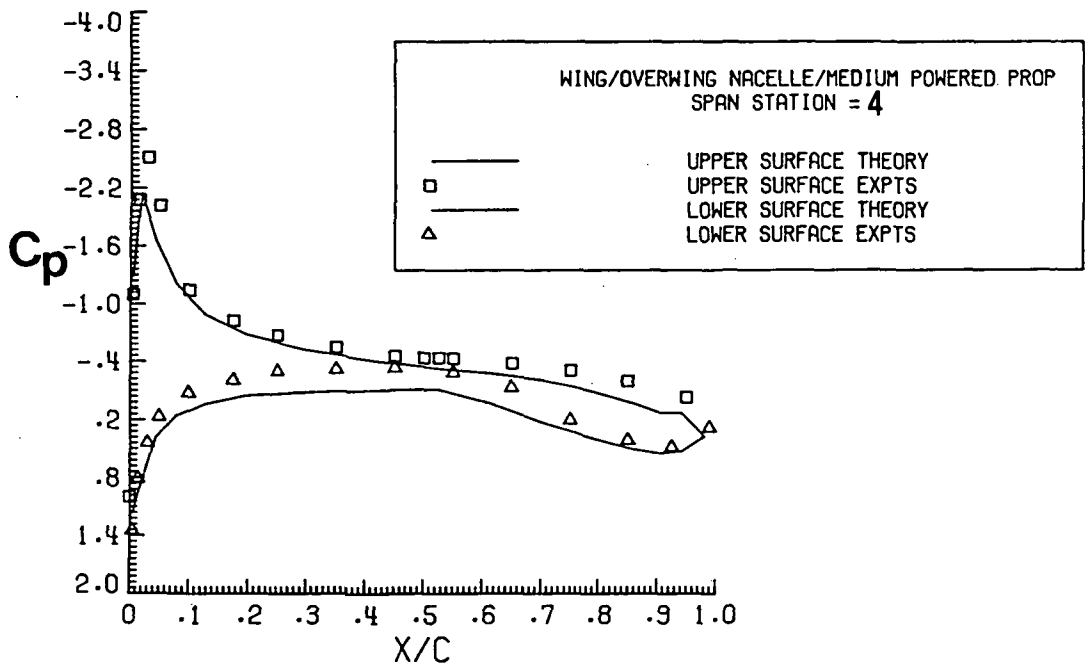
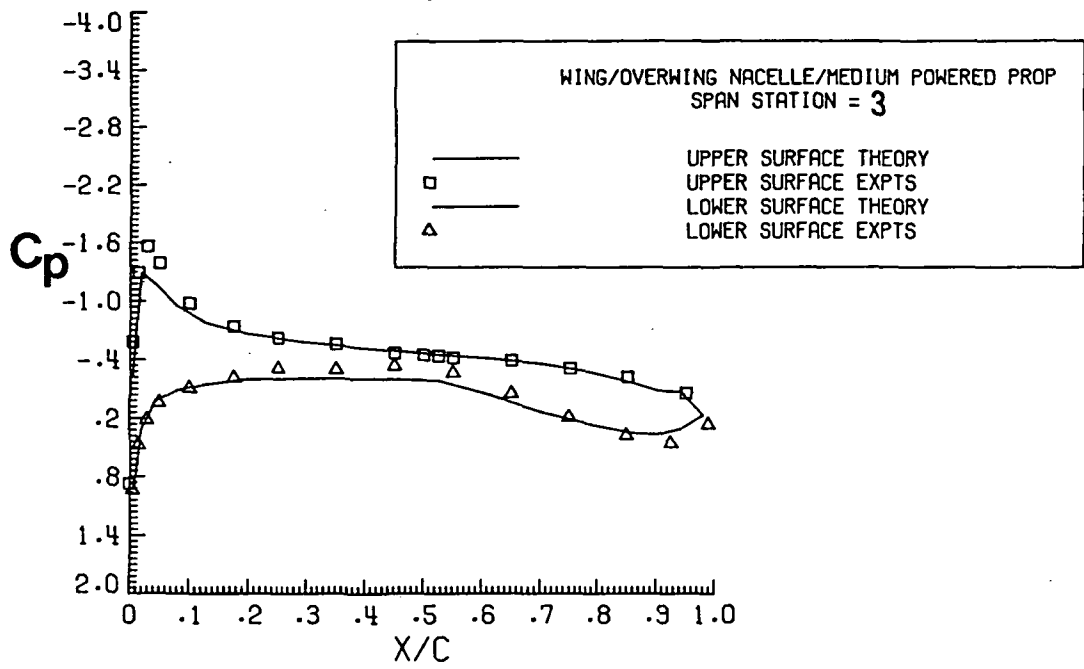


Figure 24. Continued.

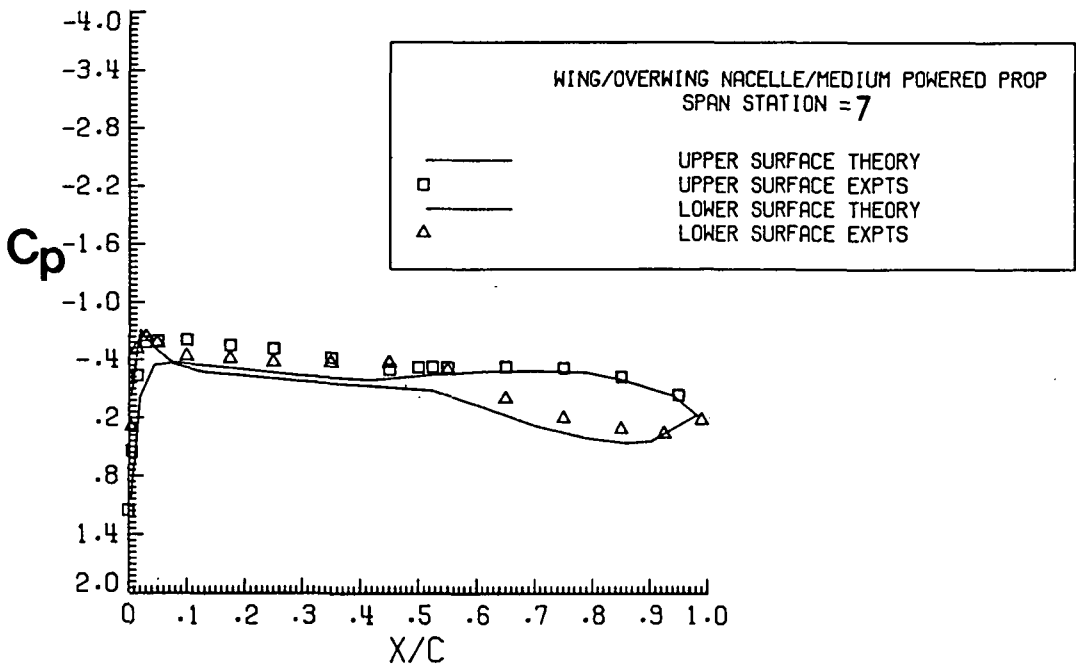
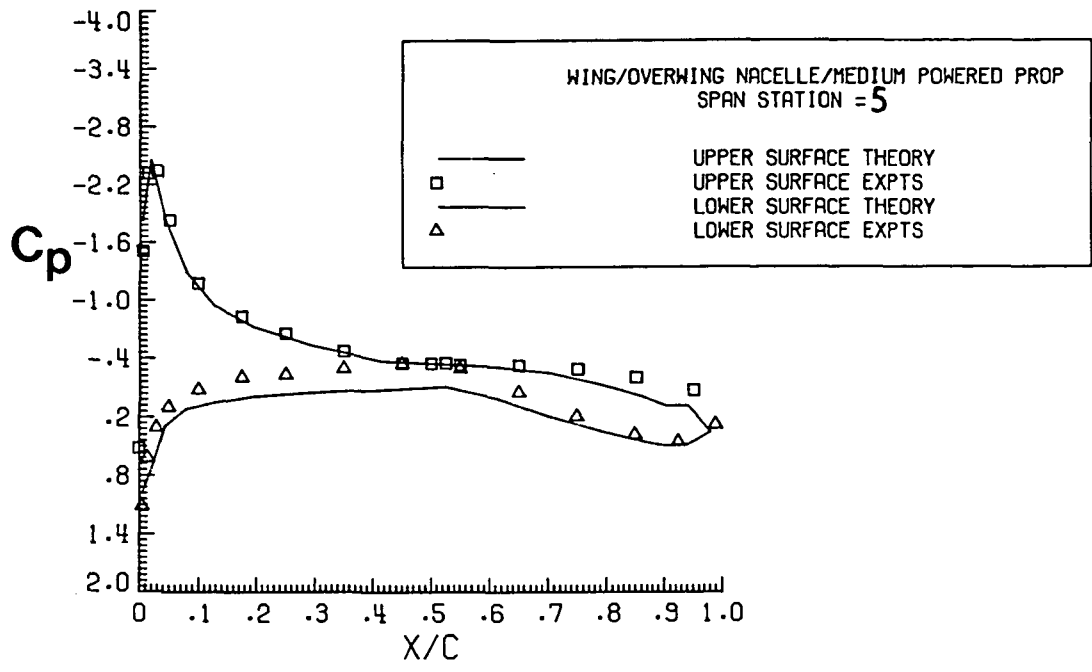


Figure 24. Continued.

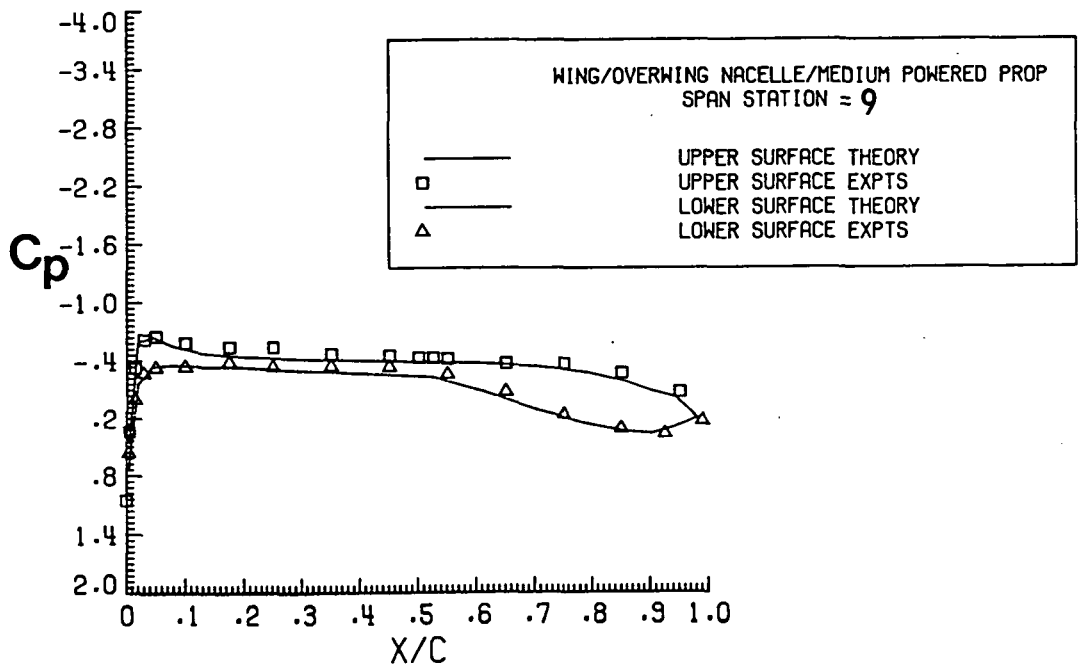
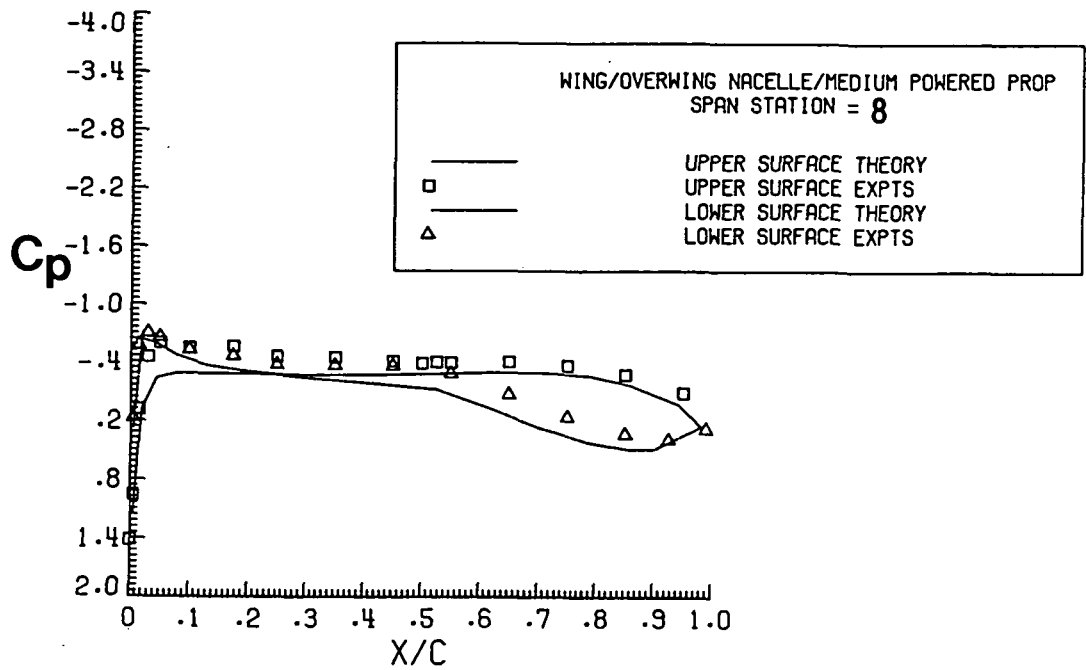


Figure 24. Continued.

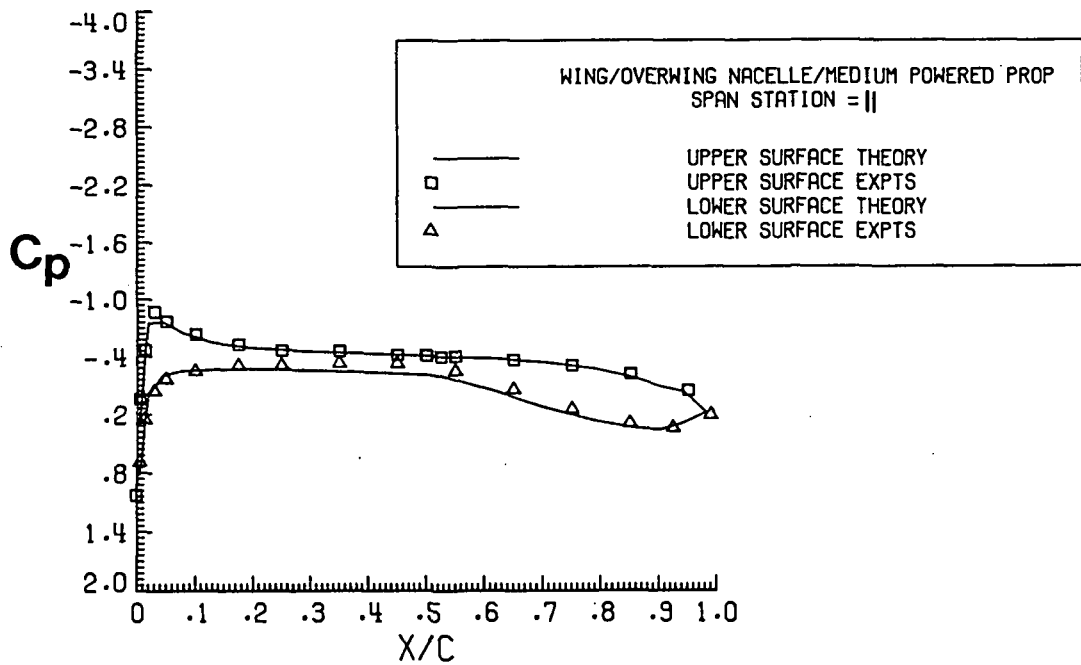
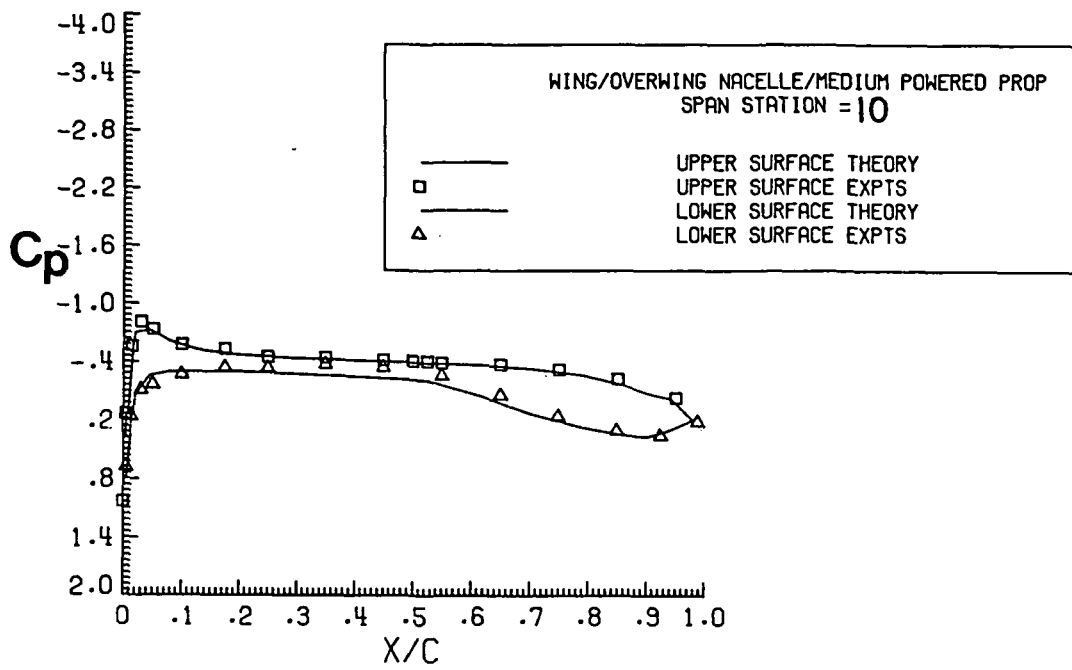


Figure 24. Concluded.

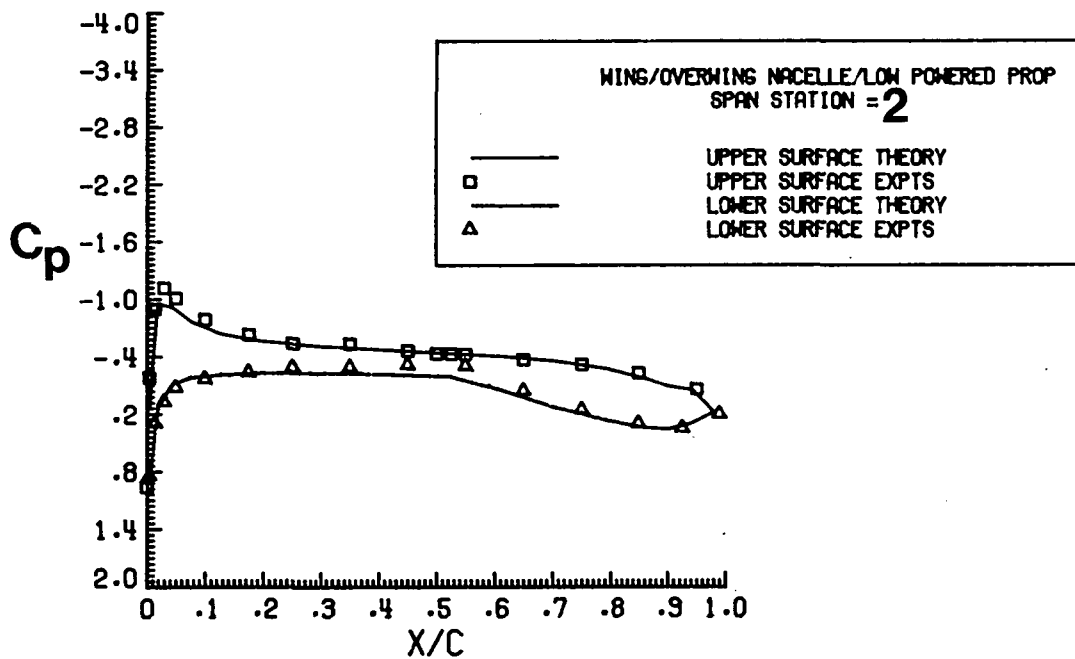
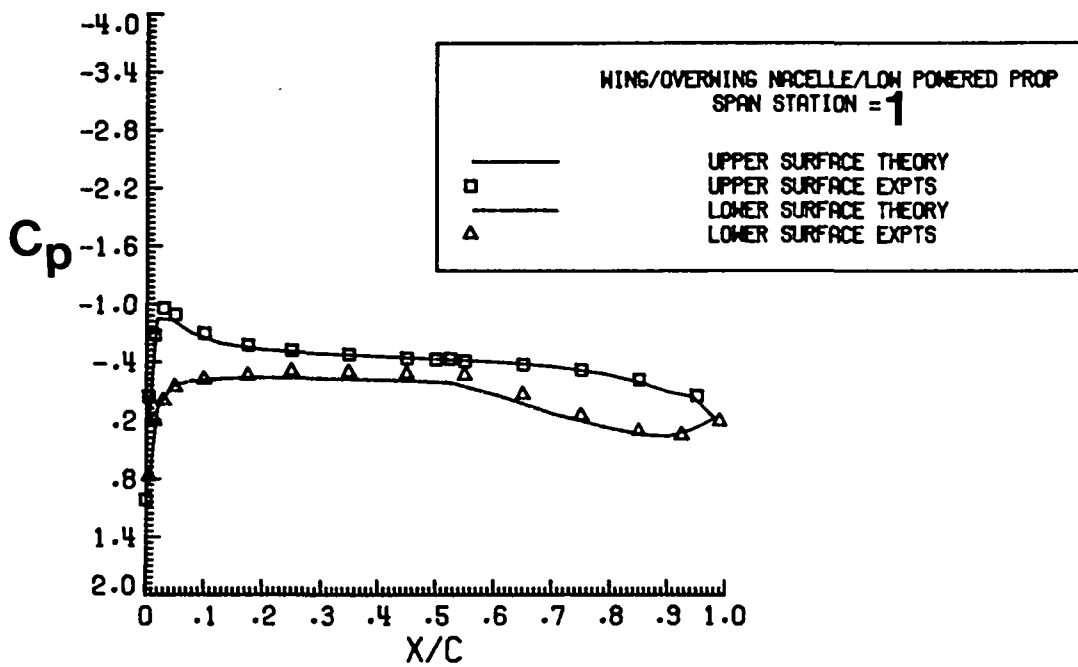


Figure 25. C_p Comparison for a Low Power Load with $C_T = 0.137$,
 $M_\infty = 0.5$, $\alpha = 1.0$ degree.

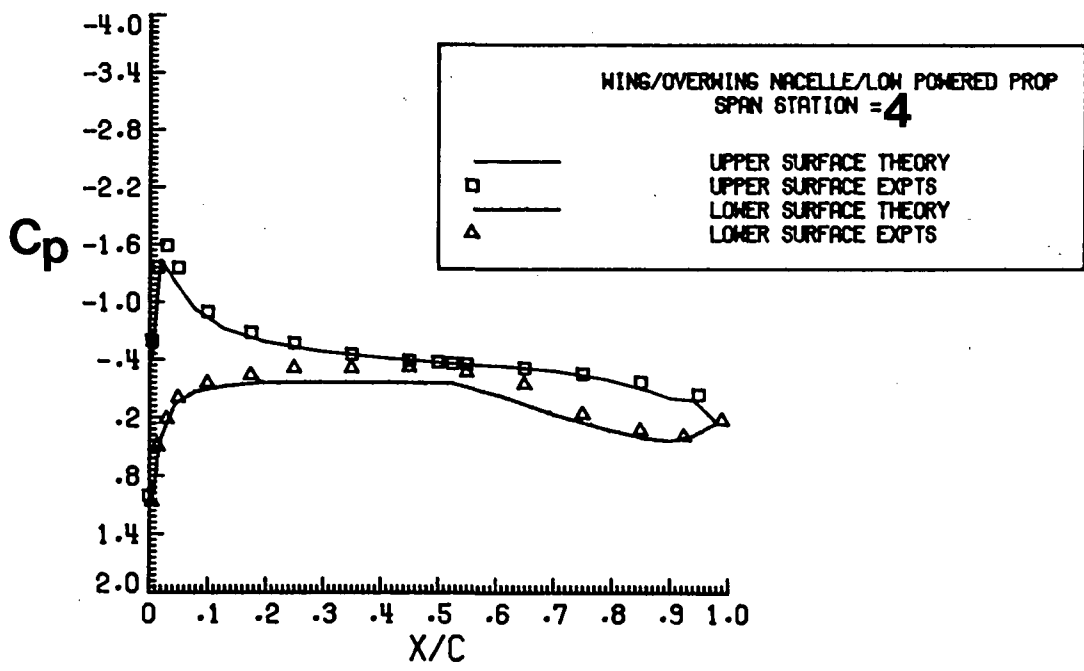
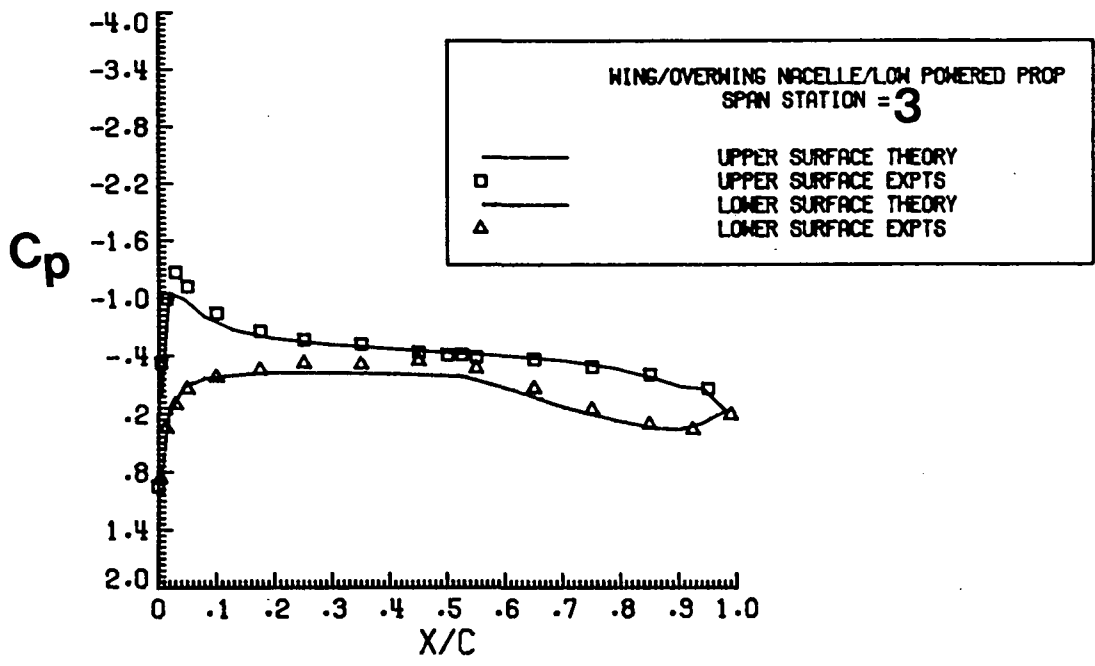


Figure 25. Continued.

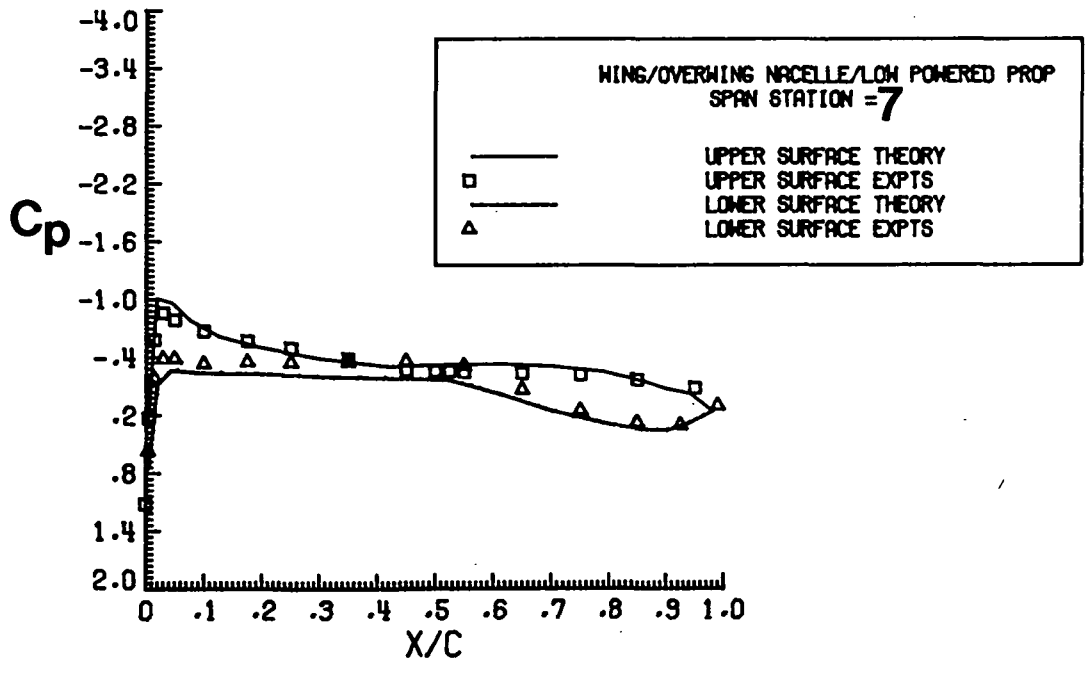
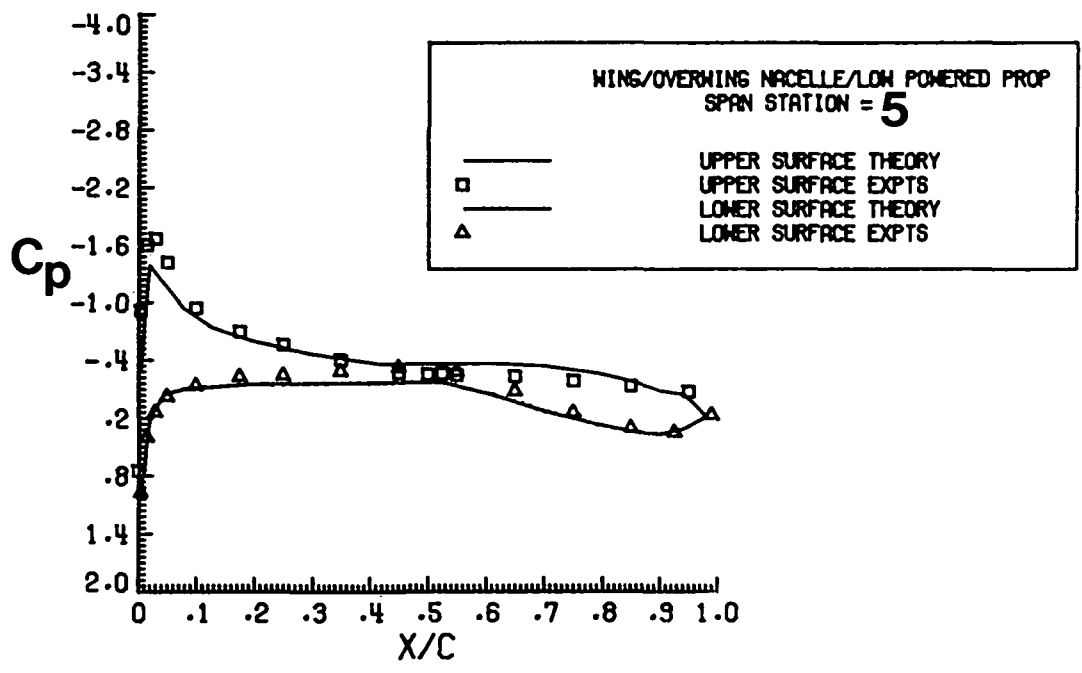


Figure 25. Continued.

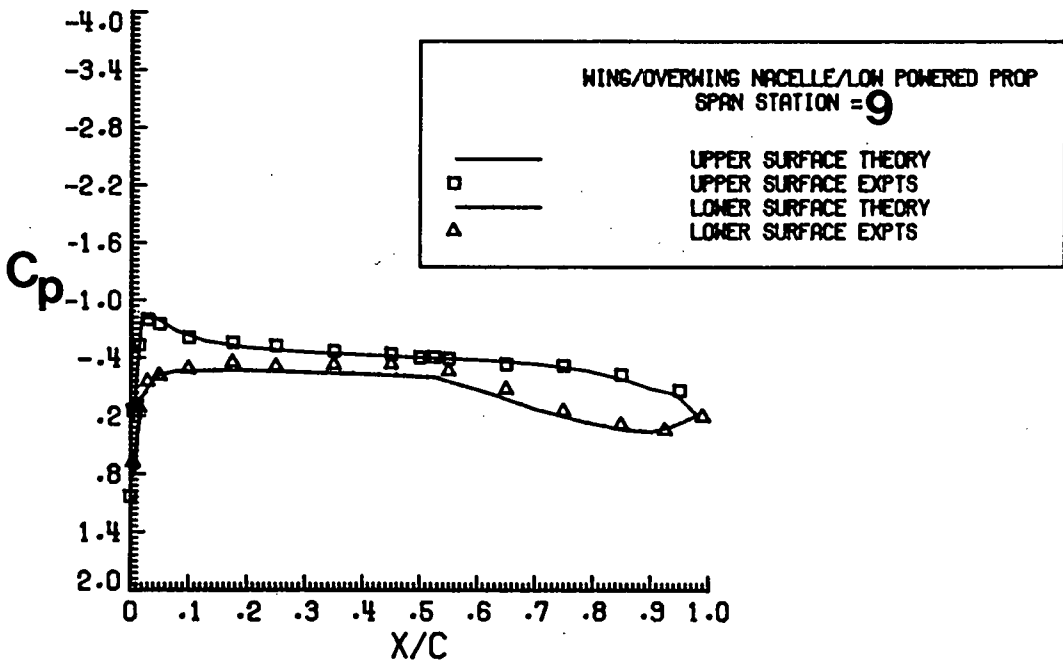
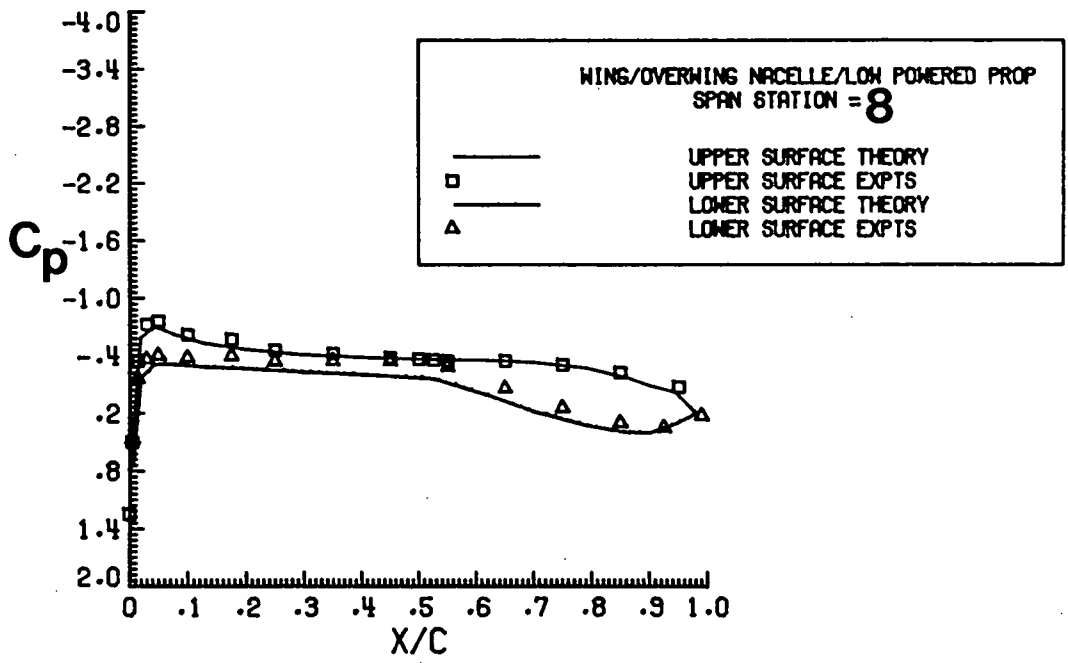


Figure 25. Continued.

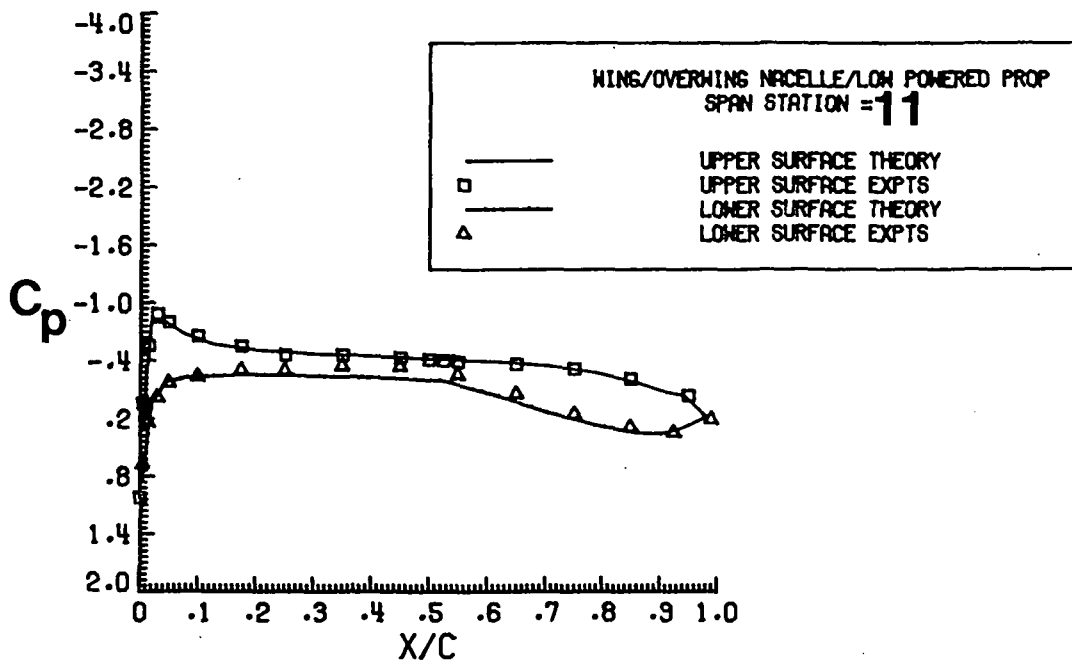
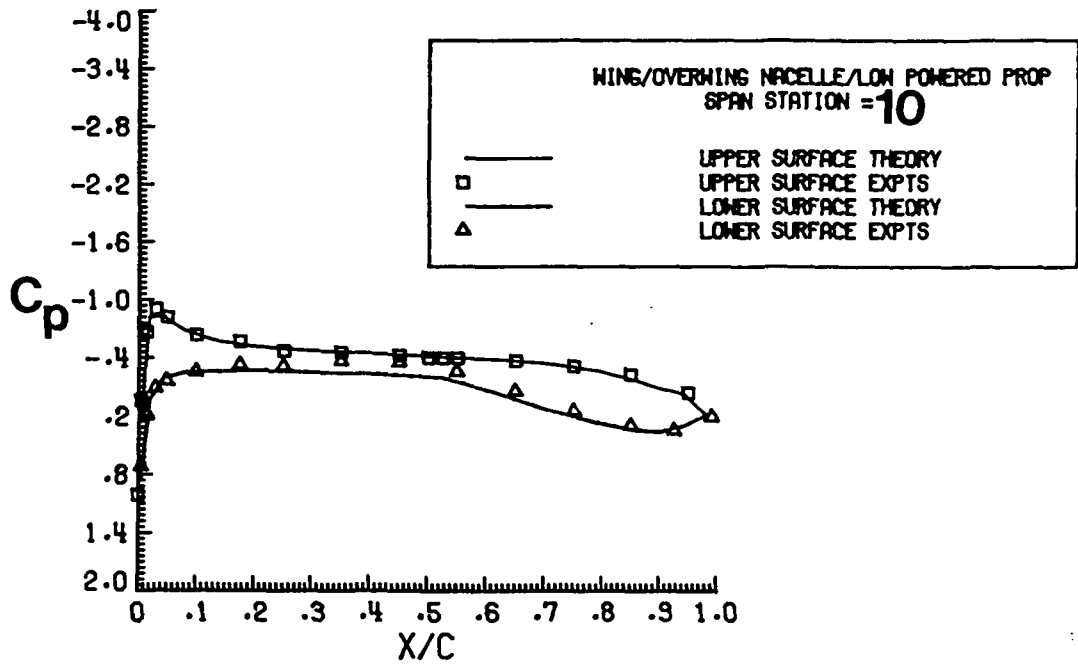


Figure 25. Concluded.

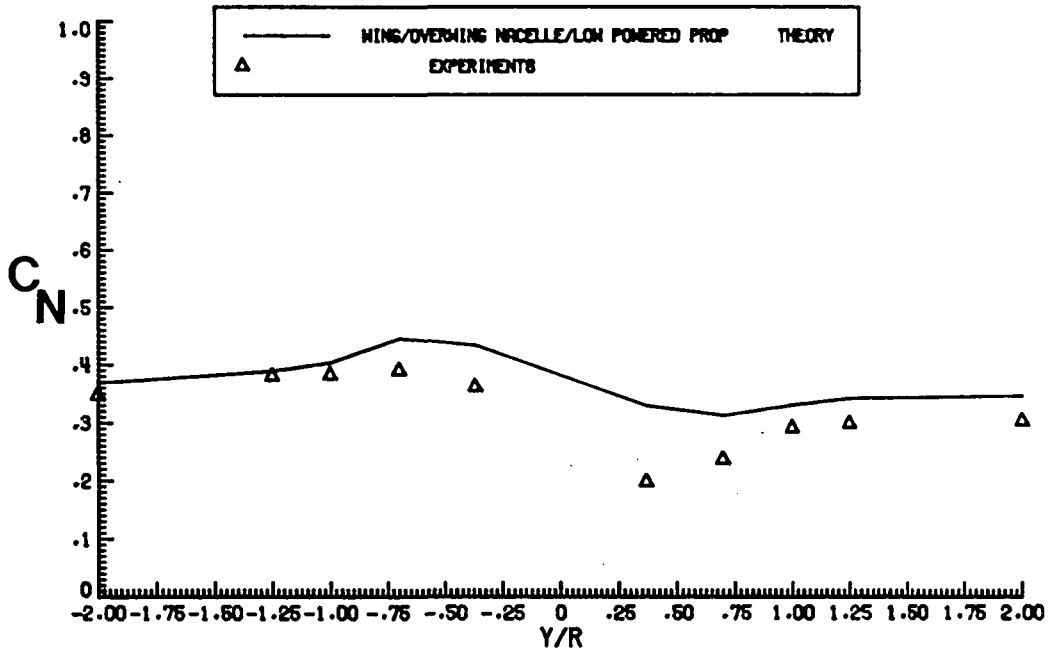


Figure 26. C_N Comparison for a Low Power Load with $C_T = 0.137$, $M_\infty = 0.5$, $\alpha = 1.0$ degree.

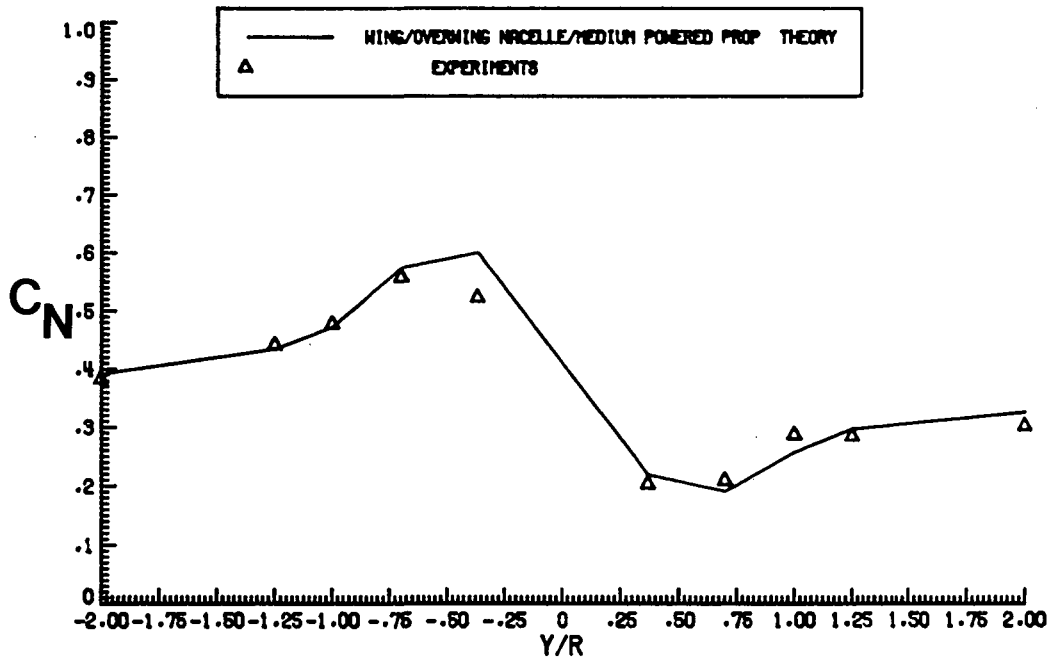


Figure 27. C_N Comparison for a Medium Power Load with $C_T = 0.338$, $M_\infty = 0.5$, $\alpha = 1.0$ degree.

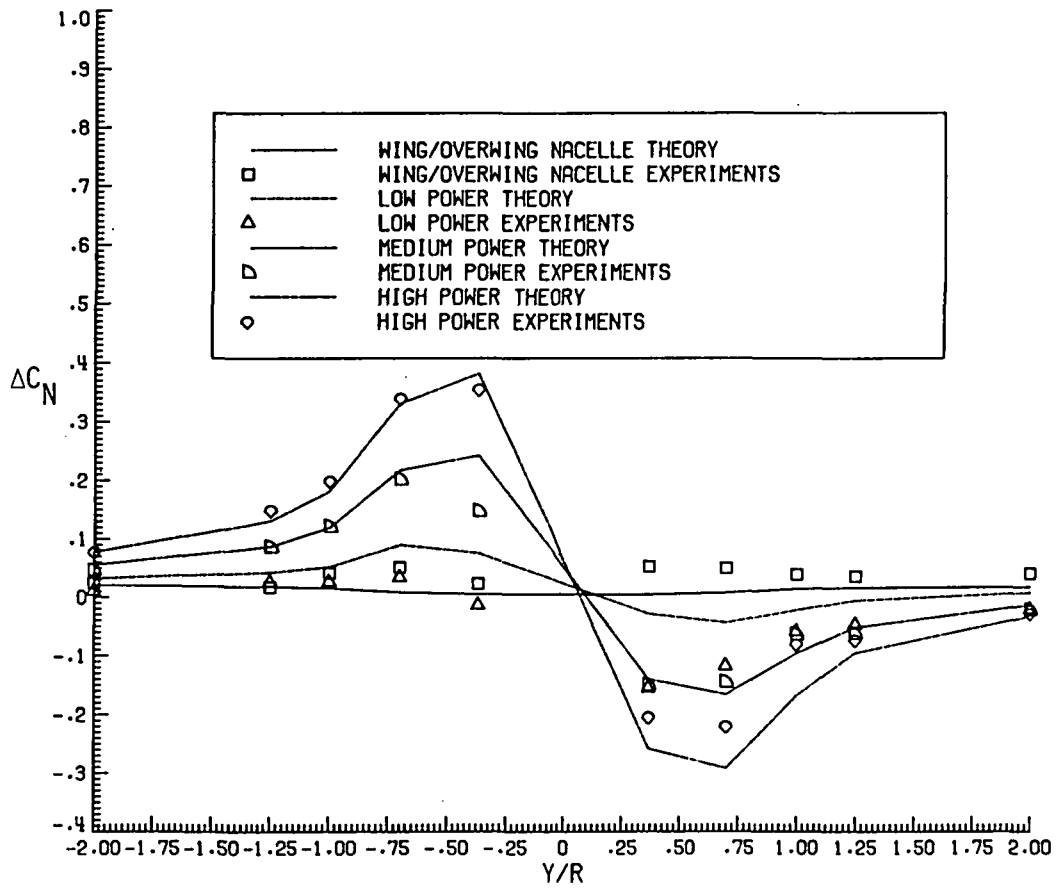


Figure 28. Interference Effect on C_N by the Addition of overwing Nacelle/Powered Propeller to the Basic Wing Configuration, $M_\infty = 0.5$, $\alpha = 1.0$ degree.

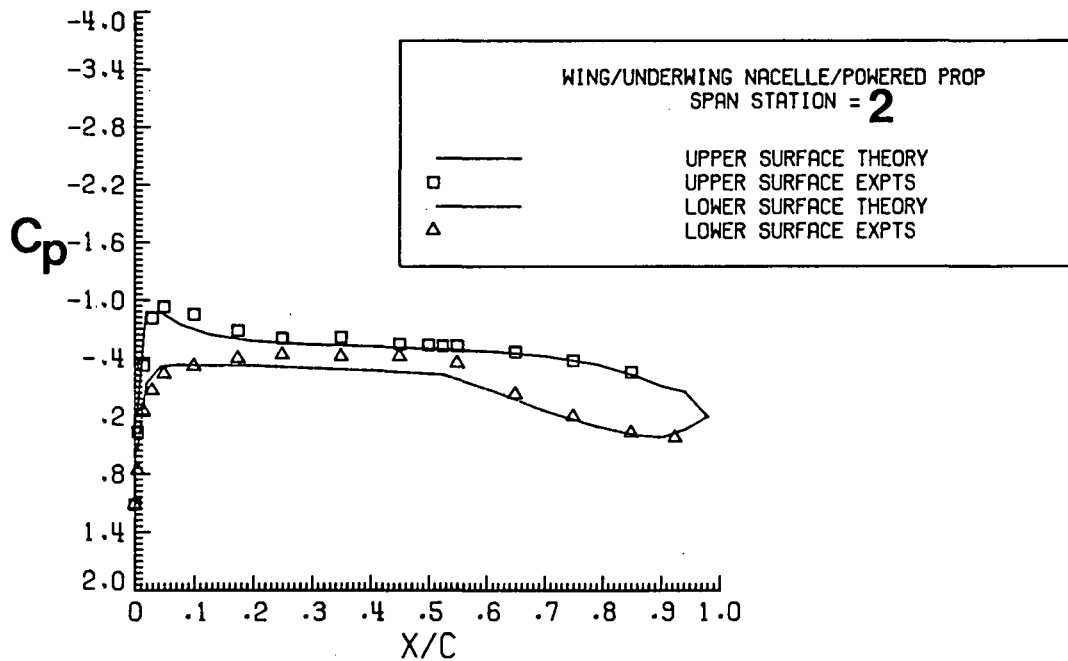
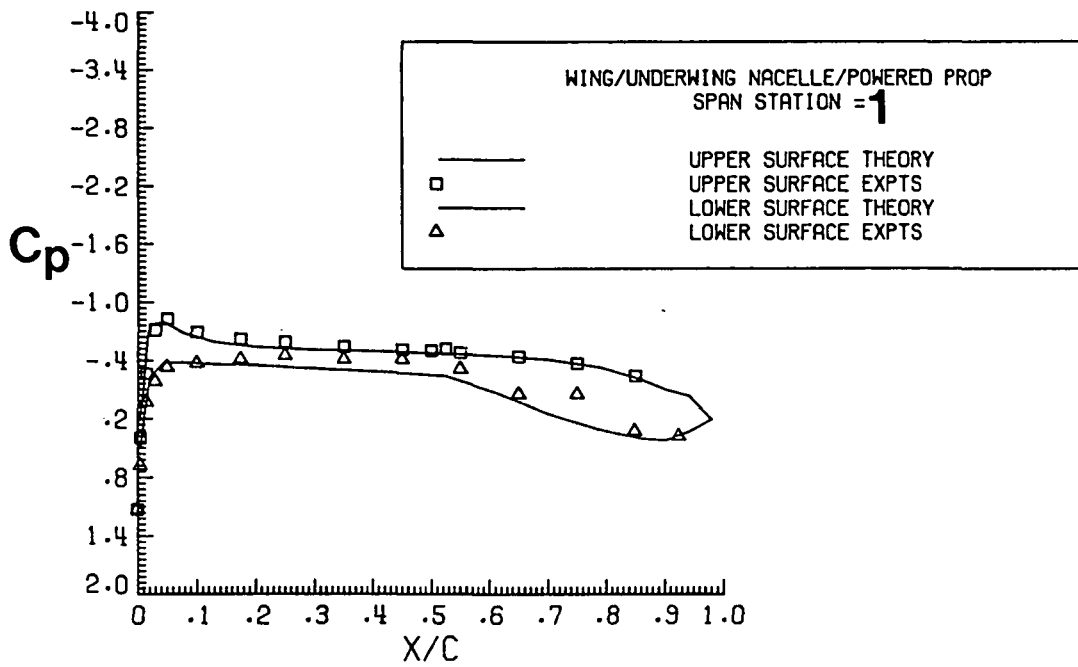


Figure 29. C_p Comparison for the Wing/Underwing Nacelle/Powered Propeller with $C_T = 0.466$, $M_\infty = 0.701$, $\alpha = 0.0$ degree, Method II, without boundary layer.

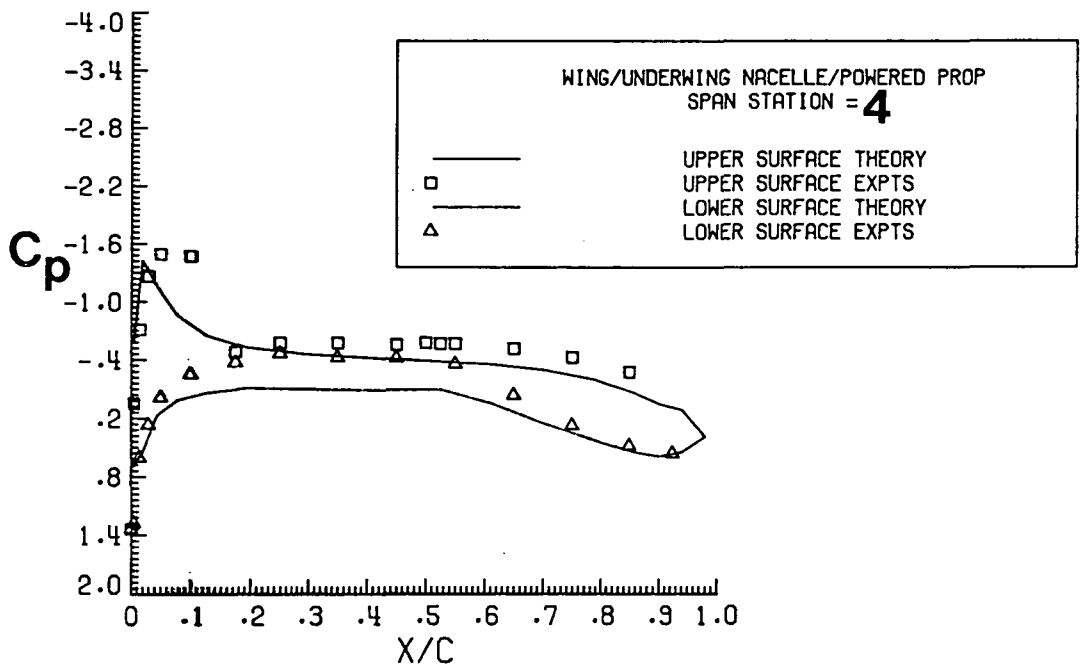
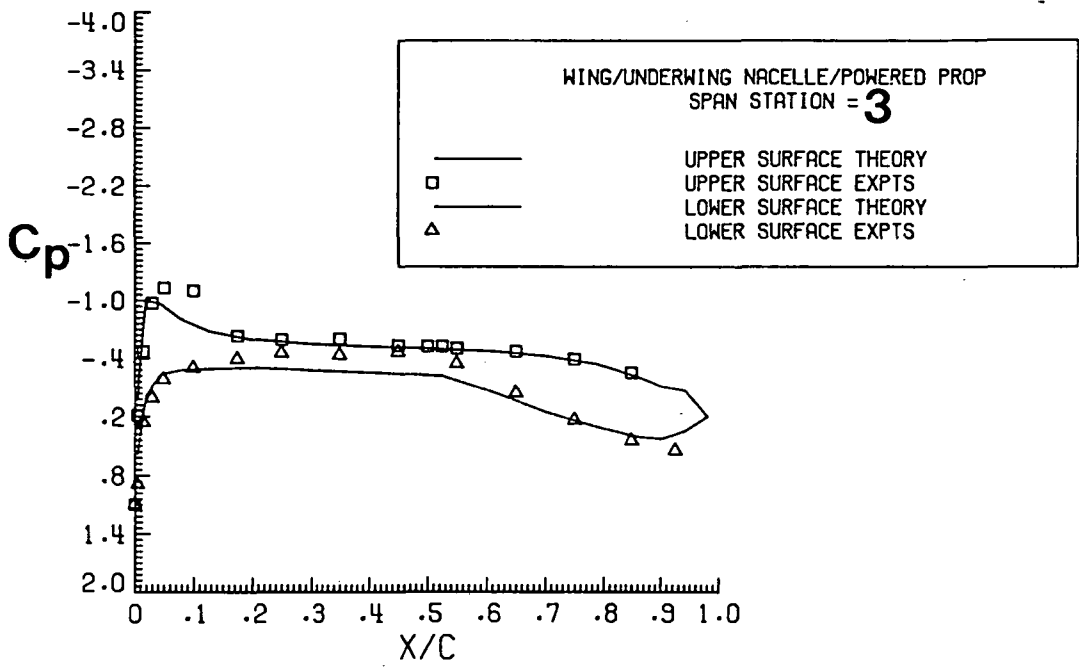


Figure 29. Continued.

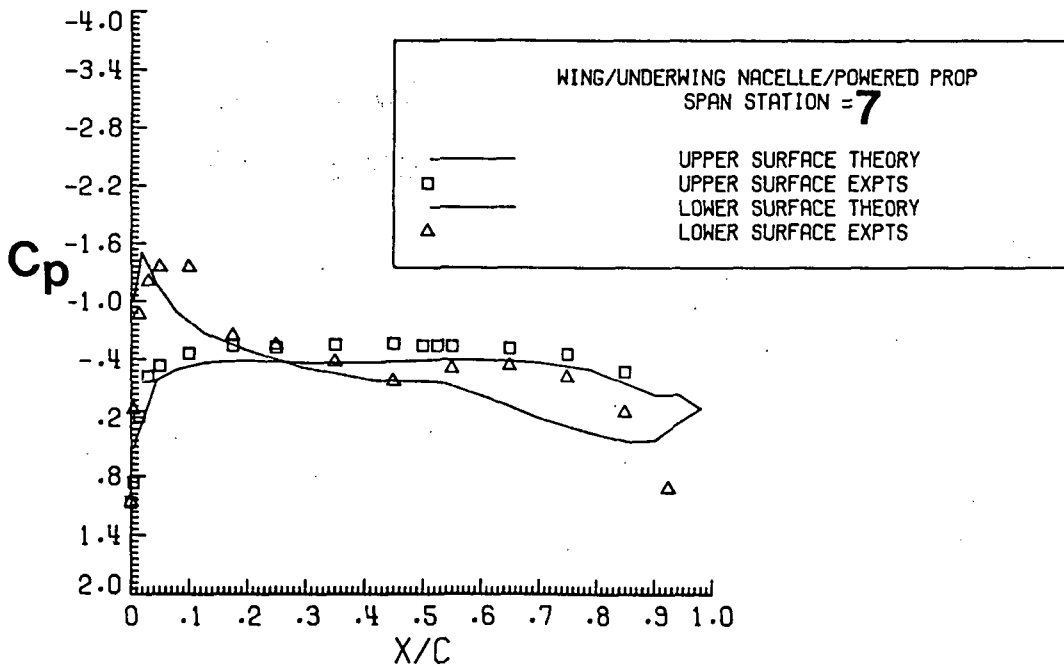
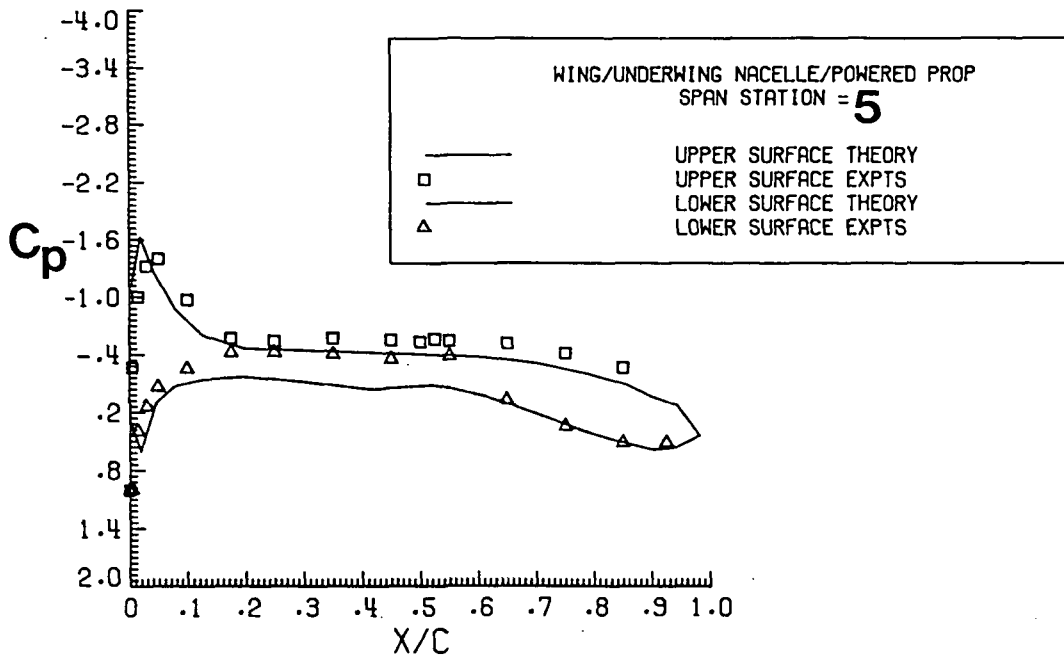


Figure 29. Continued.

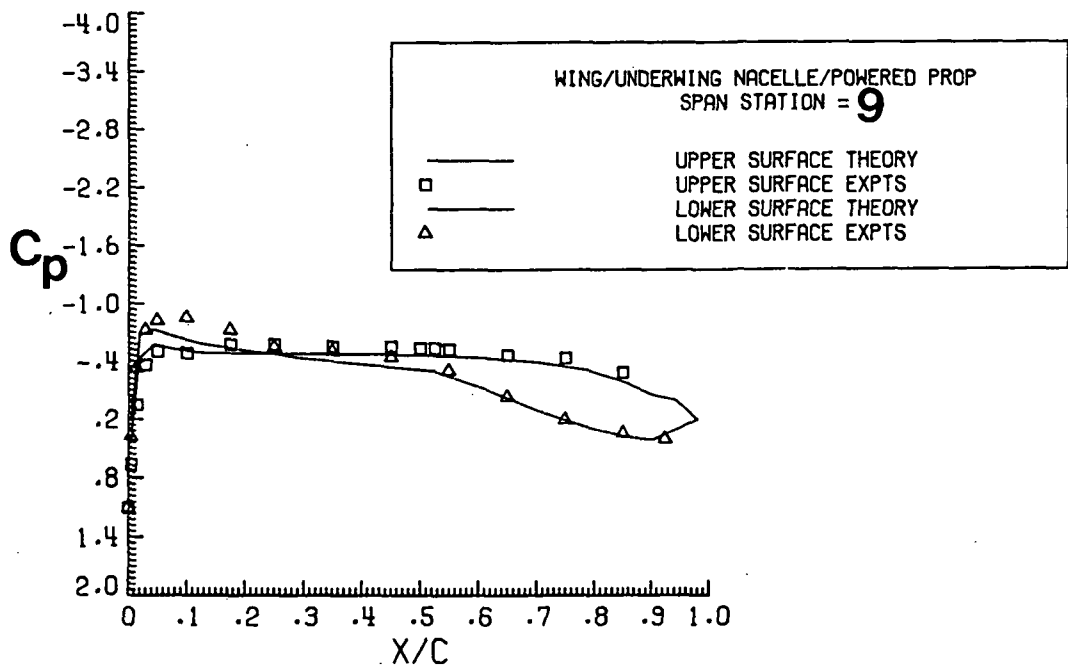
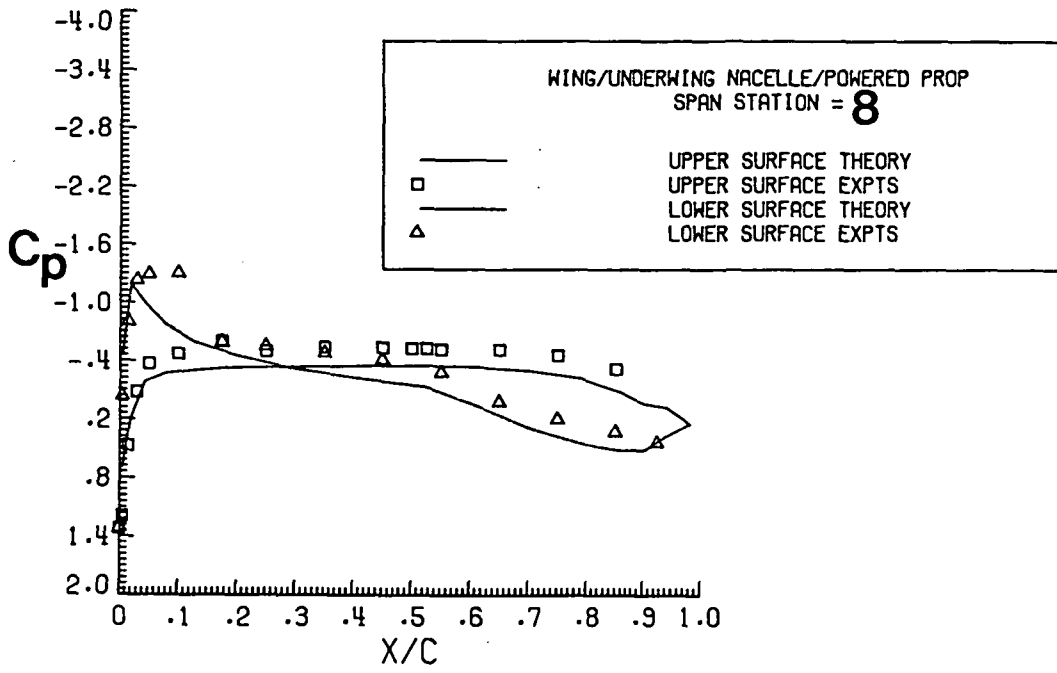


Figure 29. Continued.

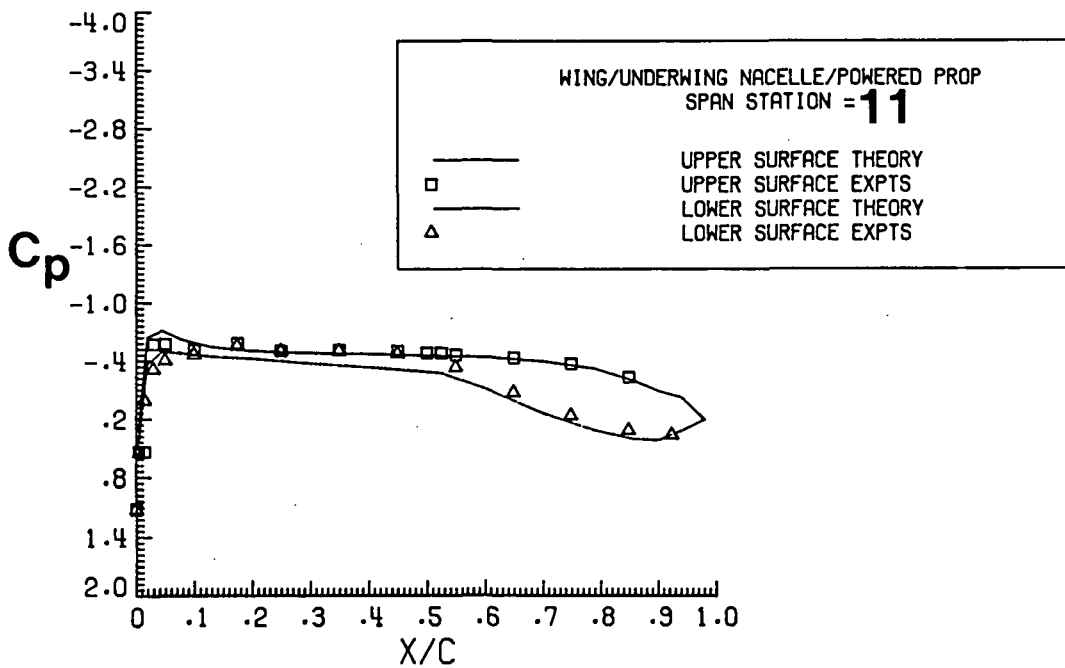
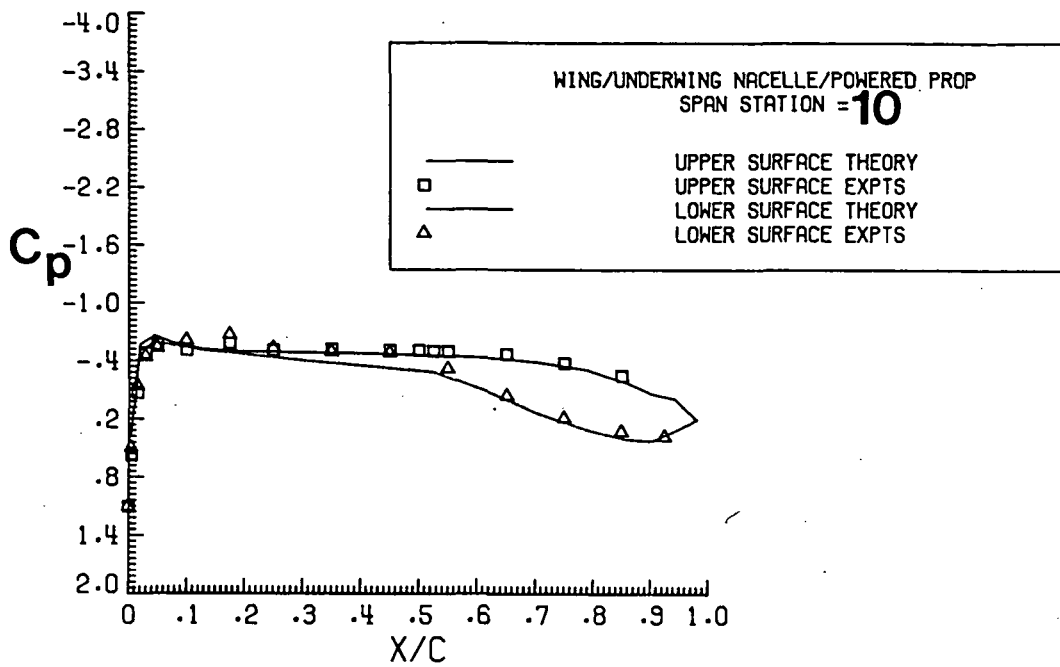


Figure 29. Concluded.

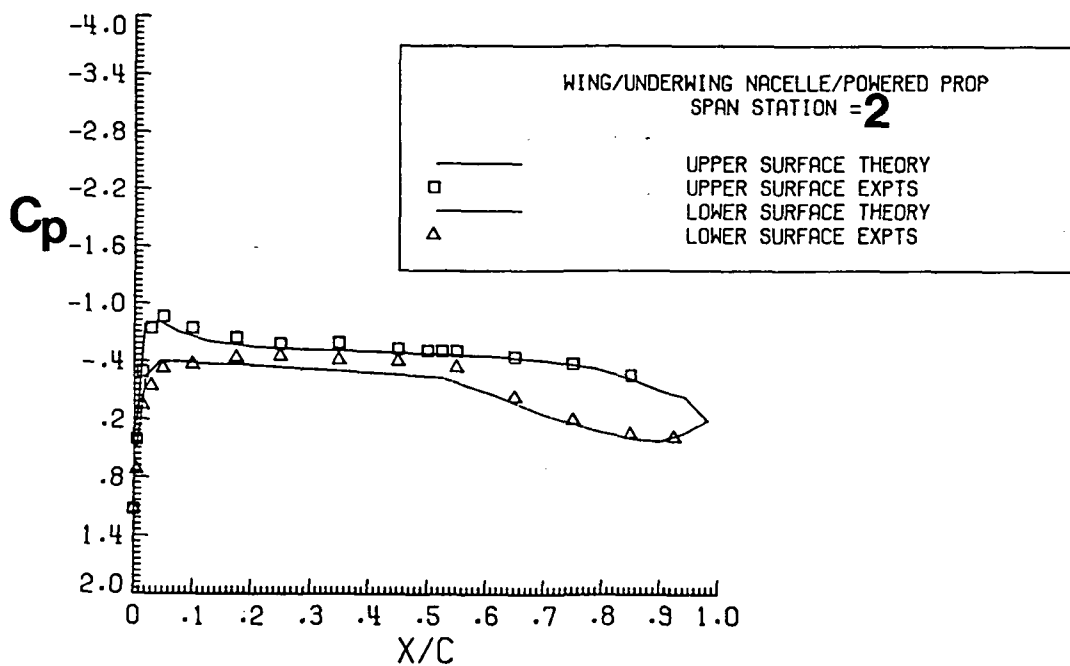
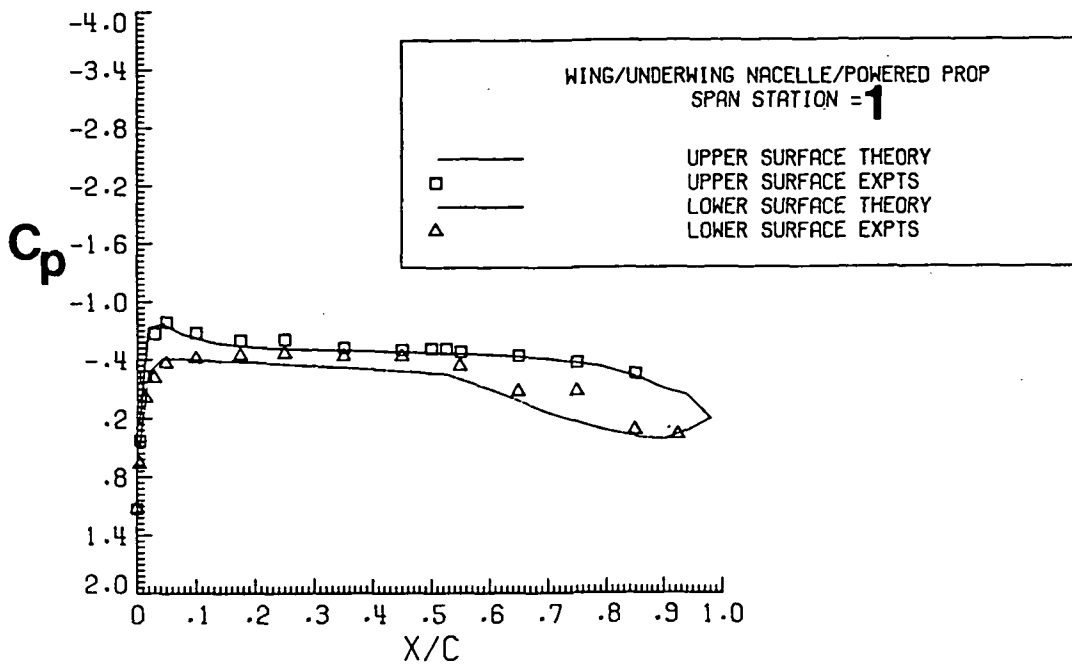


Figure 30. C_p Comparison for the Wing/Underwing Nacelle/Powered Propeller with $C_T = .245$, $M_\infty = 0.700$, $\alpha = 0.0$ degree, Method II, without boundary layer.

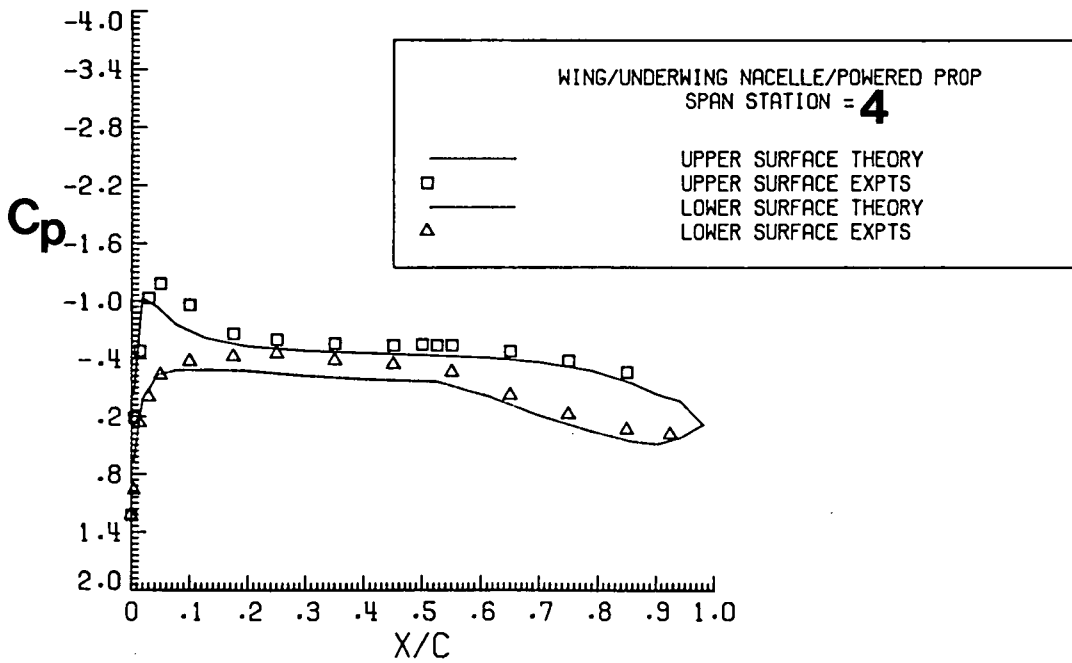
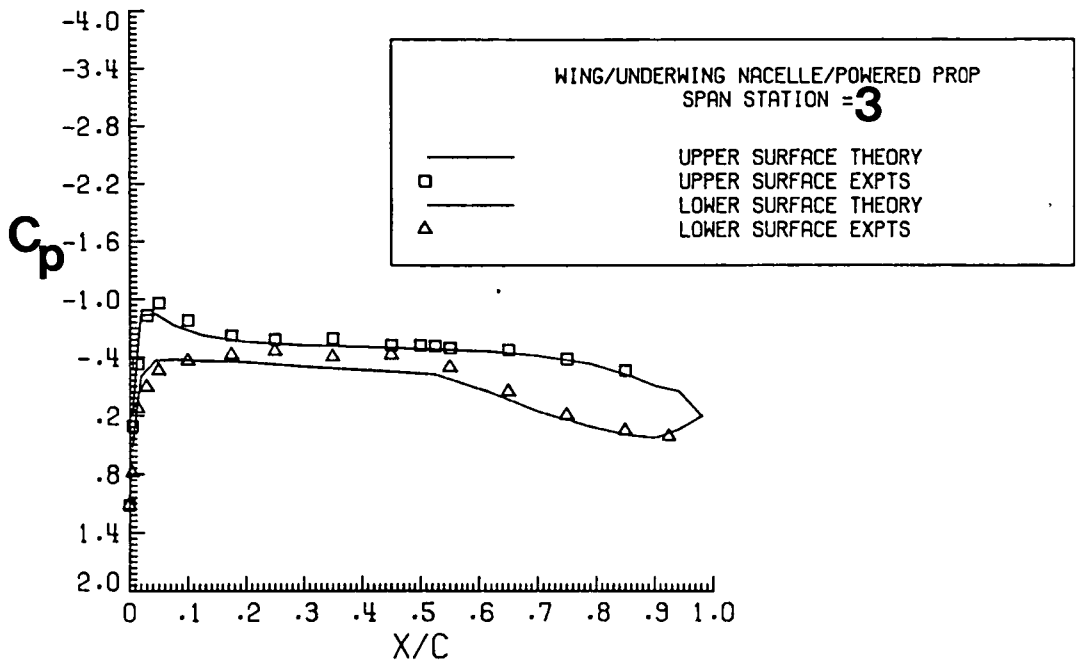


Figure 30. Continued.

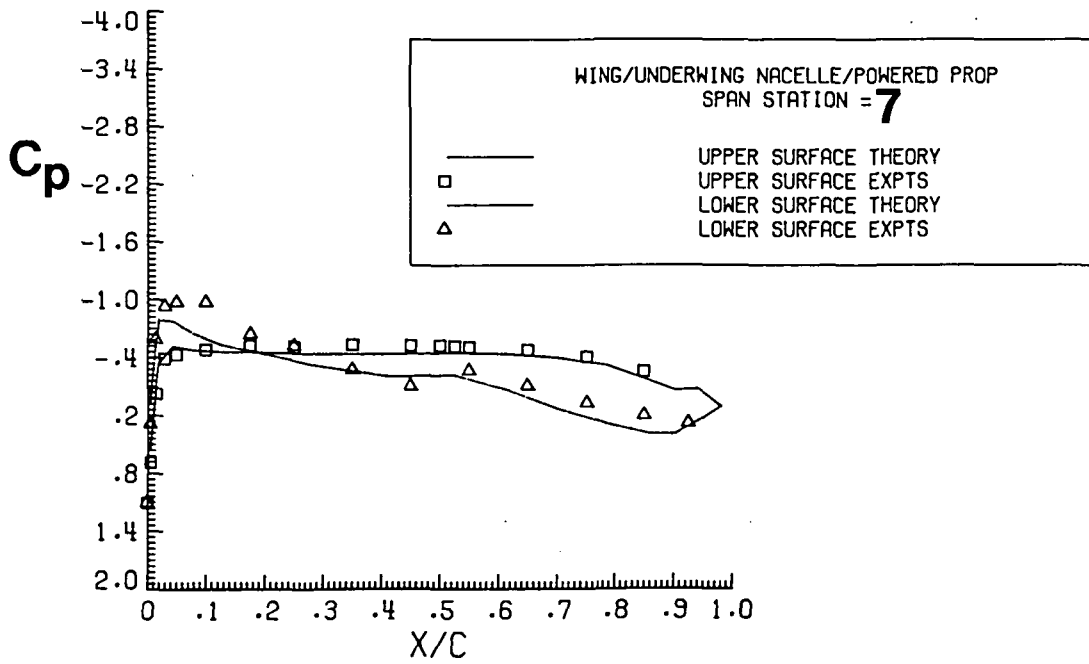
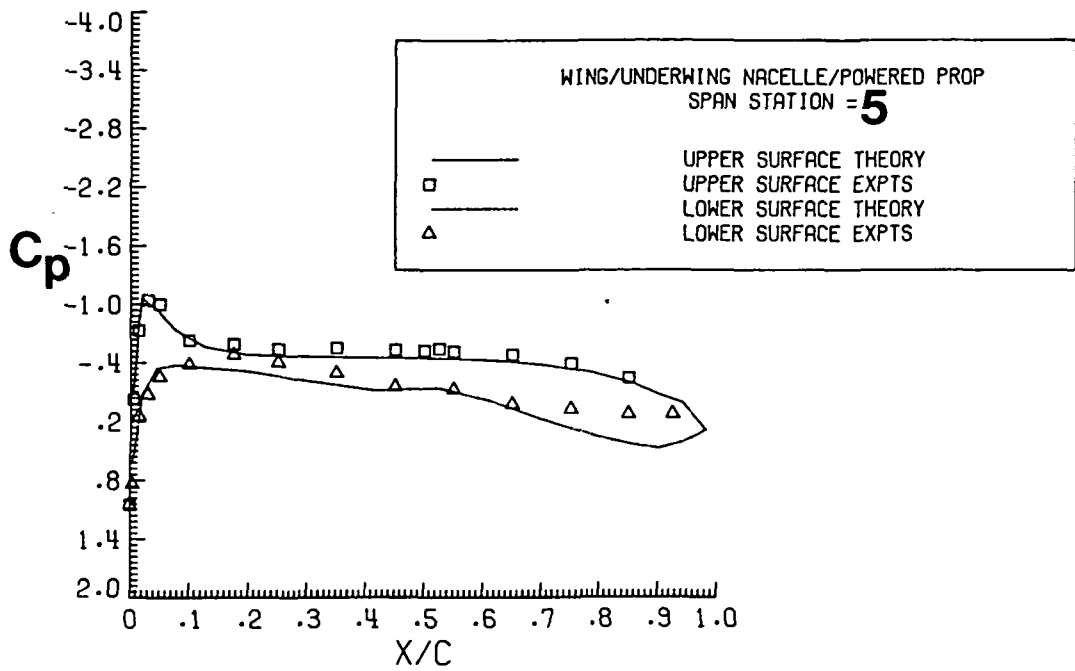


Figure 30. Continued.

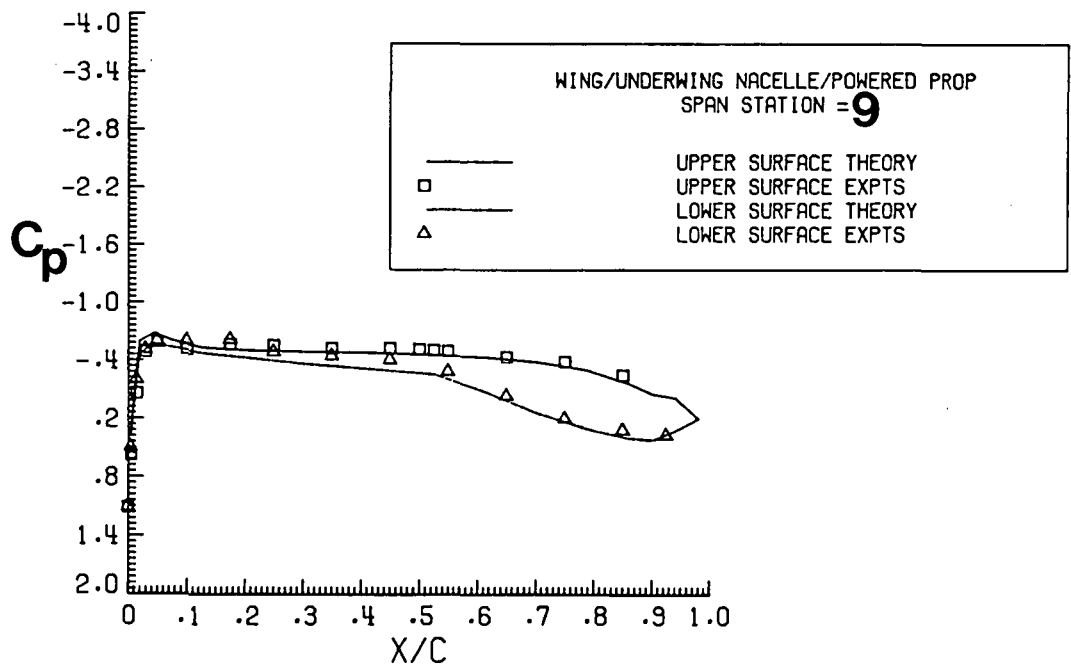
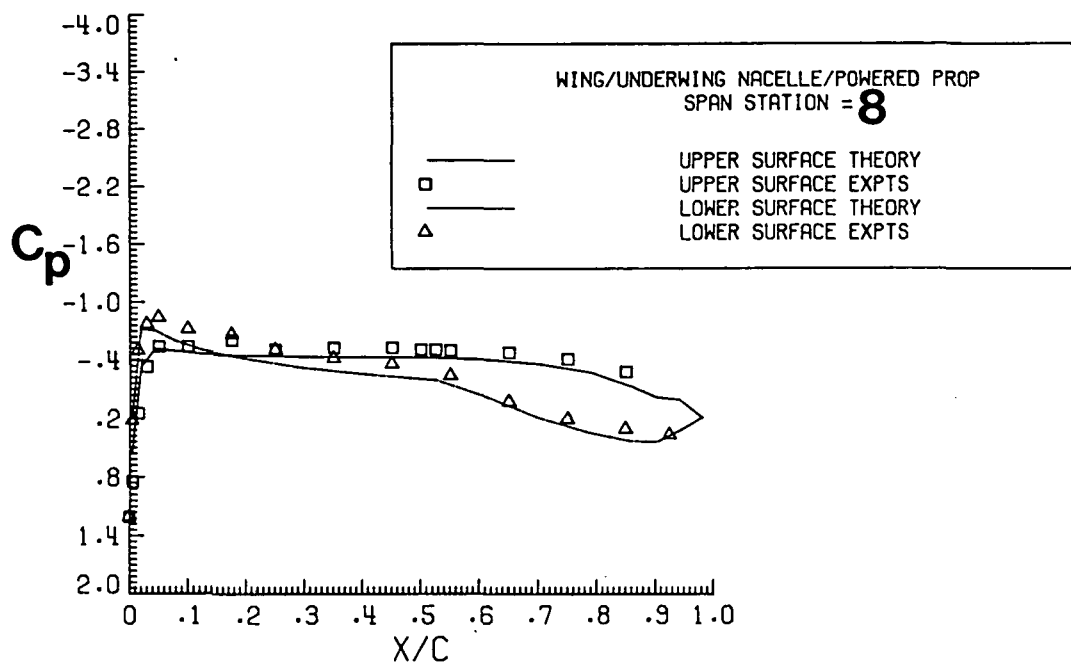


Figure 30. Continued.

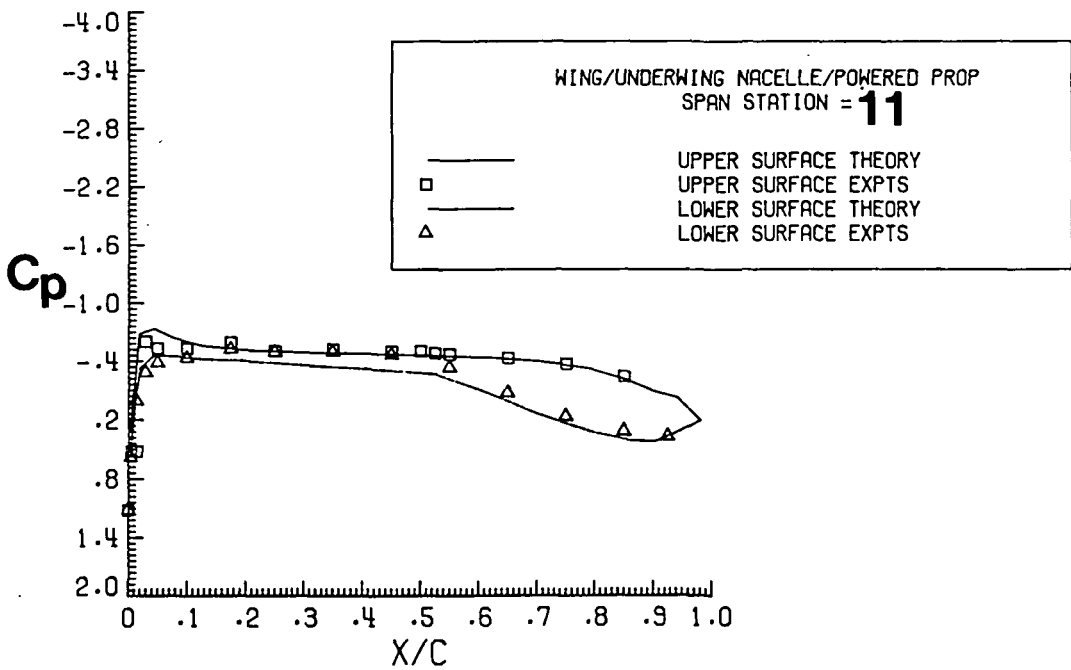
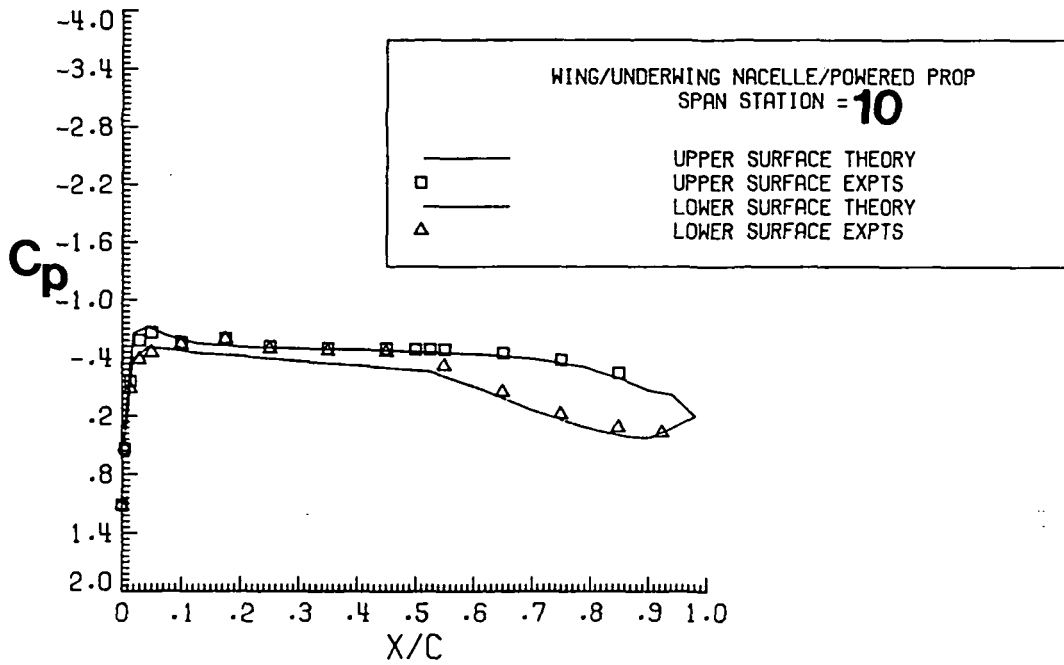


Figure 30. Concluded.

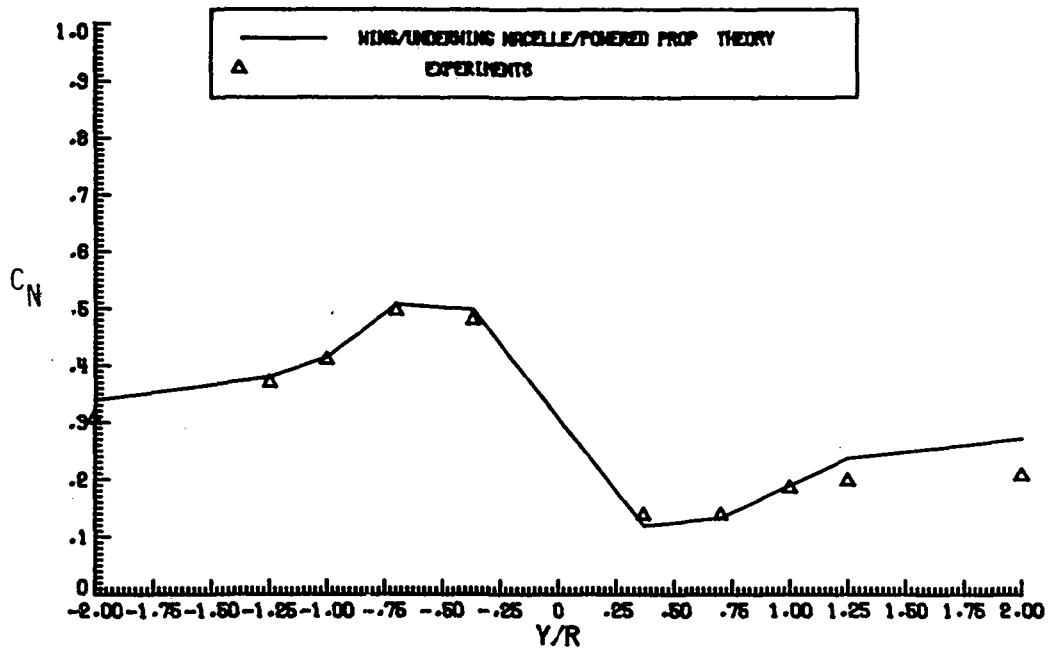


Figure 31. C_N Comparison for the Wing/Underwing Nacelle/Powered Propeller with $C_T = 0.466$, $M_\infty = 0.701$, $\alpha = 0.0$ degree, Method II, without boundary layer.

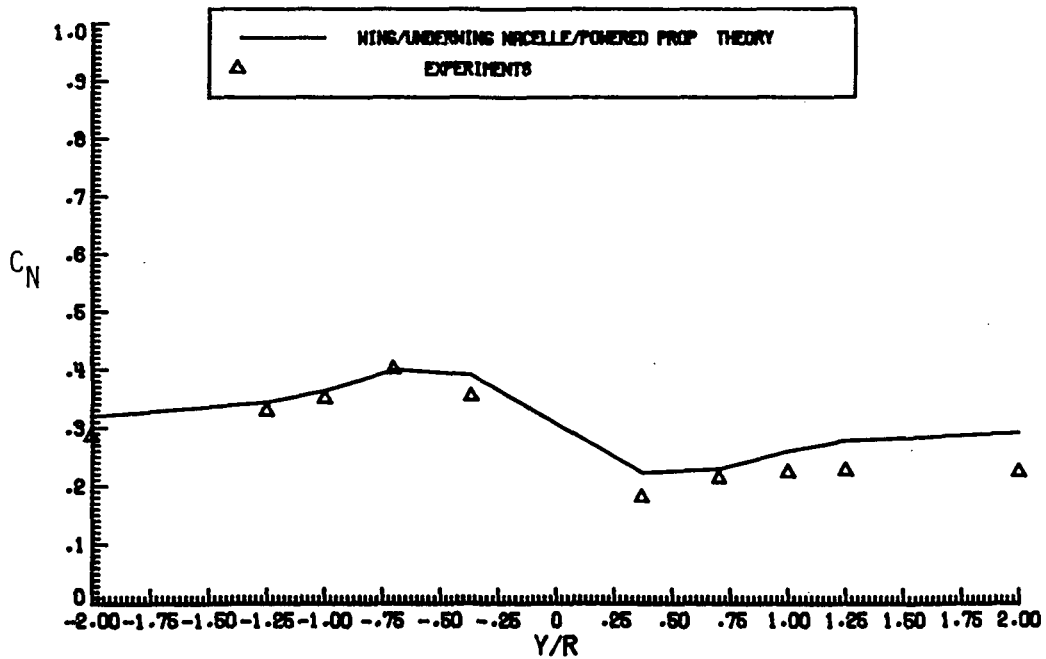


Figure 32. C_N Comparison for the Wing/Underwing Nacelle/Powered Propeller with $C_T = 0.245$, $M_\infty = 0.700$, $\alpha = 0.0$ degree, Method II, without boundary layer.

1. Report No. NASA CR-3887		2. Government Accession No.		3. Recipient's Catalog No.	
4. Title and Subtitle Method for the Prediction of the Installation Aerodynamics of a Propfan at Subsonic Speeds				5. Report Date April 1985	
				6. Performing Organization Code	
7. Author(s) B. Chandrasekaran				8. Performing Organization Report No.	
9. Performing Organization Name and Address Vigyan Research Associates, Inc. 28 Research Drive Hampton, VA 23666				10. Work Unit No.	
				11. Contract or Grant No. NAS1-16742	
12. Sponsoring Agency Name and Address National Aeronautics and Space Administration Washington, DC 20546				13. Type of Report and Period Covered Contractor Report 8/1/1981-12/31/1984	
				14. Sponsoring Agency Code 505-40-90-01	
15. Supplementary Notes Langley Technical Monitor: Lawrence E. Putnam Final Report					
16. Abstract A subsonic-flow panel code has been modified to handle the effects of a propeller wake. The effects of the propeller were modelled by a system of ring vortices of constant strength. Principles based on the blade element theory, the vortex theory and the momentum theory were used to evaluate the axial velocity increase, the swirl velocity and the pressure increase across the propeller. Theoretical calculations are compared to experimental results at Mach numbers up to 0.70 over a range of angles of attack. The discrepancies between the theory and the experimental results are analysed. Suggestions for improvements to enhance the accuracy of the theoretical prediction are indicated.					
17. Key Words (Suggested by Author(s)) Slipstream Vortex rings Blade performance theory Axial induced velocity Swirl			18. Distribution Statement Unclassified - Unlimited Subject Category 02		
19. Security Classif. (of this report) Unclassified		20. Security Classif. (of this page) Unclassified		21. No. of Pages 124	22. Price A06